TESIS DE LA UNIVERSIDAD DE ZARAGOZA

2011

13

Ainhoa Urtizberea Lorente

Open problems in the magnetic behavior of iron-oxide nanoparticles

Departamento

Física de la Materia Condensada

Director/es

Palacio Parada, Fernando

Millán Escolano, Ángel

ISSN 2254-7606

Prensas de la Universidad Universidad Zaragoza

Universidad Zaragoza
1542

Tesis Doctoral

OPEN PROBLEMS IN THE MAGNETIC BEHAVIOR OF IRON-OXIDE NANOPARTICLES

Autor

Ainhoa Urtizberea Lorente

Director/es

Palacio Parada, Fernando
Millán Escolano, Ángel

UNIVERSIDAD DE ZARAGOZA

Física de la Materia Condensada

2011

Open problems in the magnetic behavior of iron-oxide nanoparticles

Ainhoa Urtizberea Lorente

Director 1: Prof. Fernando Palacio Parada
Física Bajas Temperaturas
ICMA (CSIC - U. Zaragoza)

Director 2: Dr. Ángel Millán Escolano
Física Bajas Temperaturas
ICMA (CSIC - U. Zaragoza)

Departamento responsable del Programa: Física Teórica
Departamento de lectura de la Tesis: Física Materia Condensada
Depósito de la tesis: 7 de abril de 2011

Contents

Prologue

Nanotechnology has gained great relevance in the last decades, due to the great variety of applications in medicine, chemistry, physics and biology, among others. The main industrial applications include: magnetic recording [1], printing [2], sealing [3], damping [4], water purification [5], sensors [6] and communication [7, 8]. Iron oxide nanoparticles are particularly attractive in medicine, in the development of novel techniques for early diagnosis [9], non-invasive therapy [10, 11] and biochemical and physiological studies [12, 13]. In scientific research, the possibility of controlling their size and the particle-particle separation, allows these materials to be used as model systems for the study of magnetic properties. There are many examples, such as the physical phenomena arising from their finite size [14], the influence of dipolar interaction [15], the quantum tunneling [16], the giant magnetoresistance [17], ... just to mention some of them. The work developed in this thesis deals with some of these phenomena.

The first chapter comprises a brief description of iron oxides and the magnetic properties of nanoparticles. In chapter 2, we provide a short introduction to the experimental techniques related with the work developed in this thesis. Then, we present two chapters devoted to antiferromagnetic nanoparticles. In chapter 3, we analyze the influence of chlorine content in the magnetic properties of akaganéite nanoparticles. Previous works report that intrinsic properties, such as the Néel temperature and the effective spin of this antiferromagnetic material, are greatly influenced by the amount of interstitial ions. Based on this idea, we analyze how the magnetic relaxation of the nanoparticles is affected by the amount of chlorine contained in the crystal structure. In chapter 4, we show that akaganéite nanoparticles posses a thermoinduced magnetic moment. Antiferromagnetic nanoparticles have a finite magnetic moment arising from the decompensation of atomic spins. In addition, they may exhibit a thermoinduced magnetic moment, due to their finite size, which has the unusual property of increasing with temperature. One of the main complications in the study of this phenomenon is that the magnetic properties of the bulk material are often unknown. To overcome this problem we have chosen akaganéite nanoparticles as a model system because akaganéite can be produced in bulk and therefore, its bulk magnetic properties can be determined in a rather straightforward manner. The following chapters are devoted to studies on ferrimagnetic maghemite nanoparticles. In chapter 5 we show that the saturation magnetization in this system decreases with the nanoparticle size. This decrease can be expressed in terms of bulk saturation magnetization, particle size and thickness of a magnetically disordered layer. The proposed equation is based on the so called core-shell model, which assumes that nanoparticles consist of a bulk-like ferrimagnetic core and a shell of disordered spins. The experimental determination of shell thickness is, in fact, not so straightforward, because there is a noticeable spreading in saturation magnetization values of samples prepared by different synthetic procedures. Therefore we have studied a representative number of nanocomposites, with an average particle size in the range from 1.5 to 15

nm. We estimate a layer thickness of about 1 nm. Chapter 6 deals with the effect of magnetic interactions in magnetic nanoparticles. First, we show that the magnetic relaxation becomes faster as the strength of the interaction increases, in a ferrofluid where dipolar interactions are very weak. There are some reports showing that the relaxation time increases with the degree of interaction while other works show the opposite trend. These discrepancies can be understood following the conclusions deduced from some theoretical models. These models predict that when the interactions are weak in relation to the anisotropy, the magnetic relaxation is no longer governed by the interaction and, actually, becomes faster with growing interactions. In this section, we show that the relaxation time obtained from magnetization measurements decreases with concentration when the interaction strength is weak. Second, we propose an experimental procedure to study the influence of dipolar interactions that enables us to switch on the interactions by magnetically texturing a ferrofluid. This approach allow us to compare the energy barrier of a ferrofluid without dipolar interactions (before the process of texture) with the energy barrier in the presence of dipolar interactions (after the texture process). In addition, we show that the dynamics in a system with dipolar interactions can not be described by the expressions developed for spin-glass transitions. Finally, the last chapter summarizes the main findings of this thesis.

Zaragoza, 6 de abril de 2011

Chapter 1

Introduction

1.1 Iron oxides

The iron oxides are common compounds which are widespread in nature and readily synthesized in the laboratory. There are 16 known iron oxides. These compounds are either oxides, hydroxides or oxide-hydroxides, collectively referred as iron oxides. They consist of arrays of Fe ions (Fe^{II} and/or Fe^{III}) and O^{2-} or OH^{-} ions. The arrangement of the sheets of anions in the third dimension are usually hexagonal close packing (hcp; sheets stacked ABABA...) or cubic close packing (ccp; ABCABC..). Only akaganéite, with a body centered cubic (bcc) anion arrangement, lies outside the scheme. The sheets of anions are staked along some particular crystallographic direction. There are twice as many interstices between the sheets of anions as there are anions in the layer. The cations fit into the octahedral or the tetrahedral interstices. In particular, the Fe^{2+} is octahedrally coordinated while the Fe^{3+} has no preference between the octahedral or tetrahedral coordination. The interstices sites are twice the number of anions and, as the charge of the iron ions (Fe^{2+} and/or Fe^{3+}) is less than the double of the oxygen ions charge, only a portion of the interstices sites are occupied. Differences between the structures arise as a result of variations in the arrangement of cations in the interstices and, to a lesser extent, differences in the stacking of the sheets of anions.

The type of magnetic interaction between Fe ions on adjacent sites depends on the state oxidation of Fe and the Fe-O-Fe angle. This interaction proceeds via the intervening O^{2-} or OH^{-} ligands and is termed superexchange. The intensity of the interaction depends on the Fe-O-Fe bond angle and the Fe-O bond length. The types of exchange interactions in iron oxides are listed in Table. 1.1.

We will subsequently describe the basic properties of the iron oxides related with the work presented in this thesis. For detailed information the reader is referred to Ref. [18].

1.1.1 Akaganéite

Akaganéite, named after the Akagané mine in Japan, is the naturally occurring form of β-FeOOH and it is mainly found in Cl-rich environments such as rust in marine environments. It has a brown to yellow color.

Table 1.1: Exchange interactions in iron oxides according to Ref. [18].

Ion pair	Fe-O-Fe bond angle	Type of interaction
Fe^{3+}-Fe^{3+}	90^o	weak antiferromagnetic
	120^o	strong antiferromagnetic
Fe^{2+}-Fe^{2+}	90^o	weak antiferromagnetic
	120 - 180 ^{o}	strong antiferromagnetic

The structure is based on body centered cubic packing of anions (bcp) and contains either chloride or fluoride ions in the crystal structure. The structure of akaganéite is similar to that of hollandite, characterized by the presence of channels parallel to the b-axis. These channels are partially occupied by chloride anions that give to the crystal its structural stability. Preliminary studies proposed that akaganéite possess a tetragonal symmetry I4/m. However the structural refinement obtained by using the Rietveld analysis of X-ray [19] and neutron diffraction data [20] showed that the unit cell is monoclinic (symmetry I2/m). The structure of akaganéite, shown in Fig. 1.1, consists of double chains of edge-sharing Fe^{3+}-(O,OH) octahedra. These double chains share corners with adjacent chains to give a three dimensional structure containing channels with square cross sections that measure two octahedra per side. The Cl^- ions reside inside the channels. Post et al [20] performed X-

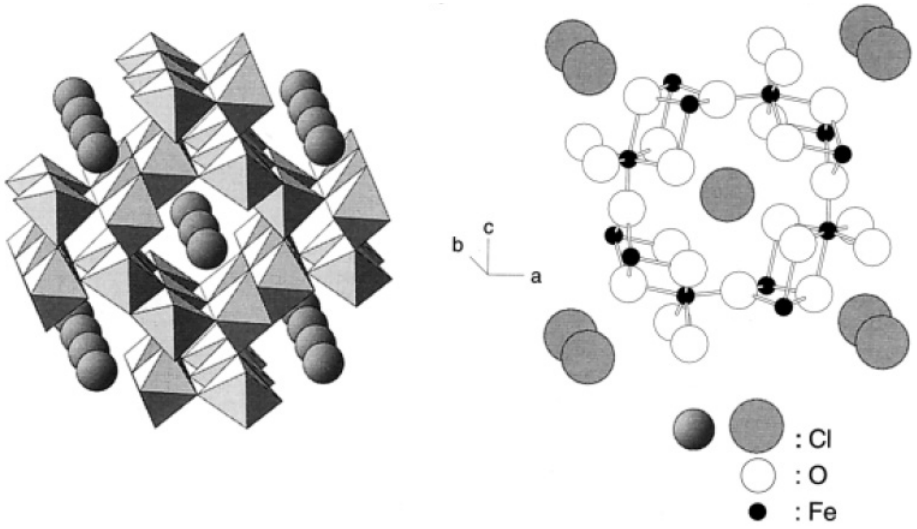

Figure 1.1: Left; Arrangement of octahedral double chains running parallel to the b axis with Cl atoms in the channels. Right; akaganéite unit cell. Images from Ref. [18].

ray powder diffraction (XRD) at different temperatures. They determined that there is no thermal expansion up to ~ 225 °C. For higher temperatures, the unit cell volume gradually decreases. At ~ 290-310 °C akaganéite transforms into hematite. In this transformation,

four molecules of H_2O are released per unit cell.

The exchange interactions between Fe^{3+} ions in akaganéite makes it an antiferromagnetic material. The first structural model for the magnetic structure of β-FeOOH, shown in Fig. 1.2, was proposed from neutron diffraction studies [21]. The magnetic unit cell coincides

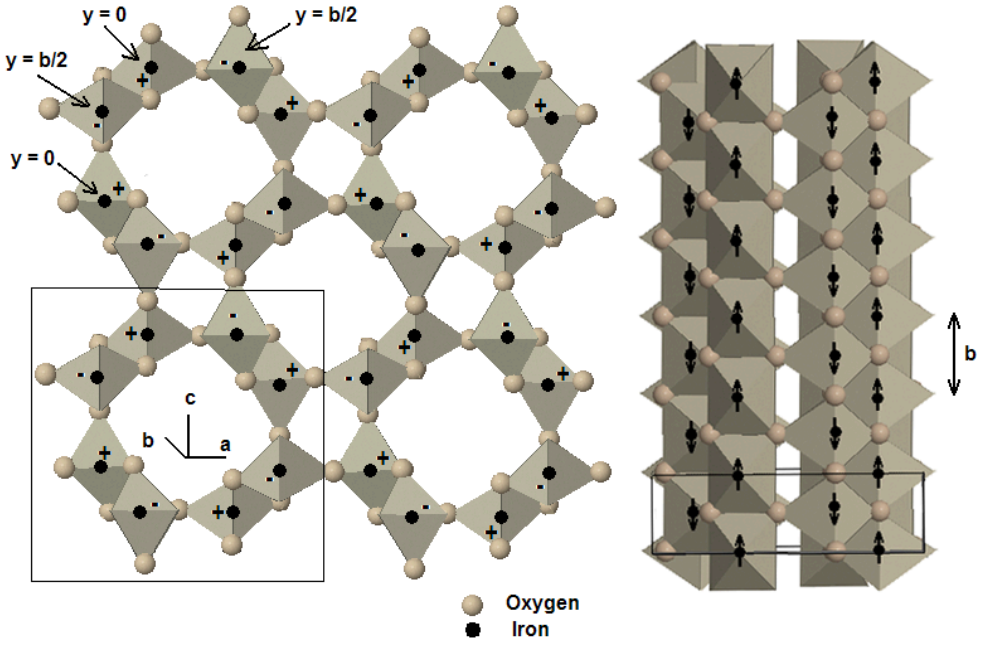

Figure 1.2: Magnetic structure for akaganéite. In the left figure the b axis is pointing towards the reader. Interaction between the iron in different layers is antiferro. Interaction for neighbors running through the b-axis is ferromagnetic.

with the chemical unit cell. The alignment of the magnetic moments along the b-axis was confirmed by Mössbauer experiments [22]. In the magnetic structure proposed in Ref. [21] two layers are defined in a *d010* slice: layer A comprising the Fe ions at y=0 positions and layer B comprising Fe ions at y=b/2 positions. The superexchange interaction between spins belonging to nearest neighbor layers (A-B) propagates through an angle of $\simeq 120^o$. The interaction between the spins of the iron atoms along b-axis (A-A') is held through an angle of $\simeq 104^o$. Thus the spin couples antiferromagnetically with six neighbor spins and weakly antiferromagnetically with two neighbor spins. The interaction between the spins of A-A' iron atoms along b-axis propagates through an angle much smaller than the one between the spins of A-B iron atoms and the interaction between A-A' iron atoms is expected then to be weaker than that between A-B iron atoms. Previous works on akaganéite have concluded that its physical and chemical properties are strongly dependent on the ions that fill the channels. In particular, the Néel T_N and the Curie-Weiss θ temperatures measured for differently synthesized materials are found to vary within rather broad ranges, $T_N \sim 240$ K - 299 K and $\theta \sim 300$ K - 1000 K. Many previous works on akaganéite have analyzed their experimental results within the assumption that two differently coordinated sites are available for the Fe^{3+} ions: those lying close to chlorine ions and those located near the Cl^- vacancies [23]. D. Chambaere and E. De Grave showed that the Néel temperature

strongly depends on the mean number of intersticial water molecules [24]. They associated this dependence to a reduction of the effective 3d-spin S. They came to the same conclusion: there are different sites for the Fe^{3+} ions, those near to a vacant site and those close to the ion occupying the channels. Summarizing, the magnetic structure is as shown in Fig. 1.2, but the strengths of the exchange interactions are highly variable and depend upon the chemical conditions held during the synthesis.

1.1.2 Magnetite

Magnetite, Fe_3O_4 is a black ferrimagnetic material. It is responsible, together with titanomagnetite for the magnetism of the rocks. It is formed in various organisms in which it serves as an orientation aid.

The structure is that of an inverse spinel structure. Magnetite has a face-centered cubic unit cell with $a \sim 8.39$ Å. It contains both Fe^{II} and Fe^{III} ions. The tetrahedral sites (A) are occupied by Fe^{III} ion and the octahedral sites (B) are distributed between Fe^{II} and Fe^{III} ions. Its formula is written as $Fe^{III}[Fe^{II}Fe^{III}]O_4$ where the brackets indicate the octahedral sites. Magnetite is usually non-stoichiometric in which case it has a cation deficient Fe^{III} sublattice. In stoichiometric magnetite $Fe^{II}/Fe^{III} = 0.5$.

Magnetite has a Curie temperature T_c of around 850 K. Below T_c, the spins on the A and B sites are antiparallel. The ferrimagnetism arises since the magnitude of the spins in A sites are different from that of the B sites. At 120 K the magnetite presents the Verwey transition T_v, usually associated to a charge ordering of the Fe^{2+} and Fe^{3+} ions in the octahedral sites. Above T_v the electrons of the Fe are thermally delocalized, which confers high conductivity to magnetite. The magnetite presents cubic anisotropy. The preferred direction of magnetization is along the 8 [111] cube diagonals. Its saturation magnetization is 92-100 emu/g.

1.1.3 Maghemite

Maghemite γ-Fe_2O_3 is a red-brown mineral that occurs as a weathering product of magnetite or as the product of heating other Fe oxides. It has a cubic cell with $a \sim 8.34$ Å. Maghemite is isostructural with magnetite. However, it has no Fe^{2+}, i.e. all the iron is in the trivalent state, such that the charge deficiency produced by the variation of the iron oxidation state is compensated by cation vacancies. Each cell contains 32 O^{2-} ions, 21 1/3 Fe^{III} ions and 2 2/3 vacancies. Eight cations occupy all the tetrahedral sites and the remaining cations are randomly distributed over the octahedral sites. All the vacancies are located in octahedral sites. These considerations give to maghemite the general formula of $Fe_8\,[Fe_{13.3}\square_{2.67}]\,O_{32}$.

Maghemite is ferrimagnetic at room temperature. The determination of T_c is difficult because it transforms to hematite in this range of temperatures. It is estimated to be about 820 to 986 K. The magnetic structure consists of two sublattices corresponding to the Fe^{3+} located on tetrahedral sites and on the octahedral sites, respectively. Below T_c the spins within each sublattice are parallel, but those of the two sublattices are antiparallel. Ferrimagnetism arises from decompensation between the number of Fe ions present in each sublattice. The magnetite presents cubic anisotropy. Its saturation magnetization is 60-80 emu/g.

1.1.4 Iron oxide nanoparticles

Nanotechnology has gained great relevance in the last two decades due to the great variety of real and feasible applications in multidisciplinary fields such as chemistry, physics, medicine, engineering, biology and pharmacy among others. Combining the magnetic properties of the iron oxides with the particular properties of nano-sized materials, the iron oxide nanoparticles have become a fascinating system which have been of interest to the scientific community for a long time.

There are many synthetic routes to produce iron oxide nanoparticles. Some of them are based on the use of polymers. The resulting iron oxide/polymer composites can readily be dispersed to form a ferrofluid, i.e. magnetic stable suspensions of ultrafine ferro- or ferrimagnetic particles. These systems can be used for instance in medicine for cancer therapy and magnetic resonance imaging. Among the numerous routes to prepare the iron-oxide polymer nanocomposites [25], the materials studied in this thesis have been synthesized by in situ precipitation. This procedure profits from the moulding effect of the polymer. In this route, the matrix is mixed with a molecular metal precursor and the particles are grown inside the precursor-polymer compound by addition of a precipitating agent [26–29]. The polymer used here is poly(4-vinylpyridine) (PVP), that has nitrogen base groups that form coordination bonds with iron ions. In this way, the hydrolysis reaction is carried out in a controlled manner. This method is employed for the production of maghemite [30] and akaganéite [31] nanocomposites. In the former case, the precipitating agent was sodium hydroxide and the precursor salt was iron bromide. In the latter, the precipitating agent is the same, while the precursor is iron chloride.

Ferrofluids of magnetic nanoparticles can also be produced in organic solvents by decomposition of iron coordination compounds. The stabilization of these particles is achieved through a surfactant which hinders the particles from flocculation and sedimentation. This synthetic route has the advantage of producing nanoparticles with a very narrow size distribution. This fact makes them ideal materials in fundamental magnetism research. The iron oxide nanoparticles produced is this way can also be used for biomedical applications after coating them with a biocompatible shell. The ferrofluids studied in this thesis have been prepared following the Hyeon method [32], that is based on the thermal decomposition of iron pentacarbonyl in the presence of oleic acid. This method allows the control of particle size with the iron/surfactant ratio.

1.2 Magnetic nanoparticles: basic principles

Bulk ferromagnetic materials develop a domain structure below the ordering temperature. This domain configuration arises from an equilibrium situation in which the creation of domains diminishes magnetostatic energy (demagnetization energy) but increases exchange and anisotropy energies. In the following, we consider only the completely ordered magnetic state, that is, at temperatures far below the ordering temperature. The magnetostatic energy is a function of particle volume and the exchange and anisotropy energies depend on the surface of the domain walls separating different magnetic domains. Then, when the volume is reduced below a critical size, the energy needed to create a domain wall (an action that increases anisotropy and exchange energies) does not compensate the reduction in magnetostatic energy. In this situation, the monodomain configuration becomes the most stable one [33]. Particles of such size and smaller are called single-domain particles and they are superparamagnetic. Such critical size depends on the balance between anisotropy, exchange and magnetostatic energies and therefore is characteristic of the material.

Let us consider the simplest case of a single-domain particle with uniaxial anisotropy under zero applied field and at $T = 0$. The energy term depending of the anisotropy can then be written as

$$E(\theta) = KV\sin^2\theta \tag{1.1}$$

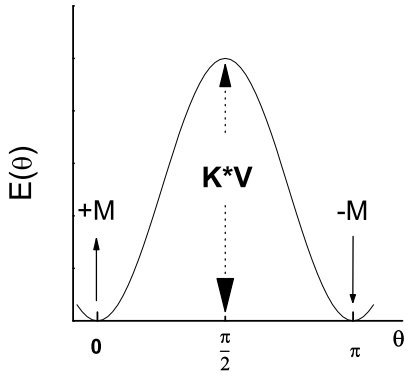

Figure 1.3: Energy of a single-domain particle with uniaxial anisotropy.

where V is the particle volume, θ is the angle between the magnetization and the easy direction of ferromagnetic alignment and K is a constant that depends on the type of anisotropy dominant in the material. The minimum energy orientations correspond to $\theta = 0$ and $\theta = \pi$. They are separated by an energy barrier of height $U = KV$. Therefore, the magnetization will remain stable and lie along the direction defined by $\theta = 0$ or $\theta = \pi$ unless a perturbing energy, like for example thermal agitation, can take the magnetization over the barrier.

If we apply a magnetic field along the easy magnetization axis, the energy expression is then modified to

$$U(H) = KV\sin^2\theta - \mu H\cos\theta \tag{1.2}$$

where θ is the angle between the easy axis and the magnetization vector. Either $\theta = 0$ or $\theta = \pi$ are still directions of minimum energy, but one of them becomes more favorable than the other.

Let us assume that at temperature T=0 the system is in a metastable minimum of energy. Then, the spin will remain in this minimum until the magnetic field suppresses the energy barrier. The location of the maximum energy is at $\cos\theta = -\frac{\mu H}{2KV} \equiv -\frac{H}{H_k}$, where H_k is the anisotropy field. The energy barrier is

$$U(H) = KV\left[1 - \frac{\mu H}{2KV}\right]^2 \tag{1.3}$$

The situation for the field applied along a direction at an angle ψ with the easy axis is shown in Fig.1.5. In this case the minimum position deviates from $\theta = 0$ or $\theta = \pi$ and the height of the energy barrier at low enough fields can be approximated by [34],

$$U(H,\psi) = KV\left[1 - \frac{H}{Hc(\psi)}\right]^{\kappa(\psi)} \tag{1.4}$$

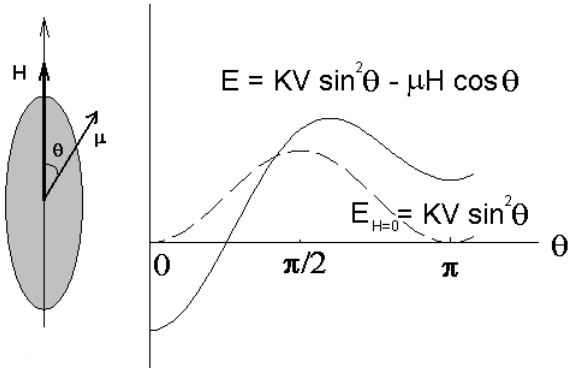

Figure 1.4: Energy of a single-domain particle with uniaxial anisotropy for a field applied along the easy axis.

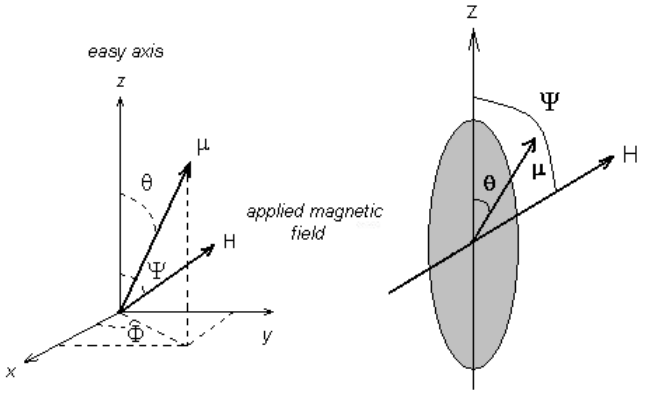

Figure 1.5: Magnetic moment orientation under an applied field for a monodomain particle with uniaxial anisotropy.

where the new critical field that suppresses the energy barrier is $H_c(\psi) = H_k(\text{sen}^{2/3}\psi + \cos^{2/3}\psi)^{-3/2}$

1.2.1 Relaxation time

At finite temperature, overcoming the energy barrier by magnetization is the more likely to occur the smaller the particle volume is. This process can be characterized by a relaxation time τ.

Consider a powder sample of uniaxial particles whose easy axis lie all along the z-axis. If we apply a magnetic field along the positive z-axis direction the powder is magnetized in this direction to saturation M_{sat}. Upon removal of the applied field the magnetization will decay according to $M = M_{\text{sat}}e^{-t/\tau}$. If τ is very large $M \approx M_{\text{sat}}$ for all times and the system remains magnetized to saturation. If τ is small M rapidly vanishes. Now, $1/\tau$ is the

probability (or frequency) of a transition of magnetization between -z and z directions. This probability should be proportional to the Boltzmann factor $e^{-U/k_B T}$

$$1/\tau = \nu = \nu_0 e^{-U/k_B T} \rightarrow \tau = \tau_0 e^{U/k_B T} \tag{1.5}$$

This expression that describes the dependence of the superparamagnetic relaxation time with the temperature, where U is the height of the energy barrier, was first proposed by L. Néel (1949) [35]. It was later modified by W. F. Brown [36] and W. T. Coffey [37] to introduce the dependence of τ_0 with temperature and anisotropy.

1.2.2 Blocking temperature

At finite temperature T it is possible to define a critical energy

$$U_B = k_B T \ln(\tau_{ex}/\tau_0) \tag{1.6}$$

Particles with volume or anisotropy small enough will have an energy barrier smaller than this critical energy so that their magnetic moment can freely rotate like in a paramagnetic material. There are also some particles whose energy barriers are higher than this critical energy $U > U_B$. They cannot surmount the barrier within the experimental time so that their magnetic moment is blocked at an energy minimum.

Similarly a blocking temperature T_B is defined for a single domain-particle as the temperature at which the superparamagnetic relaxation time is comparable with the experimental time. At temperatures lower than the blocking temperature, the magnetic moment can not surmount the energy barrier and becomes blocked.

The height of the energy barrier is proportional to the particle volume. Therefore, in a sample of particles with a distribution of sizes, we also have a distribution of blocking temperatures.

1.2.3 Magnetization of superparamagnetic nanoparticles

Consider a system of N monodomain particles at temperature T such that all the particles have their magnetic moments in thermodynamic equilibrium. The magnetic moment of the particles is free to rotate and each particle behaves as a paramagnetic atom with a very large magnetic moment. The magnetization of N isotropic paramagnetic atoms of magnetic moment J, with an applied magnetic field H is given by [38]

$$M = N g \mu_B J B_J\left(\frac{g\mu_B JH}{k_B T}\right) \tag{1.7}$$

where

$$B_J\left(\frac{g\mu_B JH}{k_B T}\right) = \frac{2J+1}{2J}\coth\left(\frac{2J+1}{2J}\frac{g\mu_B JH}{k_B T}\right) - \frac{1}{2J}\coth\left(\frac{g\mu_B JH}{2Jk_B T}\right) \tag{1.8}$$

is the Brillouin function and $g\mu_B J$ is the maximum magnetic moment of the atom. The magnetization of an ensemble of N noninteracting superparamagnetic particles without magnetic anisotropy can be obtained by means of a simple translation of the paramagnetic theory. Similarly to paramagnetic atoms the magnetization can be written in the form

$$M = N g \mu_B J\left[\frac{2J+1}{2J}\coth\left(\frac{2J+1}{2J}\frac{g\mu_B JH}{k_B T}\right) - \frac{1}{2J}\coth\left(\frac{g\mu_B JH}{2Jk_B T}\right)\right] \tag{1.9}$$

The maximum magnetic moment for the paramagnetic ion is $\mu = g\mu_B J$. Therefore the magnetization of an ensemble of N superparamagnetic nanoparticles of magnetic moment μ

in a magnetic field can be described by

$$M = N\mu\left[\coth\left(\frac{\mu H}{k_B T}\right) - \frac{1}{\frac{\mu H}{k_B T}}\right] \equiv N\mu L\left(\mu\frac{H}{k_B T}\right) \tag{1.10}$$

where μ is the magnetic moment of the particle, k_B is the Boltzmann factor and T is the temperature. $L\left(\mu\frac{H}{k_B T}\right)$ is the Langevin function. In the superparamagnetic regime we can neglect as a first approximation the influence of the anisotropy, size distribution and interparticle interactions. Then the magnetization can be described by Eq. (1.10) so that when magnetization curves are plotted as a function of H/T they superimpose on a single master curve in the whole temperature and field ranges.

At low values of applied field $\mu H << k_B T$,

$$M = N\mu\left[\coth\left(\frac{\mu H}{k_B T}\right) - \frac{1}{\frac{\mu H}{k_B T}}\right] \to N\frac{1}{3}\frac{\mu^2 H}{k_B T} \tag{1.11}$$

that corresponds to the Curie law, typically the linear response limit. At high fields $\mu H/k_B T >> 1$, all the particles have their magnetic moments aligned with the magnetic field and then

$$M = N\mu\left[\coth\left(\frac{\mu H}{k_B T}\right) - \frac{1}{\frac{\mu H}{k_B T}}\right] \to N\mu \tag{1.12}$$

Influence of the particle size distribution

In a more realistic sample we do not have an ensemble of N identical particles of volume V but we usually have a size distribution. We can take into account the size distribution calculating the total magnetization as a superposition of Langevin contributions from each particle size fraction. Let $f(D)$ be the distribution function of particles of diameter D. In the superparamagnetic regime, the total magnetization is then given by:

$$M(H) = \frac{\langle\mu\rangle}{V_{\text{sample}}} = \frac{\int_0^\infty \mu(D,H,T)f(D)dD}{V_{\text{sample}}} \tag{1.13}$$

where the function $f(D)$ is defined as,

$$\int_0^\infty f(D)dD = N \tag{1.14}$$

For particles not very small ($N_{\text{atoms}} > 50$) we can consider that $\mu = M_s V$, where V is the particle volume and M_s is the saturation magnetization of the bulk material. Therefore

$$M(H) = \frac{\int_0^\infty \mu(D,H,T)f(D)dD}{V_{\text{sample}}} = \frac{1}{V_{\text{sample}}}\int_0^\infty V(D)M(D,H,T)f(D)dD = \tag{1.15}$$

$$= \frac{\int_0^\infty V(D)M_s L\left(\mu\frac{H}{k_B T}\right)f(D)dD}{\int_0^\infty V(D)f(D)dD} \tag{1.16}$$

that describes magnetization for a sample with a distribution of particle sizes. The effect of size distribution on the analysis of magnetization curves should not be ignored, otherwise erroneous variations of the fitting parameters with temperature can be obtained [39]. We remark that, as we have a superposition of Langevin functions, the magnetization isotherms measured at different temperatures should still superimpose when represented as a function of H/T.

Influence of the magnetic anisotropy

As a first approximation magnetization of an ensemble of magnetic nanoparticles can be described by a Langevin function of equation (1.10). By taking the size distribution into account and calculating the total magnetization as a superposition of Langevin contributions, a better agreement between calculated and experimental data may be obtained. However discrepancies are still observed at the intermediate field region and at low temperatures. These discrepancies can be sometimes explained by the influence of the magnetic anisotropy [40–42]. In these systems the differences between Langevin model and experimental data appear in an intermediate field region: far from the linear and saturation limits. In the limits of high and low fields the magnetization approaches the Langevin function. Actually, the magnetic anisotropy makes certain directions more favorable for the magnetization alignment such that magnetization curves plotted versus H/T deviate from the ideal behavior as it is shown in Fig. 1.6 for uniaxial anisotropy.

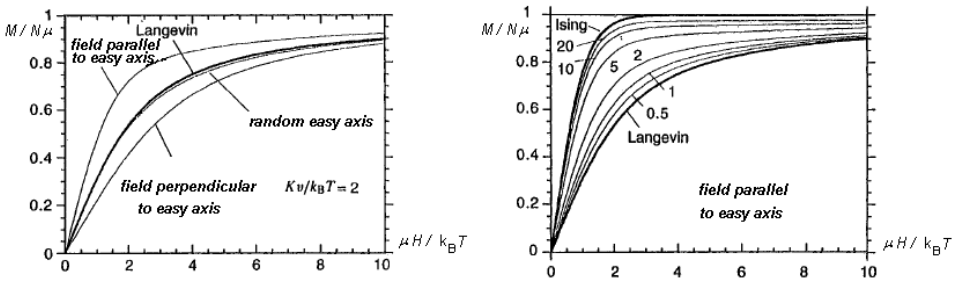

Figure 1.6: Figures taken from Ref. [43]. Anisotropy influence in magnetization curves versus $\mu H/\mathrm{k_B}T$ for an applied field parallel and perpendicular to the easy axis; anisotropy influence in magnetization curves versus $\mu H/\mathrm{k_B}T$ with parallel applied field for different values of anisotropy parameter $KV/\mathrm{k_B}T$.

We will now derive an expression for the magnetization that includes the contribution from the magnetic anisotropy. The energy of a monodomain particle with magnetic moment μ in an external magnetic field is given by the Zeeman term

$$E = -\vec{\mu} \cdot \vec{H}$$

that including the anisotropy contribution leads to

$$E = KV\sin^2\theta - \mu H\cos\alpha \tag{1.17}$$

In thermal equilibrium conditions and for a given orientation of the easy axis, the probability of finding the magnetic moment along a given direction is proportional to the Boltzmann factor,

$$\nu = \exp\{-E/\mathrm{k_B}T\} = \exp\{-(KV\sin^2\theta - \mu H\cos\alpha)/\mathrm{k_B}T\} \tag{1.18}$$

The expected value for the projection of the magnetic moment along the direction of the applied magnetic field is given by the Boltzmann statistics,

$$\frac{\langle M_\mathrm{h}(\vec{e})\rangle_T}{M_0} = \frac{\int_0^{2\pi} d\phi \int_0^{\pi} cos\alpha e^{-E(\alpha,\theta,\phi)/\mathrm{k_B}T} sin\theta d\theta}{\int_0^{2\pi} d\phi \int_0^{\pi} e^{-E(\alpha,\theta,\phi)/\mathrm{k_B}T} sin\theta d\theta} \tag{1.19}$$

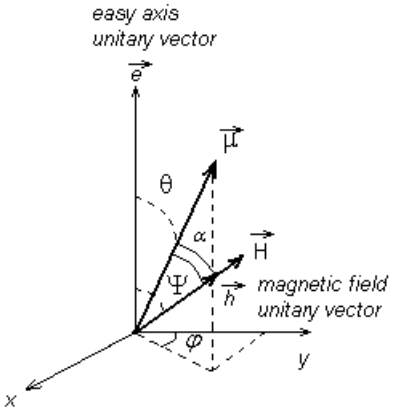

Figure 1.7: Magnetic moment of the particle with an applied field.

No analytical solution is possible for the magnetization $M(H,T,\mu)$ and the expression is usually solved through numerical integration [40, 42]. Analytical solutions for small and very large values of anisotropy are derived by García-Palacios [43].

Neglecting the effect of anisotropy on the analysis of magnetization curves can lead to erroneous fitting parameters also [41]. However, in a sample with randomly oriented easy axis, the initial susceptibility does not depend of the anisotropy [44]. Then we can avoid problems associated with the analysis of the full magnetization curve using the initial susceptibility for example to determine the possible temperature dependence of μ.

1.2.4 AC susceptibility

Different experimental techniques can be used to study superparamagnetic relaxation. They include dc susceptibility (with τ_{ex} around 100 s), ac susceptibility (τ_{ex} in a variable range from 0.1 s to 10^{-5} s), Mössbauer spectroscopy (time window from 10^{-7} s to 10^{-9} s), magnetic resonance ($\tau_{ex} = 10^{-9}$ s) and neutron diffraction (time window from 10^{-8} s to 10^{-12} s depending on the experiment). The choice of the experimental technique depends on the experimental time we are interested in. In this section we will briefly describe susceptibility measurements.

The equilibrium susceptibility describing the linear response to an applied field h, is related to the fluctuations of the magnetic moment by

$$\chi = M_S^2 V \frac{\left\langle (\vec{e}\cdot\vec{h})^2 \right\rangle_0 - \left\langle (\vec{e}\cdot\vec{h}) \right\rangle_0^2}{k_B T} \tag{1.20}$$

where the 0 subscript means average at zero field and $\vec{e}$ and $\vec{h}$ are unit vectors along the magnetic moment and applied field. The term $< (\vec{e}\cdot\vec{h}) >_0 = 0$ and developing $< (\vec{e}\cdot\vec{h})^2 >_0$ for large values of $\sigma = KV/k_B T$ one can write for the susceptibility [45],

$$\chi = \text{sen}^2\psi\chi_\perp + \cos^2\psi\chi_\parallel \tag{1.21}$$

where the field is applied with an angle ψ with respect to the easy axis and

$$\chi_\parallel = \frac{M_S^2 V}{k_B T}\frac{R'}{R} \qquad \chi_\perp = \frac{M_S^2 V}{k_B T}\frac{R - R'}{2R} \tag{1.22}$$

are the equilibrium susceptibilities parallel and perpendicular to the easy directions, respectively. The function $R(\sigma) = \int_0^1 \exp(\sigma x^2)dx$ introduces the influence of anisotropy and R' is its derivative. Formula (1.21) is averaged over a distribution of the particle easy axis orientations,

$$\chi = \left\langle \text{sen}^2\psi \right\rangle \chi_\perp + \left\langle \cos^2\psi \right\rangle \chi_\parallel \tag{1.23}$$

Let us consider now the application of a magnetic field $\vec{h} = \vec{h}_0 \text{sen}\omega t$ that oscillates with time. The ac susceptibility has two components: the *in phase* susceptibility and the *out of phase* susceptibility, dephased $\pi/2$ with respect to the applied field. The *in phase* component χ' is the linear response of the magnetization to the applied field.

For the linear response, we can separately consider the contributions to the magnetic moment induced by the field components along the easy axis and perpendicular to it. The response of the longitudinal and transverse components have very different characteristic times $\tau_\parallel$ and $\tau_\perp$, respectively. M.I. Shliomis and V.I. Stepanov [46] proposed a generalization of Eq. (1.23) that consists of attaching Debye-like factors to each component,

$$\chi = < \text{sen}^2\psi > \frac{\chi_\perp}{1 + i\omega\tau_\perp} + < \cos^2\psi > \frac{\chi_\parallel}{1 + i\omega\tau_\parallel} \tag{1.24}$$

The transverse field component just shifts the energy minima from their initial positions at $\theta = 0$ and $\theta = \pi$ towards $\pi/2$. The magnetic response involves then only transitions between orientations located on each potential energy well. It can be considered instantaneous with $\tau_\perp \sim \tau_0$. By contrast the response to the parallel component requires overcoming the anisotropy energy barrier which leads to a $\tau_\parallel$ increasing exponentially as T decreases. So that averaging over easy axis orientations $\langle \text{sen}^2\psi \rangle = 2/3$ and $\langle \cos^2\psi \rangle = 1/3$ we get for the ac susceptibility,

$$\chi = \frac{1}{3}[2\chi_\perp + \frac{\chi_\parallel}{1 + i\omega\tau_\parallel}] \tag{1.25}$$

When $\tau << \tau_{\text{ex}}$ the susceptibility takes the equilibrium value we calculated for the isotropic case (Eq. (1.11)) $\chi_{\text{eq}} = \frac{M_S^2 V}{3k_B T}$. When $\tau >> 1/\tau_{\text{ex}}$ we have $\chi_\perp = M_s^2/2K$ and $\chi_\parallel = \chi_0 - M_s^2/K$.

In a polydisperse sample the susceptibility is obtained averaging the 'monodisperse' susceptibility over the distribution of particle sizes. The susceptibility can then be written as [47, 48]

$$\chi' \simeq \int_0^{U_B} \chi_{eq}(U,T) f(U) dU + \frac{2}{3} \int_{U_B}^{\infty} \chi_\perp(U,T) f(U) dU \tag{1.26}$$

$$\chi'' \simeq \frac{\pi}{2} k_B T \chi_{\text{eq}}(T, U_B) f(U_B) \tag{1.27}$$

where χ_{eq} and $\chi_\perp$ are as defined previously and U_B is defined in Eq. (1.6).

The magnetic anisotropy gives rise to an energy barrier, as we described in Sec. 1.2.2. Below a temperature T_B the magnetic moments are blocked and at higher temperatures the magnetic moments can freely rotate. This blocking temperature depends with the frequency. And when we plot the out of phase component of the ac susceptibility $\chi''(T,\omega)$ as a function of temperature we obtain different blocking temperatures for different frequencies. Therefore at temperatures such that all the particles have their magnetic moment deblocked $\chi''(T,\omega)$ vanishes and $\chi'(T,\omega)$ curves measured at different frequencies superimpose.

The equilibrium information about the average magnetic moment of the sample is the only component of the in phase susceptibility $\chi'(T,\omega)$ and

$$\chi_{\text{eq}} = \frac{\int f(D)\mu^2(D)/3k_B T dD}{\int f(D) V dD} \tag{1.28}$$

The equilibrium susceptibility can be determined from the dc magnetic measurements at low fields as we explained in Sec. 1.2.3 and from ac magnetic measurements.

1.2.5 Dipolar interactions

Often, the magnetic nanoparticles are close enough such that dipolar interactions become relevant. If the concentration of particles is high, the dipole-dipole interactions affect the superparamagnetic relaxation, susceptibility and magnetization curves. The interpretation of the results from the experiments is somewhat complicated. However, different models have been proposed that describe the effect of interactions on superparamagnetic relaxation and equilibrium properties.

Effect of interactions on the magnetic relaxation

Two controversial models that predict opposite effects are usually followed to describe the effect of interactions on the magnetic relaxation. The Dormann-Bessais-Fiorani model [15] and the Mørup-Hansen-Tronc model [49]. In the Dormann-Bessais-Fiorani model (DBF) the relaxation time is written according to a Néel law with a modified effective energy barrier. This effective energy barrier includes the anisotropy barrier of the single-particle plus the dipolar interaction energy between the magnetic moment of the particle with that of the neighboring particles. The effect of interaction is the polarization with the neighbor magnetic moments. They propose an expression for the energy barrier due to the interactions [50]

$$E_{\mathrm{Bint}} \sim \sum_j n_{\mathrm{j}} E_{\mathrm{Bj}} L\left(E_{\mathrm{Bj}}/\mathrm{k_B}T\right) \tag{1.29}$$

where n_{j} is the number of jth neighbors and $E_{\mathrm{Bj}} \simeq \mu^2/d^3$ where d is the average distance between particles. Two regimes of medium and weak interactions are distinguished according to the value of a mean field magnetization factor $[a_1 M_{\mathrm{S}}^2 V/\mathrm{k_B}T]$, where $a_1 \sim c_{\mathrm{v}}/\sqrt{2}$ accounts for the relative orientation of magnetic moments in the particles arrangement. In both regimes the interaction effect is strong enough to increase the energy barrier as compared to that for the non-interacting particle. Therefore an increase of the relaxation time with increasing interactions strength is predicted.

In the Mørup-Hansen-Tronc model (MHT) the interaction strength is assumed to be weak enough to neglect any polarization between magnetic moments and the particle magnetic moment is just exposed to a dipolar field, which has contributions from the neighboring particles. The total magnetic energy is calculated adding to the energy barrier of the single-particle energy barrier E_{b0} the energy arising from the interaction of the particle magnetic moment with this dipolar field. In this model the variation of the relaxation time with the blocking temperature is also described by a Néel law with a modified energy barrier as

$$\tau = \tau_0 \exp\left[\alpha - \frac{\beta_{\mathrm{av}}^2}{3}\left(1 - \frac{3}{4}\alpha^{-1}\right)\right] \tag{1.30}$$

where $\alpha = E_{\mathrm{b0}}/\mathrm{k_B}T$ and $\beta_{\mathrm{av}}^2 = 2[(\mu_0/4\pi)^2\mu^2\mu^2\Sigma d_{nn}^{-6}]/(\mathrm{k_B}T)^2$ in which V is the mean particle volume, μ is the average magnetic moment and d_{nn} is the distance between the particle and its nearest neighbors. We make use of the definition of Mørup for $\Sigma d_{nn}^{-6} = \epsilon^{-6} D^{-6} \Sigma a_{nn}^{-6}$, where Σa_{nn}^{-6} depends on the geometrical arrangement of particles that is taken of the order of ~ 10-20 and ϵD is the average particle-particle distance $\epsilon^3 D^3 = V/c_{\mathrm{v}}$. The mean magnetic moment $\mu = M_{\mathrm{S}} V$, where $M_{\mathrm{S}} = M_{\mathrm{S}}(T=0)(1 - bT^{\alpha})$ can be calculated from dc magnetization measurements. The energy barrier obtained for $\alpha > 1$ decreases with increasing strength of interactions. Let us notice that in this model the dependence of τ_0 with temperature is not taken into account [36] as noticed by J. L. Dormann [51] and then values obtained for τ_0 are usually unreasonably small.

Another theoretical approach is the model proposed by P. E. Jönsson, J. L. Garcia-Palacios, M. F. Hansen and P. Nordblad (JGP) [52]. It describes the influence of dipolar interactions in the magnetic relaxation and also in the initial susceptibility. They analyze the effect of weak dipolar interactions by a local thermodynamic average of the dipolar field. The expression for the relaxation time is

$$\tau = \tau_0 e^{\sigma}[1 + 1/2\xi_{//}^2 + 1/4F(\lambda\sigma^{1/2})\xi_{\perp}^2]^{-1} \tag{1.31}$$

where λ is the damping constant, $< \xi_{//}^2 >= \xi_d^2 \mathrm{R}/3$, $< \xi_{\perp}^2 >= \xi_d^2/3$ 2R and $\mathrm{F}(\alpha) = 1 + 2(2\alpha^2 e)^{1/2\alpha^2}\gamma(1 + 1/2\alpha^2, 1/2\alpha^2)$, where γ is the incomplete gamma function and R is the factor that describes the particles arrangement. The factor $\xi_d = \mu_0\mu^2/4\pi a^3 \mathrm{k_B}T$ is the dipolar field at the temperature T, in which a is the mean particle-particle distance, and μ is the particle magnetic moment. The anisotropy barrier of the single-particle is included through $\sigma = KV/\mathrm{k_B}T_\mathrm{B}$. In a simple cubic lattice structure arrangement of particles R=16.8 [52]. The expression for the attempt time $\tau_0 = \tau_D\sqrt{\pi}\sigma^{3/2}$ where τ_D is the relaxation time of an isotropic spin. Let us notice that in this model the blocking temperature decreases for increasing interaction as it is shown in Fig.1 of Reference [52] for λ= 0.1 (typical value assumed for ultrafine particles).

Another model which involves numerical calculation is developed by D. V. Berkov and N. L. Gorn [53]. In this model the temperature dependence of the ac susceptibility is simulated numerically for various particle concentrations and single-particle anisotropy strengths. They take as a starting point the stochastic Landau-Lifshitz-Gilbert equation for the motion of each magnetic moment. The effective field in the equation includes the external field, the anisotropy field and the particle-particle dipolar interaction. The thermal fluctuations are included through the so-called 'fluctuating field'. In this model they distinguish two anisotropy regimes depending on the value of the factor $\beta = 2K/M_\mathrm{S}$. For values of $\beta \geq 1$ this corresponds to moderate and large anisotropy regime in which they show that the peak of the out-of-phase susceptibility component shifts towards lower temperatures with increasing particle concentration. Besides, in these systems another interesting feature is observed: the out of phase susceptibility component χ'' displays a non-monotonic dependence of the peak height on the particle concentration. The dependence of the peak height of χ'' with the frequency is also very unusual as shown for $\beta = 2$ [53]. With increasing frequencies the peak position is shifted to higher temperatures and the peak height decreases. The main conclusion of this model is that dipolar interactions can either decrease the energy barriers, when single-particle anisotropy is very large and dominant or increase the energy barriers when dipolar interactions dominate over the anisotropy.

The influence of dipolar interactions on the magnetic relaxation is also studied by Monte Carlo simulations by O. Iglesias and A. Labarta [54]. In particular, they determine the energy barrier distributions for different dipolar interaction strengths. They found that there exist a weak interaction regime and a strong interaction regime. For weak interactions the distribution becomes wider and the mean effective barrier shifts towards lower values as the interaction increases. When entering the strong interaction regime the distribution becomes distorted and the distribution shifts to larger energy values. This results are in agreement with the numerical simulations of D. V. Berkov and N. L. Gorn [53].

Effect of dipolar interactions on the magnetization curves

In some systems of ferromagnetic nanoparticles, the magnetization curves do not seem to follow a superparamagnetic scaling law $M(H/T)$ at temperatures much higher than those defined for the blocking regime. We already mention in Sec. 1.2.3 that deviations to this

law may arise from non-negligible anisotropy. But deviations produced from anisotropy are noticeable at intermediate fields. Actually, at low fields in a system with randomly oriented easy axis the effect of anisotropy in the initial susceptibility cancel out. There exist some systems in which differences in the initial susceptibility are also observed. The decrease of the initial susceptibility in dc magnetization with the increase of the strength of dipolar interactions have been observed in Montecarlo simulations by H. Kachkachi and M. Azeggagh [44].

An analytical model that describes the influence of magnetic interaction on the susceptibility is that proposed by P. E. Jönsson, J. L. Garcia-Palacios, M. F. Hansen, P. Nordblad (JGP) [52]. They give an expression for the equilibrium susceptibility for an interacting system of nanoparticles with random anisotropy and spherical sample shape

$$\chi_{\mathrm{eq}} = \mu_0 \mu^2 / 3\mathrm{k_B} T (1 - 1/18 \xi_d^2 R) \tag{1.32}$$

in SI units, where the parameters of this expressions have been cited above.

A phenomenological model used in the description of the influence of these interactions on the initial susceptibility and magnetization curves is that proposed by P. Allia et al [55]. They suggested that the fitting of magnetization curves with a superposition of Langevin functions is not appropriate in systems with non negligible magnetic interactions. Besides, they state that the fact that the magnetic moment obtained in the fits increases with temperature, is actually a consequence of the inappropriate use of the Langevin functions. P. Allia et al proposed that the description of the influence of these interactions can be modeled introducing a slight transformation in the argument of the Langevin function,

$$M = N\mu L\left(\frac{\mu H}{\mathrm{k_B}(T + T^*)}\right) \tag{1.33}$$

This T^* is a temperature related to the energy of the dipolar interaction of a nanoparticle with its neighbors,

$$\mathrm{k_B} T^* = \varepsilon_D = \alpha \mu^2 / d^3 \tag{1.34}$$

where d is the average particle-particle distance and α accounts for the geometrical distribution with the neighboring magnetic moments (actually it is the factor Σa_{nn}^{-6} in the MHT model). So that T^* reflects the strength of the interactions.

Equation (1.33) can be written as

$$M = N_a \mu_a L\left(\frac{\mu_a H}{\mathrm{k_B} T}\right)$$

where

$$\mu_a = \frac{\mu}{1 + \frac{T^*}{T}} \quad \text{and} \quad N_a = \left(1 + \frac{T^*}{T}\right) N \tag{1.35}$$

Two temperature regimes can be distinguished. At temperatures $T > T^*$ the $\mu_a \approx \mu$ and M/M_{S} scales with H/T, so that we are at the superparamagnetic regime. At temperatures $T < T^*$ the magnetic moment $\mu_a = \frac{\mu}{T+T^*} T$ increases with temperature and we are in the interacting-superparamagnetic regime.

From low field expansion of Eq. (1.33) the expression for the initial susceptibility is obtained,

$$\chi = \frac{N\mu^2}{3\mathrm{k_B}(T + T^*)} \tag{1.36}$$

For a system with a magnetic moment distribution Eq. (1.33) becomes

$$M = N \int_0^\infty \mu L\left(\frac{\mu H}{\mathrm{k_B}(T + T^*)}\right) f(\mu) d\mu = N_a \int_0^\infty \mu_a L\left(\frac{\mu_a H}{\mathrm{k_B} T}\right) f(\mu_a) d\mu_a \tag{1.37}$$

where relations (1.35) hold. Magnetization isotherms are fitted with this expression (assuming N_a independent of temperature) to determine μ_a. The expression for the equilibrium susceptibility Eq. (1.36) is also modified, so that the reciprocal susceptibility becomes,

$$\frac{\rho}{\chi} = 3k_B N\left(\frac{T}{M_S^2}\right) + 3\alpha \tag{1.38}$$

where $\rho =< \mu^2 > / < \mu >^2 =< \mu_a^2 > / < \mu_a >^2$. The parameter T^* can be determined by fitting Eq. (1.38) to the experimental reciprocal susceptibility. With the parameters μ_a and T^*, the actual magnetic moment μ is calculated. If magnetization curves are not available, we can determine from expression Eq. (1.38) the actual magnetic moment μ from inverse susceptibility fits. But then the value of ρ should be known in advance. For a ferromagnetic material we can assume $\mu \propto V$ so that $\rho =< V^2 > / < V >^2$. Fitting of inverse susceptibility to the expression Eq. (1.38) gives α and then

$$\mu = \left[\left(\frac{\rho}{\chi} - 3\alpha\right)\frac{N}{3k_B T}\right]^{-1/2} \tag{1.39}$$

Then, if size distribution is known, N and ρ can be determined and μ calculated from the latter expression.

This model was reexamined by M. El-Hilo et al [56] showing that conclusions about particle interactions should be drawn carefully. They calculated an analytical expression for the inverse equilibrium susceptibility in the superparamagnetic regime. They reported that χ follows an expression similar to Eq. (1.36) such that T^* has two distinct contributions, from blocking and from the interactions, $T^* = T_B - T_i$. Then, a negative $T^* = T_B$ is obtained even in absence of magnetic interactions. Besides, the $T^* = 0$ does not imply negligible magnetic interactions but just that interaction effects are compensated with that of blocking.

Therefore the model of P. Allia et al [55] can be used to qualitative study the influence of interactions in the initial susceptibility. But one should be careful with the conclusions drawn from it.

1.2.6 Antiferromagnetic particles

In antiferromagnetic materials the magnetic moment of an atom interacts with that of its nearest neighbors in such a way that magnetic interaction tend to align the moments antiparallel. The direction of ordering is defined by the easy axis of magnetization. In the simplest case an antiferromagnet can be regarded as two identical sublattices, say A and B. The magnetic moment of atoms from sublattice A interact antiferromagnetically with the magnetic moment of atoms from sublattice B. And the magnetic moment of atoms from sublattice A can interact ferro or antiferromagnetically with the magnetic moment of sublattice A. At temperatures below the ordering temperature, called the Néel temperature (T_N), the antiferromagnet is in its ordered state. In this situation magnetization of each sublattice are antiparallel to one another. The magnitude of the resultant spontaneous magnetization tends to zero at $T = 0$.

Consider we apply an external magnetic field along the easy direction. At absolute zero temperature the net magnetization is still zero. But, if we apply at $T = 0$ the external magnetic field perpendicular to the direction of the easy axis the magnetic moments of both sublattices will tend to align with the external magnetic field. So that in bulk antiferromagnetic materials there exist a non zero contribution to the magnetization, arising from the sublattices canting by the perpendicular component of the magnetic field, even at $T = 0$. At temperatures below T_N the magnetization of an antiferromagnet is linear with the applied

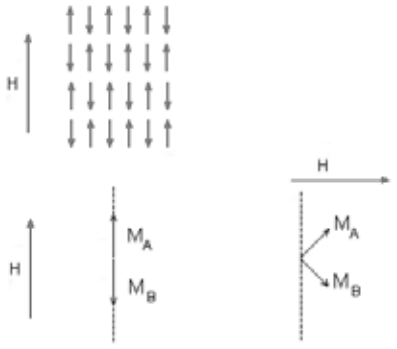

Figure 1.8: Magnetic moments for an antiferromagnet when applied magnetic field is parallel and perpendicular to easy direction.

field, $M{=}\chi_{\mathrm{AF}}H$ where χ_{AF} is the antiferromagnetic susceptibility. For a random distribution of easy magnetization axis, $\chi_{\mathrm{AF}} = 1/3\chi_{//} + 2/3\chi_{\perp}$. The perpendicular component $\chi_{\perp}$ is temperature independent, but $\chi_{//}$ increases with temperature up to T_{N} where it meets the value of $\chi_{\perp}$. Then in a bulk antiferromagnetic material χ_{AF} increases with temperature up to $T = T_{\mathrm{N}}$, decreasing for $T > T_{\mathrm{N}}$ following a Curie-Weiss law.

As the size of the antiferromagnetic material decreases, the particles start to show magnetic phenomena different from that of the bulk. This behavior was first discussed by L. Néel [57–59]. He proposed that an additional contribution from the decompensated magnetic moments exists for antiferromagnetic nanoparticles $\mu_{\mathrm{per\ atom}}(N_{\mathrm{atoms}})^{x}$ where $\mu_{\mathrm{per\ atom}}$ is the magnetic moment of each magnetic atom and N_{atoms} is the number of atoms per particle. The parameter x range from 1/3 to 2/3 depending on how the decompensated magnetic moments are distributed in the crystal. This parameter x is taken as 1/2 for disordered spins and 1/3 when the disorder arises from the surface (in the surface there are $N_{\mathrm{surf}} = N_{\mathrm{atoms}}^{2/3}$ spins). This additional component to the magnetic moment experiences the energy barrier due to the coupling with the antiferromagnetic moments such that a relation similar to that of the equation (1.5) holds: $\tau = \tau_0 e^{U/\mathrm{k_B}T}$. This contribution to the magnetic moment does not increase with temperature [60].

S. Mørup [61, 62] proposed the existence of another contribution to magnetic moment in antiferromagnetic nanoparticles that has the unusual property of increasing with temperature. This contribution will be described in the following section.

Néel [58] modeled the magnetization response of small antiferromagnetic particles under an external applied field. He concluded that it is a complicated combination of both bulk and nanoparticle response. However, at low enough fields if $\mu H/\mathrm{k_B}T \ll 1$ and $(\chi_{\perp}{-}\chi_{//})H^2/2\mathrm{k_B}T \ll 1$ it is just a linear combination of bulk volume susceptibility χ_{AF} and nanoparticle Langevin contribution (see Eq. (1.11)),

$$\chi = \chi_{\mathrm{AF}} + N\frac{1}{3}\frac{<\mu^2>}{\mathrm{k_B}T} \tag{1.40}$$

The dependence of the magnetic moment can therefore be calculated from equilibrium susceptibility for the antiferromagnetic nanoparticle if χ_{AF} is known.

1.2.7 Spin waves in antiferromagnets: thermoinduced magnetic moment

The exchange interaction in a ferromagnet tends to align the spins parallel to one another along the easy axis such that at T=0 the system is completely ordered. At finite temperatures the system can access to higher energy states, so that it can be perturbed from its fully ordered configuration. These states can be described classically considering the spin as a classical vector of magnetic moment oriented at T=0 along the anisotropy direction. In the excited states, the magnetic moment vector deviates its orientation and precesses around the easy axis. The exchange interaction favors this deviation in the spin direction to propagate as a wave.

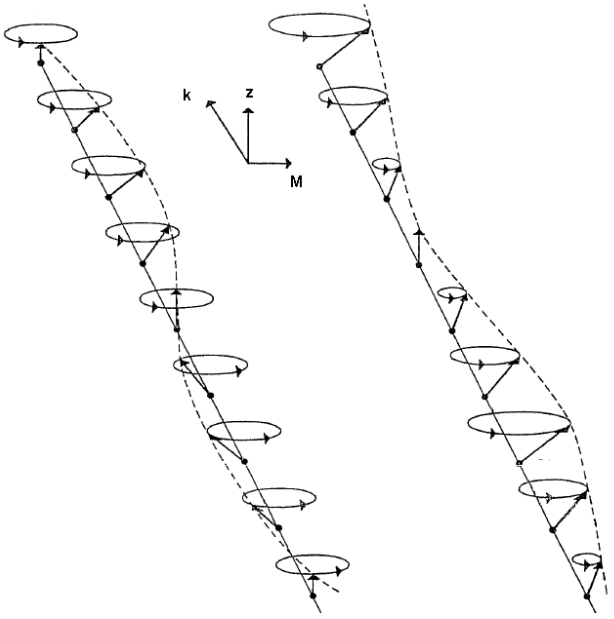

Figure 1.9: Spin wave propagation in the direction $\vec{k}$ in a ferromagnetic material. Figures taken from Ref. [38].

In an antiferromagnet the exchange interaction tends to align the spins in the same direction but with opposite senses. Let us assume that we can neglect the anisotropic contributions so that the energy of the system is completely determined by the exchange interaction. As in a ferromagnet, at T=0 the system is completely ordered, but at finite temperatures each spin precesses around its initial orientation. Since the momenta are oppositely aligned, the resultant precessions would be in opposite senses. The exchange interactions therefore do not sustain this motion and indeed it can be shown that this spin wave is not a normal mode of the system. To form normal modes it is necessary to allow the two sublattices to precess with unequal amplitudes [38, 63]. The precession amplitude depends on the energy of the mode. The excitation energy of spin waves for antiferromagnets

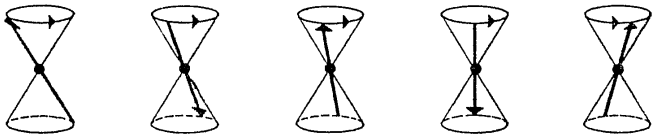

Figure 1.10: Spin wave propagation in an antiferromagnetic material : mode not allowed. Figures taken from Ref. [38].

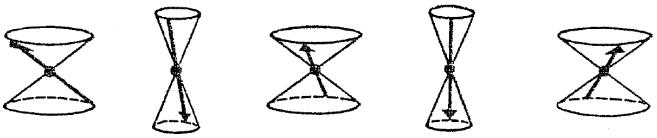

Figure 1.11: Spin wave propagation in an antiferromagnet: allowed normal mode. Figures taken from Ref. [38].

is given by [38]

$$\hbar\omega_k = g\mu_B \left[(H_E + H_{AN})^2 - H_E^2 \{ \frac{1}{z} \sum_m \cos\vec{k} \cdot \vec{a}_m \}^2 \right]^{1/2} \pm g\mu_B H \simeq \tag{1.41}$$

$$= g\mu_B \left[(H_E + H_{AN})^2 - H_E^2 \left(1 - \frac{2k^2a^2}{z} \right) \right]^{1/2} \pm g\mu_B H \tag{1.42}$$

where H_E is the exchange magnetic field, H_{AN} is the anisotropy field and H is the applied field. The summation is over all lattice vectors $\vec{a}_m$ that connect an ion with its z neighbors. In finite nanosized materials wave vectors that can propagate are limited, like in a stationary wave in a closed tube. Therefore only those modes that fulfill the condition $\lambda/2 = L/n \rightarrow |\vec{k}| = 2\pi/\lambda = n\pi/L$ can propagate through the material. Actually, modes with $k = 0$ are also possible and they have a non-zero magnetic moment that increases with increasing temperature.

Thermoinduced magnetic moment

S. Mørup et al calculated semi-classically the temperature dependant susceptibility for an antiferromagnetic system in which just the uniform mode is populated [61, 62]. The calculation is completely developed in Ref. [62] so that we will just give a brief description here. In this calculation any uncompensated magnetic moment other than the ones arising from the thermal population of spin waves, is neglected. The contribution from uncompensated magnetic moment is further taken into account in Ref. [64].

If no magnetic field is applied, the energy of the homogeneous mode with $k = 0$ is

$$\hbar\omega_0 = g\mu_B \left[(2H_E + H_{AN}) H_{AN} \right]^{1/2} \simeq g\mu_B \sqrt{2H_E H_{AN}} \tag{1.43}$$

When this uniform state is excited the magnetization vectors of both sublattices precess around the easy axis with angles θ_A and θ_B such that $\theta_A \neq \theta_B$ and

$$\frac{\sin\theta_A}{\sin\theta_B} \simeq 1 + \delta \quad \text{where} \quad \delta = \pm\sqrt{2\frac{H_{AN}}{H_E}} \tag{1.44}$$

This leads to a non-zero magnetic moment for the antiferromagnetic nanoparticle with absolute value

$$|\mu_{\mathrm{AF}}| = M_{\mathrm{S}} V |\cos\theta_{\mathrm{A}} - \cos\theta_{\mathrm{B}}| \simeq M_{\mathrm{S}} V \delta \sin^2\theta_{\mathrm{B}} \tag{1.45}$$

where M_{S} is the sublattice magnetization. To obtain this last expression it is assumed that θ is small and $\sin\theta$ is expanded. This assumption is valid at low temperatures such that only small values of θ are populated. The precession modes are characterized by angles $\cos\theta_{\mathrm{B}}$=1, 1-ξ, 1-2ξ, ..., 1-(N-1)ξ, where $\xi \simeq \frac{g\mu_{\mathrm{B}}}{2M_{\mathrm{S}}V\delta}$ is the smallest allowed change in $\cos\theta$ and $N = 1/\xi$. At low temperatures, $\sin^2\theta_{\mathrm{B}} \simeq 2\mathrm{n}\xi$ and $|\mu_{\mathrm{AF}}(n)| = M_{\mathrm{S}} V \delta 2n\xi$. When a magnetic field is applied along the easy magnetization axis we have different probabilities, p^+ and p^-, for the magnetic moment to be parallel of antiparallel to the applied field. The thermal average of the magnetic moment is then

$$\langle \mu_{\mathrm{AF}} \rangle = \sum_{n=0}^{N-1} |\mu_{\mathrm{AF}}(n)| p(n) [p^+ - p^-] \tag{1.46}$$

where

$$p(n) = \frac{\exp(-4\alpha n\xi)}{\sum_{n=0}^{N-1} \exp(-4\alpha n\xi)} \quad \text{and} \quad p^{\pm} \simeq \frac{1}{2}\left(1 \pm \frac{|\mu_{AF(n)}| B_{ext}}{\mathrm{k_B} T}\right) \tag{1.47}$$

and $\alpha = KV/\mathrm{k_B}T$. Introducing the expression

$$F(\alpha) = \ln\left(\sum_{n=0}^{N-1} \exp(-4n\alpha\xi)\right)$$

the initial susceptibility can be calculated as

$$\chi \simeq \frac{(M_{\mathrm{S}} V\delta)^2}{\mathrm{k_B} T}\left[\frac{d^2F(\alpha)}{d\alpha^2} + \left(\frac{dF(\alpha)}{d\alpha}\right)^2\right] \tag{1.48}$$

in the CGS system of units. The obtained initial susceptibility increases with temperature. We should stress that in this derivation, modes with zero net magnetic moment as ($\nearrow\swarrow$) have not been taken into account. In addition, the zero point energy is not included in the derivation of the thermal average of the magnetic moment. As a consequence, the magnetic moment tends to zero at $T = 0$.

The susceptibility associated with the population of the uniform mode can also be calculated using statistical mechanical formulae as follows. The energy of this mode when a magnetic field is applied is

$$E_{n,\pm} = (n + 1/2)\hbar\omega_{0,\pm} = \pm g\mu_{\mathrm{B}} H_0 + \hbar\omega_0 \quad \text{where} \quad \hbar\omega_0 = g\mu_{\mathrm{B}} \left[H_{\mathrm{AN}}(2H_{\mathrm{E}} + H_{\mathrm{AN}})\right]^{1/2} \tag{1.49}$$

The magnetic moment of mode n_+ is -(n+1/2)gμ_{B} and that corresponding to mode n_- is (n+1/2)gμ_{B}. Then, the partition function in an applied field H_0 is

$$Z = \sum_{n=0}^{N-1}\left(e^{-\beta(n+1/2)\hbar\omega_{0+}} + e^{-\beta(n+1/2)\hbar\omega_{0-}}\right) = \ldots = \tag{1.50}$$

$$= e^{-\beta\frac{\hbar\omega_{0+}}{2}}\left(\frac{1 - e^{-\beta\hbar\omega_{0,+}N}}{1 - e^{-\beta\hbar\omega_{0+}}}\right) + e^{-\beta\frac{\hbar\omega_{0-}}{2}}\left(\frac{1 - e^{-\beta\hbar\omega_{0-}N}}{1 - e^{-\beta\hbar\omega_{0-}}}\right) \tag{1.51}$$

The variable N was already defined in Mørup derivation. Now,

$$F = \frac{-1}{\beta}\ln Z \quad \text{and} \quad M = -\frac{\partial F}{\partial B} = \frac{1}{\beta}\frac{1}{Z}\frac{\partial Z}{\partial B} \tag{1.52}$$

The susceptibility can then be obtained as,

$$\chi = \left.\frac{\partial M}{\partial H_0}\right|_{H_0=0} = \frac{1}{\beta}\frac{\left.\frac{\partial^2 Z}{\partial B^2}\right|_{B=0} Z_0 - \left(\left.\frac{\partial Z}{\partial B}\right|_{B=0}\right)^2}{Z_0^2} \tag{1.53}$$

The expression $\frac{\partial Z}{\partial B}\big|_{B=0} = 0$ because at $B = 0$ $\omega_{0+} = \omega_{0-} = \omega_0$ so that

$$\chi = \frac{1}{\beta}\frac{\frac{\partial^2 Z}{\partial B^2}\big|_{B=0}}{Z_0} \tag{1.54}$$

that leads for the susceptibility to the expression

$$\chi = \beta\frac{(g\mu_B)^2}{4}\frac{1-2e^{-\beta\hbar\omega_0}-7e^{-2\beta\hbar\omega_0}-(2N+1)^2e^{-\beta\hbar\omega_0 N}+(8N^2+16N+2)e^{-\beta\hbar\omega_0(N+1)}-(4N^2+12N-7)e^{-\beta\hbar\omega_0(N+2)}}{(1-e^{-\beta\hbar\omega_0 N})(1-e^{-\beta\hbar\omega_0})^2} \tag{1.55}$$

We can approach

$$\sum_{n=0}^{N-1} e^{-\beta n\hbar\omega_0} \simeq \frac{1}{1-e^{-\beta\hbar\omega_0}} \tag{1.56}$$

so we get for the susceptibility the following expression

$$\chi = \frac{\beta(g\mu_B)^2}{4\left(1-e^{-\beta\hbar\omega_0}\right)}\left[1+3e^{-\beta\hbar\omega_0}+4e^{-\beta\hbar\omega_0}\frac{1+e^{-\beta\hbar\omega_0}}{1-e^{-\beta\hbar\omega_0}}\right] \tag{1.57}$$

The thermoinduced magnetic moment is parallel to the easy axis. Therefore, the equilibrium susceptibility for a nanoparticle with the easy axis randomly oriented is $\chi = \frac{1}{3}\chi_{\rm th} + \chi_{\rm AF}$, where $\chi_{\rm th}$ refers to that obtained in expressions Eq. (1.48) or Eq. (1.55) or Eq. (1.57). The thermoinduced moment $\mu_{\rm th}$ can be determined from the parallel susceptibility as follows

$$\chi_{\rm th} = \frac{<\mu_{\rm th}^2>_T}{k_B T} \tag{1.58}$$

Fig. 1.12 shows that the magnetic moment calculated through Mørup semi-classical method and the one calculated through the statistical mechanic calculation using the expression Eq. (1.58).

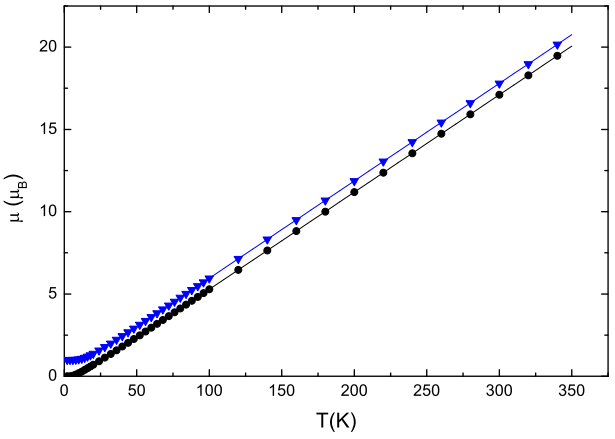

Figure 1.12: μ calculated with semi-classical ($\circ$) and statistical mechanical calculations for infinite N approximation ($\triangledown$).

The data were calculated using parameters similar to that valid for the akaganéite nanoparticles studied in this work. We take H_{AN}=10.5×10^3 Oe, H_E=6×10^6 Oe, M_S=520 emu/cm^3 and a particle volume of V=298.5 nm^3. We notice in Fig. 1.12 that the uniform mode gives at T = 0 a non zero contribution, $\mu(0) = \frac{1}{2}g\mu_B$ for the magnetic moment calculated through statistical method. The dependence of μ with the temperature is similar differences being noticeable at low temperatures between the results obtained by these two calculations.

We can therefore conclude that the semi-classical method is a good approximation. However, for antiferromagnetic systems the statistical mechanical calculation would be more accurate.

Chapter 2

Experimental methods

In this chapter the experimental methods used in the following chapters are briefly described.

2.1 X-ray powder diffraction

X-ray powder diffraction (XRD) was used in this thesis to characterize the crystallographic structure of materials and to determine the average particle size [65].

The XRD measurements were performed at the *Servicio de Difracción de Rayos X y Análisis por Fluorescencia* of the *Universidad de Zaragoza*. We used a D-Max Rigaku diffractometer equipped with a $CuK_{\alpha 1,2}$ (λ=1.54 Å) radiation source. Diffraction patterns were recorded at room temperature. Solid samples were prepared by grinding and spreading the powders onto a glass holder. Liquid suspension samples were previously precipitated and washed with acetone and then dried at room temperature. Crystallite phases present in the sample were determined by comparison with database diffraction patterns. The size of crystalline domains ('XRD particle size' from here on) was estimated by fitting the strongest reflection peak to a Lorentzian. From the fitting we obtain θ and Δ and, by using the Debye-Scherrer's equation, we determine the average size of the nanoparticles.

2.2 Thermo-gravimetric analysis

We used Thermo-gravimetric analysis (TGA) to determine the weight percentage of maghemite in organic ferrofluid samples.

The experiments were performed at the *Servicio de Análisis Térmico* of the *Instituto de Ciencia de Materiales de Aragón (CSIC - Universidad de Zaragoza)*. We used a TGA 5000 apparatus from TA Instruments. These measurements on liquid samples were performed on an alumina sample holder, in nitrogen atmosphere.

2.3 Fourier transform infrared spectra

The IR spectroscopy technique was used together with XRD as a means of identification of compounds in a sample.

In this thesis, Fourier transform infrared spectra (FTIR) were acquired in a Spectrum One (Perkin Elmer) instrument in the *Department of Inorganic Chemistry* of the *Universidad de Zaragoza*. Measurements were carried out on KBr pellets with about 5wt% of sample.

2.4 Atomic emission spectroscopy

We used the Atomic emission spectroscopy to determine the metal content in the samples.

The experiments were performed at the *Laboratorio Central de Análisis* of the *Universidad de Zaragoza*. We used an inductively coupled plasma optical emission spectrometer (ICP-OES) Perkin-Elmer Plasma 40. The samples were dried and dissolved in concentrated HCl.

2.5 Dynamic light scattering

Dynamic light scattering (DLS) was used for measuring the size of particles suspended in a liquid buffer.

The experiments were performed at the laboratory facilities of the *Instituto de Ciencia de Materiales de Aragón (CSIC - Universidad de Zaragoza)*. We used a Zetasizer NanoZS ZEN3600 from Malvern Instruments [66]. The apparatus uses a red laser of wavelength 633 nm and a scattering angle of 173° (backscatter detection). The measurements were performed at room temperature. The samples were previously sonicated and placed in a plastic cell provided by Malvern. Several sample dilutions were used to discard any influence of the concentration in the results. The size distribution profiles were compared with those obtained from electron microscopy in order to discard the existence of aggregates in the liquid samples.

2.6 Electron microscopy

We used electron microscopy in order to obtain images of the sample and information about the reciprocal lattice of the sample.

The scanning electron microscopy (SEM) measurements were performed at the *Servicio Microscopía Electrónica* of the *Universidad de Zaragoza*. We used a Jeol-JSM 6400 microscope with a resolution down to 3.5 nm that works with voltages from 0.2 to 40 kV. This microscope is also equipped with an Electron Back Scatter Diffraction analyzer which provides information on the elemental composition. Samples were prepared embedding the grounded powder in an epoxy resin and polishing it. The obtained images were analyzed by using a Digital Micrograph software to determine the average particle size.

The transmission electron microscopy (TEM) measurements on solid samples were performed either at the *Servicio Microscopía Electrónica* of the *Universidad de Zaragoza* or at the 'CEMES' in Tolousse (France). In the first case, we used a Jeol-2000 FXII microscope

that works with voltages from 20 to 200 kV. Some samples were prepared by grounding the samples in acetone and evaporating drops of the resulting suspension on carbon-coated copper grids. Other samples were prepared by embedding the grounded sample in an epoxy resin and cutting ultrathin slices by ultramicrotomy. Both low and high-magnification images were recorded, the latter revealing details of the crystallite structure.

The measurements of the organic ferrofluid samples were performed at the *Servicios científico-técnicos* of the *Universidad de Barcelona*. We used a Philips CM-30 instrument working at an acceleration voltage of 200 kV. Samples were prepared by putting a drop of the as-prepared maghemite ferrofluid on a carbon-coated copper grid and then drying in air.

Image analysis was carried out with a Digital Micrograph software. We determine the average particle diameter by fitting a gaussian to the particles-size histogram. Additionally, we usually obtained the mean number of particles N per gram of iron oxide as:

$$N = \frac{\int n(V)dV}{\int n(V)\rho V dV} \tag{2.1}$$

where ρ is the density of iron oxide phase. Using N we also calculated the number of Fe ions per particle.

2.7 Small angle X-ray scattering

In this thesis, small angle X-ray scattering (SAXS) has been employed to get information about average sizes as well as nanoparticle arrangements.

X-ray scattering is named as 'small-angle X-ray scattering' (or SAXS) when the measurement is confined to angles within the range between ~ 0.1 and 10 degrees, these limits depending on the particular instrumental setup [67–69]. Most of SAXS experiments are performed using X-ray wavelengths λ ranging from 0.6 Å to 3.25 Å and they provide useful information about heterogeneities in electron density sized within the range ~ 0.5 nm to 50 nm.

A small-angle scattering instrument, shown in Fig. 2.1, consists of a radiation source, a collimator (usually a monochromator), the specimen block and the detector of the scattered radiation.

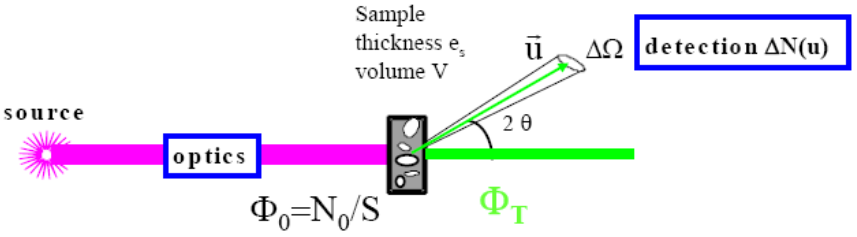

Figure 2.1: Schematic view of a typical scattering experiment.

The detector measures the counts in the direction u in a solid angle $\Delta\Omega$,

$$\frac{\Delta N}{\Delta\Omega} = T\Phi_0 \frac{d\sigma}{d\Omega}(\vec{u}) \tag{2.2}$$

where $T = \Phi_T/\Phi_0$ is the transmission of the sample and $d\sigma/d\Omega$ is the differential scattering cross-section, measured in cm^2. The scattered intensity is the differential scattering cross-section per unit volume,

$$I = \frac{d\Sigma}{d\Omega} = \frac{1}{V}\frac{d\sigma}{d\Omega}(\vec{u}) = \frac{\Delta N}{N_0}\frac{1}{Te_s\Delta\Omega} \tag{2.3}$$

The standard unit is cm^{-1}.

The intensity is collected as a function of the scattering angle 2θ. Elastic interactions are characterized by zero energy transfers, such that the final wave vector $\vec{k}_f$ is equal in modulus to $\vec{k}_i$. The momentum transfer or scattering vector $\vec{q}=\vec{k}_i-\vec{k}_f$ is defined by $q=4\pi\sin\theta/\lambda$. The standard unit for q is $Å^{-1}$. The scattered intensity $I(q)$ is the Fourier Transform of $g(r)$, the correlation function of the electronic density $\rho(r)$, which corresponds to the probability to find a scatterer at position r in the sample if another scatterer is located at position 0. Then, the experiments reveal the spatial correlations in the sample. The number of photons scattered by one sample is proportional to its total volume V and to its electronic contrast. In the simple case of a binary system such as an ensemble of scattering objects of density ρ_1 embedded in a solvent of density ρ_2, the electronic contrast is $\Delta\rho = \rho_1 - \rho_2$ (cm^{-2}). The higher the contrast between particles and solvent, the more intense the scattered signal will be. A typical small angle scattering intensity profile is shown on Fig. 2.2. Intuitively, a

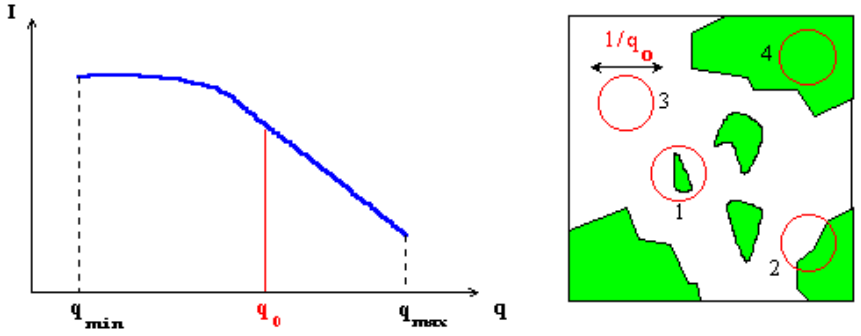

Figure 2.2: Left: Example of scattering intensity profile measured between q_{min} and q_{max}. Right: Binary sample and 'q-window' corresponding to a measurement at a given q_0. The contrast is equal to zero in cases 3 and 4 and different from zero in cases 1 and 2.

measurement made at a given q_0 allows to investigate the density fluctuations in the sample on a distance scale $D_0=2\ \pi\ /q_0$. This is equivalent to observe the system through a $2\ \pi\ /q_0$ diameter 'window' in real space as shown on Fig. 2.2. The q-range is usually divided into three main domains as illustrated in Fig. 2.3. The window defined in the high-q domain (case 3) is very small so that there is a contrast only at the interface between the two media. It is called the Porod's region and gives information about the interfaces present in the sample. In the intermediary region, case 2, we can obtain information about the size, shape and internal structure of single particles. Finally, when the observation window is very large (low-q domain, case 1), the structural order can be obtained which allows to investigate the interactions in the system.

The analysis of small-angle scattering data can be performed following three different approaches. The first one, so-called direct method of interpretation, is used when some *a*

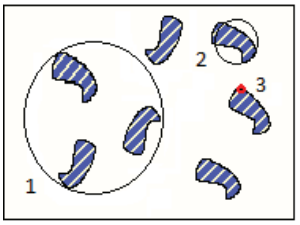

Figure 2.3: Three q-domains define correspondingly three 'windows' of diameter 2 π /q diameter in real space. Each q-domain provide different information about the characteristics of the sample.

priori information on the object is available and permits to recover directly its structure, i.e., the scattering density distribution. This approach is used mainly in the analysis of the scattering of non-complex systems. There are some available software packages for this kind of analysis, such as GNOM developed by A. V. Semenyuk and D. I. Svergun [70, 71], which searches for the density distribution function that fits the experimental data using some initial conditions provided by the user. The second approach is used to determine structural parameters of the system and it is based on the evaluation of the invariants of the scattering curve. These are calculated from approximate expressions of the scattering intensity that are applicable in certain q regimes. In the range $qR_g<1$ the intensity of a system composed of N randomly oriented and spatially uncorrelated nano-objects follows the Guinier law,

$$I(q) = I(0)\exp\left(-\frac{\langle R_g\rangle^2 q^2}{3}\right) \tag{2.4}$$

where $I(0) = (\rho_1 - \rho_2)^2\phi(1-\phi)\langle V_1\rangle$ is the extrapolation of the intensity at $q \to 0$, V_1 is the average volume of the particle and ϕ is the volume fraction. R_g is the radius of gyration of the nano-object which in the case of a homogeneous and spherical object of radius R is given by R_g^2=3/5R and in cylinders with diameter D and height H is $R_g^2 = (D^2/8) + (H^2/12)$. Then, the beginning of the scattering curve provides information about two parameters, namely $I(0)$, characterizing the total amount of scattering matter, and R_g, bearing information on its distribution with respect to the particle center of mass. In the high q region, when two media are separated by a sharp interface, the asymptotic intensity follows the Porod's law,

$$\lim_{q\to\infty} I(q) = \frac{2\pi(\Delta\rho)^2}{q^4}\frac{S}{V} \tag{2.5}$$

where S is the nanoparticle surface area. There are more sophisticated expressions of this law for complex interfaces. Porod' s law applies to either, dilute or concentrated systems of isolated nano-objects, however in the particular case of thin sheets or very narrow cylinders the asymptotic intensity is proportional to $1/q^2$ and $1/q$, respectively [68]. The behavior of $I(q)$ at high q is often analyzed using a Porod plot ($I(q)q^4$ versus q^4), that according with Eq. (2.5) $I(q)q^4$ is expected to become asymptotically constant in the high q limit. Let us remark that scattering intensity must be in absolute units for the determination of the interface surface area using Eq. (2.5). Then, the asymptotic behavior of $I(q)$ provides information about the surface scattering. Finally, the Porod invariant Q is obtained from the integral of the scattering intensity in reciprocal space,

$$Q = \int_0^\infty q^2 I(q)dq = 2\pi^2\phi_1(1-\phi_1)(\Delta\rho)^2 \tag{2.6}$$

Let us notice that Q only depends on the electron density contrast factor and on the volume fractions ϕ occupied by both phases, but not on their detailed geometrical configuration.

For example, in structural transformations in which the electron densities and the volume fractions of both phases are constant, the integral Q remains constant even if the structure and, consequently, the shape of the scattering intensity curves vary. Again, the calculation of the Porod invariant requires that the scattering intensity is in absolute units. The integral Q is very useful for the determination of the volume fraction, from which we can derive the concentration of the material. The right volume fraction is obtained from Eq. (2.6) only in absence of aggregates. The scattering of clusters is reflected as an additional contribution to the intensity that appears around the angle position corresponding to the average cluster size. In this situation, Eq. (2.6) would give larger ϕ values than the real ones. The comparison between calculated and real concentrations provides information about the formation of particle clusters. In those systems where particles are not correlated and $\phi << 1$, we can make use of the expression of the extrapolated intensity $I(0) \simeq (\Delta\rho)^2\phi_1 V_1$ and Eq. (2.6), $Q = 2\pi^2\phi_1(1-\phi_1)(\Delta\rho)^2 \simeq 2\pi^2\phi_1(\Delta\rho)^2$ to obtain the 'Porod' volume of the particle,

$$V_1 = 2\pi^2 \frac{I(0)}{\int I(q)q^2 dq} \tag{2.7}$$

This expression does not require the absolute intensity values. The last approach is one of the most widely used in the interpretation of SAXS data. It is based on the fitting of the scattering intensity with a unified equation proposed by Beaucage [72, 73],

$$I_p(q) = G_1 \exp\left(-\frac{R_g^2 q^2}{3}\right) + B_1 \left(\frac{\{\mathrm{erf}\left[qR_g/\sqrt{6}\right]\}^3}{q}\right)^p \tag{2.8}$$

where G_1 is the Guinier prefactor,

$$G_1 = N\left(\rho_1 - \rho_2\right)^2 V_1^2 \tag{2.9}$$

and N is the number of particles per unit volume. B_1 is a prefactor specific to the type of power-law scattering, defined according to the regime in which the factor p falls. This factor describes the power law decay of the scattered intensity and depends on the dimension of the scattering surface. For $p = 4$, B_1 is the Porod constant defined as

$$B_1 = 2\pi N\left(\rho_1 - \rho_2\right)^2 S \tag{2.10}$$

This approach successfully describes scattering from polydisperse nano-objects with different shapes and from multiple-size structures [72]. The above expression yields the values of R_g, B_1 and G_1, that can be used to calculate the mean diameter and the standard deviation of the particle distribution [74].

The experiments were performed at the *Beam Lines ID01* ($\lambda = 1.77$ Å) and *BM16* ($\lambda = 0.97$ Å) of the *European Synchrotron Radiation Facility (ESRF)*. Several sample detector distances were used in order to cover a broad angle range. In some experiments in BM16 line, the CCD-detector was off-centered to collect data at the highest possible angle. Various counting times were used and several runs performed for every sample in order to have better statistics. Solid samples were prepared by grinding and pressing into pellets. As prepared transparent films were also observed for some samples. In the case of liquid suspensions, the solvent and empty cell were also measured for absolute data extraction. A PRIMUS software [75] was used in data treatment (subtraction, averaging of different runs...). Average particle sizes were obtained using GNOM software [71].

SAXS data from ID01 beamline were processed with macro software provided by ID01 to get the absolute intensity profiles, as well as for error bars estimations. The intensity in BM16 experiments was calculated in absolute units (cm^{-1}) by a scaling method using water as a reference. The procedure was as follows: first, scattering intensities from the CCD

detector were azimuthally averaged by using macros provided by BM16. Then, the scattered intensity is normalized with the transmitted intensity (I_1). Finally, the water scattering intensity shown in Fig. 2.4 is determined, subtracting the cell contribution and normalizing by cell thickness. The extrapolated value of the scattered intensity is correlated with the

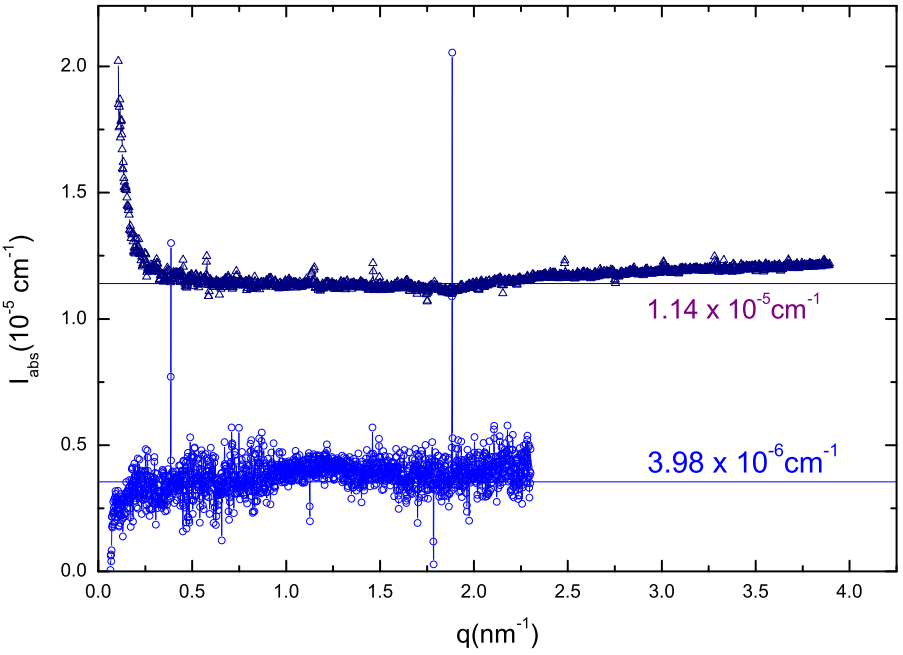

Figure 2.4: Intensity profiles for the water at sample to detector distances of 2.5 m (▵) and 4 m (○).

constant scattering intensity of water [76] at room temperature, $I(293\ \mathrm{K}) = 1.632 \times 10^{-2}$ cm^{-1}.

2.8 Differential scanning calorimetry

In this thesis, differential scanning calorimetry (DSC) was used to confirm Néel temperature estimation from magnetization measurements.

The experiments were performed at the *Servicio de Análisis Térmico* of the *Instituto de Ciencia de Materiales de Aragón (CSIC - Universidad de Zaragoza)*. We used a commercial Q1000 apparatus from TA instruments. The instrument was calibrated in temperature and energy using an Indium sample. Additionally, a standard Sapphire sample was measured in the same temperature range as that used for the samples in order to calibrate the DSC for absolute heat capacity measurements. The sample holder was an aluminum pan.

2.9 Specific absorption rate

In this thesis, we measured the specific absorption rate (SAR) of the ferrofluids to determine the effective relaxation time of the particles at frequencies $f \sim$ kHz. The specific absorption rate is defined as the thermal power per mass unit dissipated in the presence of an alternating magnetic field. SAR is measured according to the pulse heating method,

$$SAR = \frac{1}{m_{\mathrm{NP}}} \cdot \mathrm{C} \cdot \frac{\Delta T}{\Delta t} \tag{2.11}$$

where m_{NP} is the mass of magnetic material, C the heat capacity of the whole sample and ΔT the temperature increment during the field application interval Δt. The installation, shown in Fig. 2.5, consists of an ac magnetic field generator, a sample space delimited by an isolating material, temperature sensors and a data acquisition system. The sample is hanged by

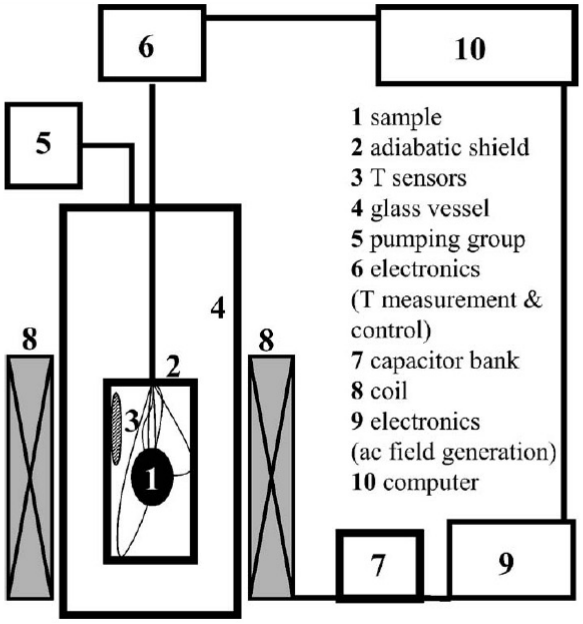

Figure 2.5: Schematic view of SAR setup. Image taken from Ref. [77].

thermal isolating threads from the adiabatic shield, which surrounds the sample. The shield is kept at the same temperature as the sample in order to ensure adiabatic conditions. It is made of alumina to minimize the effect of Foucault currents, which arise in the presence of alternating magnetic fields. The coil is placed outside the vacuum environment to prevent any heating in the sample environment produced at high field amplitudes. A detailed description of the magneto-thermal installation can be found in Refs. [77, 78].

The experiments were performed at the laboratory facilities of the *Instituto de Ciencia de Materiales de Aragón (CSIC - Universidad de Zaragoza)*. We used the special-purpose magneto-thermal setup [77, 78] working under adiabatic conditions previously described. Measurements were performed on liquid samples at average temperatures of 315 K. The specific absorption rate is measured by applying an oscillating magnetic field of amplitude 3 kA/m and frequency f of 109 kHz. We used a quartz sample holder sealed with a vacuum-proof solvent. The contributions to the SAR of the carrier liquid, the quartz sample holder

and the sealant were taken into account. The temperature increments measured were small due to the low nanoparticle concentration in the ferrofluid and the relatively high heat capacity, so that final SAR values were obtained by averaging between 5 to 9 heating steps. According to R. E. Rosensweig [79] SAR can be expressed as:

$$SAR(\mathrm{W/g}) = \mu_0 \pi f H_0^2 \chi''/\rho \quad \text{with} \quad \chi'' = \chi_0 \frac{\omega\tau_{\mathrm{eff}}}{1+(\omega\tau_{\mathrm{eff}})^2} \tag{2.12}$$

where ρ is the mass density of the active material, χ_0 is the equilibrium susceptibility, $\omega = 2\pi f$ and τ_{eff} is the effective relaxation time of the particles.

2.10 Magnetic experimental techniques

The magnetic measurements were performed using three different setups that are briefly described here.

The ac and dc susceptibility measurements under magnetic fields up to 5 T were performed in superconducting quantum interference (SQUID) magnetometers of Quantum Design Inc [80, 81]. Basically, this device consists of a superconducting magnet inserted in helium bath, a temperature and magnet control system and a SQUID-based dc magnetometer and ac susceptometer. A schematic draw is shown in Fig. 2.6. The sample is suspended

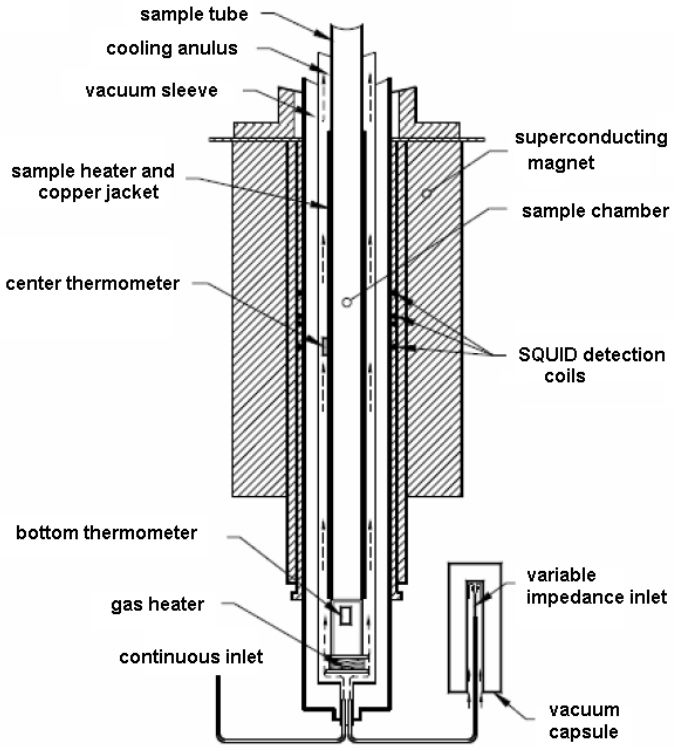

Figure 2.6: Schematic view of the SQUID magnetometer.

in a central chamber isolated from the helium bath, allowing the temperature of the sample

to be controlled over the temperature range 1.8-400 K, while the detection coils and the drive coils remain in liquid helium. The system works under applied fields up to 5 T.

In the dc-magnetization measurements the sample is moved in a series of discrete steps through the detection coils. A change in the sample's position causes a change in the flux within the superconducting detection coil, thereby changing the current in the superconducting detection circuit. The detection coils are configured as a second-order gradiometer, consisting of an upper coil turned clockwise, two coils turned counter-clockwise and a bottom coil turned clockwise. This configuration cancels the signal produced by fluctuations in the large magnetic field of the superconducting magnet. The detection coils are inductively coupled through a superconducting isolation transformer to a SQUID-based detection system. The SQUID act as a flux-to-voltage convertor so that measures directly the change in flux as the sample moves through the superconducting detection coils. This voltage is recorded at each of the sample positions, being the raw data of the dc measurement. The longitudinal SQUID calibration factor is used to convert the measured voltages into magnetic moment (Palladium is used to determine this calibration factor). The resolution is of the order of 10^{-7}-10^{-8} emu. The ac susceptometer consist of an ac drive system and a feedback system in addition to the detection coils and the SQUID. In an ac susceptibility measurements the high sensitivity of the SQUID is combined with the noise rejection inherent to ac techniques. In the ac-susceptibility measurements an oscillating magnetic field is applied to the sample; the change in flux seen by detection circuit is due only to the change of the magnetic moment of the sample as it responds to the applied ac field. From these measurements we obtain the complex susceptibility. The data result from two separate measurements, one in the lower gradiometer coil and another in the center coil. First, the sample is moved to the lower coil where the system automatically nulls any noise and removes dc offset and the signal of the sample itself, to a selected user noise level. The remnant signal in the bottom coil is then measured during a time specified by the user. The sample is then moved into the center coil of the gradiometer and the signal is measured. The difference between these two measurements is about three times the actual moment of the sample, since the center coil has opposite orientation to the lower coil and twice as many windings.

High-field magnetization isotherms have been measured with the vibrating sample magnetometer VSM option of the physical property measurement system (PPMS) [82]. This option has a sensitivity of 10^{-6} emu (at 1 Hz). The option consists of a VSM linear motor transport (head) for vibrating the sample, a coilset puck for detection and the electronics for driving the linear motor transport and detecting the response from the pickup coils. The measurement is accomplished by oscillating the sample near a detection (pickup) coil and synchronously detecting the voltage induced in a pickup coil. The time dependent induced voltage

$$V_{\text{coil}} = \frac{d\Phi}{dt} = \frac{d\Phi}{dz}\frac{dz}{dt} = 2\pi f C \mu A \sin(2\pi f t) \tag{2.13}$$

where Φ is the magnetic flux enclosed in the pickup coil, C is a coupling constant, μ is the magnetic moment of the sample, A the amplitude of oscillation, f is the frequency of oscillation and z is the vertical position of the sample. The voltage induced in the pickup coil is amplified and lock-in detected in the VSM detection module.

The experiments were performed at the *Servicio de Instrumentación Científica - Área Medidas Físicas* of the *Universidad de Zaragoza*. Magnetic measurements were performed using commercial PPMS system and SQUID magnetometers MPMS-XL and MPMS-5S from Quantum Design. The samples were hold in capsules for the measurements. The diamagnetic contributions of polymer matrix, solvent and capsule were determined in independent measurements. All of them vary linearly with the applied field and are temperature independent. Their contribution was subtracted from all the sample experimental data.

We also performed high field magnetization measurements at the *High Field Magnet Laboratory (HFML)* facility in Nijmegen. Magnetization curves were measured as a function of magnetic field up to 30×10^4 Oe at different temperatures using an extraction magnetometer in a Bitter magnet [83]. The sensitivity of the extraction magnetometer is about 10^{-3} emu. The measurement device yields magnetization as a voltage output that it is converted to electromagnetic units (emu) by using a calibration factor. The samples were enclosed in teflon sample-holders for the measurements. The diamagnetic contribution from the sample-holder was also analyzed and it was removed from the experimental data.

The results included in the following chapters are given in gaussian (CGS) units. That is, magnetic field is expressed in Oersted (Oe, 1 Oe = $10^{\ 3}$ / 4π A/m) and magnetic moment in electromagnetic units (emu, 1 emu = 10^{-3} Am^2). The magnetization, usually defined as the magnetic moment per volume unit, is given in the following chapters as magnetic moment per gram of magnetic material. Accordingly, the susceptibility would be given per gram of magnetic material and expressed in emu/Oe g units.

Chapter 3

Akaganéite polymer nanocomposites

This chapter investigates the magnetic properties of a series of akaganéite polymer nanocomposites prepared by 'in situ' precipitation of akaganéite nanoparticles in a polymer media. A controlled precipitation is achieved by using a polymer matrix, polyvinylpyridine, containing N-base functional groups that form coordination bonds with iron ions. The resulting nanocomposites contain isolated rod-like nanoparticles organized in parallel planar arrays distributed within the polymer matrix. Magnetic studies show two sources of magnetic moment in akaganéite nanoparticles: 1) finite size effects with a characteristic blocking temperature below 2 K; and 2) a deficient Cl^- occupancy, with a characteristic blocking temperature around 18 K.

3.1 Introduction

In their several crystalline forms, iron oxides are valuable materials for a variety of applications [18]. In particular, akaganéite (β -FeOOH) is present in pharmaceutical formulations for the treatment of anaemia [84]. It is also used in environmental applications [85, 86] and catalysis [87] thanks to its capacity for ion and vapor adsorption. Though not frequently, akaganéite is found in soils [88, 89] and possibly in other planets [90, 91]. Moreover, akaganéite is used as a precursor in the production of other iron oxide phases such as hematite [92], goethite [93] and magnetite [94], in order to obtain particle morphologies that are unusual in these iron oxide phases. In this way, akaganéite is indirectly useful in industrial and biomedical applications associated to other iron oxide phases. Besides industrial applications, akaganéite is also interesting in basic science, mainly in geology, corrosion, colloids and magnetism. For instance, an open issue in magnetism is the variation of magnetic properties of bulk materials when their size is reduced to the nanometer range. This phenomenon has been extensively studied in ferromagnetic materials but rarely in antiferromagnetic ones. As a characteristic antiferromagnet, akaganéite can be a suitable model material in these studies. For this purpose, nanocomposites would be the ideal samples, since particles should be isolated in order to distinguish between intrinsic particle properties and collective effects. The obtained nanocomposites have been used in detailed magnetic studies that will be described in following chapters. Nevertheless, some novel features about akaganéite magnetic

behavior concerning the influence of Cl^- ions are analyzed in this work.

3.2 Synthesis

Akaganéite has a monoclinic crystal structure [19, 20, 95, 96] formed by square channels of double octahedra chains that are hold by interstitial Cl^- ions. The Cl^- content may vary with the preparation conditions, but below a threshold concentration the structure collapses. Thus, akaganéite is usually prepared by hydrolysis of $FeCl_3$ aqueous solutions at moderate temperatures. The pH must be slightly acidic (pH<5) to avoid the formation of more stable phases, such as hematite and goethite [97, 98]. Akaganéite has also been obtained by hydrothermal synthesis [99] and by addition of NaOH to $FeCl_2$ solutions [100]. For all these methods, particles are usually rod-like single crystals with a length of several tenths of micron [101] that, concerning magnetic properties, can be considered as bulky particles. Some additives and organic solvents [102–106] may induce the formation of akaganéite at a high pH. In these conditions, the particle size is reduced to a few nanometers and aggregation is favored. A convenient method to control aggregation and particle size is to prepare akaganéite particles in a template, such as a polymer. However, there are few examples of akaganéite polymer nanocomposites in the literature. Dextran and other polysaccharide have often been used, but this is more because they are an adequate encapsulation for biomedical applications, such as anaemia therapy, [106–110], because of their templating capacity. Other matrixes used for akaganéite nanocomposites are assemblies of polyions [111] and nanoporous alumina [112].

This chapter focuses on akaganéite-polymer nanocomposites. Among the numerous routes to prepare magnetic polymer nanocomposites [25], in situ precipitation has been our choice, since it yields homogeneous materials and profits from the moulding effect of the polymer. In this route, the matrix is mixed with a molecular metal precursor and the particles are grown inside the precursor-polymer compound by addition of a precipitating agent [26–29]. The polymer used here is poly(4-vinylpyridine) (PVP), that has nitrogen base groups that form coordination bonds with iron ions. In this way, the hydrolysis reaction is carried out in a controlled manner. This method has recently been employed successfully for the production of maghemite nanocomposites [30]. In that case the precipitating agent was sodium hydroxide and the precursor salt was iron bromide. In the present case the precipitating agent is the same while the precursor is iron chloride.

Inorganic reagents and PVP polymer (60.000 D) were purchased from Aldrich. Gels of iron-PVP coordination compounds were prepared by dissolving 0.2 g of PVP in 4 mL of water/acetone (1:1), mixing this solution with 2 mL of 1M $FeCl_3{\cdot}6H_2O$ solution in the same solvent and drying first in air and then in an oven at 60 °C for 2 h. Akaganéite nanocomposites were prepared by immersing the iron-PVP coordination compound in a volume of 1 M NaOH solution for a Fe/OH ratio of 1:3, washing with water, drying at room temperature and then in an oven at 150 °C.

Two nanocomposite samples were prepared by the procedure described above with a [Fe]/[pyridine] ratio = 1.05. The first sample, NC_{wash}, was extensively washed with water after the treatment with NaOH, whereas the second sample, NC_{Cl}, was just slightly washed. The bulk akaganéite sample was prepared by the spontaneous oxidative hydrolysis of $FeCl_2$ solutions as previously proposed in the literature [18, 100]. One litter of 0.1 M solution of $FeCl_2{\cdot}4H_2O$ was aged inside a closed vessel in an oven at 70 °C for 1 month. The yellow precipitate was filtered, washed with water, dried first at room temperature, then in an oven at 50 °C and finally stored in a sealed flask.

3.2.1 Mechanisms of particle formation

The hydrolysis of iron ions may lead to a variety of crystalline phases depending on the precipitation conditions and the precursor iron salt by a process that involves several intermediate iron species. Concerning the akaganéite phase, it is formed in iron aqueous solutions only in the presence of chloride ions, slightly acidic solutions and moderate temperatures. Nucleation and growth proceed by two different hydrolysis reactions, namely olation and oxolation. The process has been explained by Bottero et al [113] and it can be summarized as follows: 1) formation of iron dimers and trimmers 2) condensation into Fe24 polycations (with the same local structure as akaganéite), 3) arrangement of Fe24 clusters into linear chains, 4) chain ramification, 5) precipitation of hydrated low density amorphous particles, 6) condensation into crystalline particles. Obviously, it is difficult to control this process, although it is known that it is drastically affected by the presence of iron ligands, such as PO_4^{3-} [114].

The strategy proposed here to control akaganéite precipitation is to perform the process in a restrictive environment. There are three factors that may contribute to growth restriction in iron-PVP system: 1) the growth medium is a solid matrix and therefore ion diffusion is slowed down with respect to liquid media, 2) the matrix contains pyridine groups that interact with iron growing units and with the particle surface by means of N-Fe coordination bonds and 3) the pyridine groups are deprotonized before the onset of precipitation, becoming hydrophobic. This third factor can be determinant in the particle growth process. As it is explained in our previous report [30], the initially homogeneous iron-polymer gel collapses when the pyridine groups become hydrophobic. The new microstructure would be no longer uniform in the nanometer scale, but, most probably it would be partitioned into hydrophilic and hydrophobic regions encapsulating the iron ions. Thus, the subsequent growth process will be restricted by the amount of iron ions contained in each hydrophilic region. This mechanism explains the small particle size and the absence of aggregates. Besides, it will help to reduce the particle size dispersion.

3.3 Physical characterization

3.3.1 XRD

X-rays powder diffraction was performed in a Rigaku D-max B diffractometer. Fig. 3.1 shows XRD patterns from NC_{wash} and NC_{Cl} composite samples, PVP polymer and precipitated akaganéite powders. The nanocomposite XRD patterns show a very broad peak around 22°, which is also observed in the polymer pattern and some narrower peaks, which are in turn present in akaganéite powder pattern, at angles corresponding to those of akaganéite crystal structure. The differences in relative peak intensities between powders and nanocomposites patterns and the reference pattern are probably due to particle shape effects. The pattern of sample NC_{Cl} shows additional sharp peaks that correspond to NaCl crystal structure revealing that the washing was insufficient to eliminate this salt from the nanocomposite. An analysis by atomic absorption yielded 22wt % of Fe and 4wt % of Na in this sample. Assuming a percentage of adsorbed water ~15wt% we can determine the weight percentage for the polymer as ~50wt%.

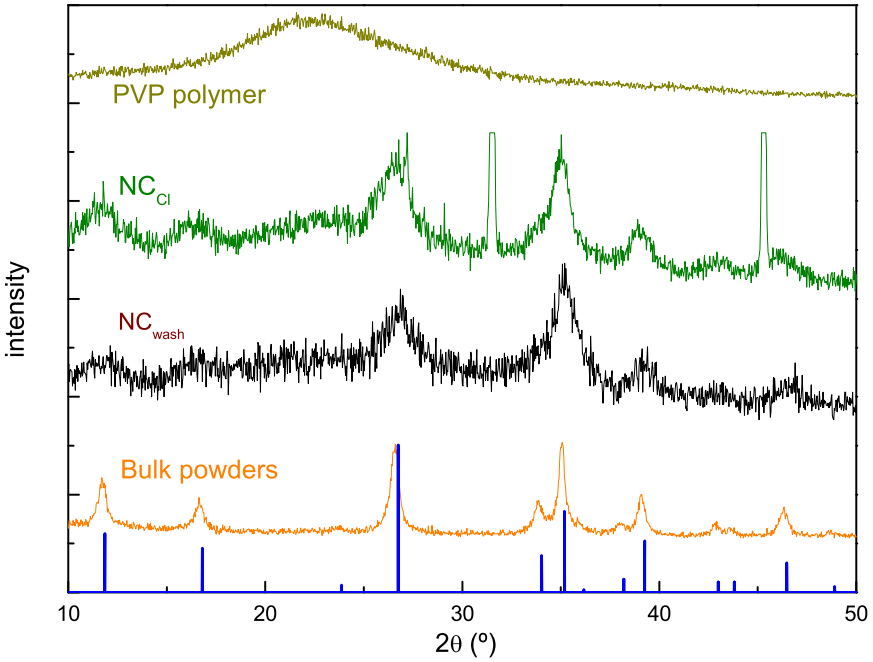

Figure 3.1: XRD patterns of akaganéite database reference (β-FeOOH), akaganéite nanoparticle powders from spontaneous precipitation, nanocomposite samples NC_{wash}, NC_{Cl} and PVP polymer.

3.3.2 FTIR

Fourier transform infrared spectra were taken on KBr pellets using a Perkin Elmer Spectrum One instrument. Fig. 3.2 shows FTIR spectra of pure akaganéite powders, PVP and nanocomposite samples. The spectrum of akaganéite powders shows broad bands at 1623 cm^{-1}, 850 cm^{-1}, 683 cm^{-1} and 411 cm^{-1} and shoulders at 630 cm^{-1} and 473 cm^{-1}, which are close to wave number values reported for this compound [115–120]. The band at 1623 cm^{-1} can be assigned to bending vibrations of structural water bound to different sites [116, 117]. The band at 850 cm^{-1} and shoulder at 630 cm^{-1} correspond to H-O–Cl libration vibrations (850+826 cm^{-1}, 642 cm^{-1} in ref [118, 120]). The shoulder at 473 cm^{-1} and the strong band at 411 cm^{-1} can be related to Fe-O translational modes (479, 424 cm^{-1} in ref [118]) or to Fe-O-Fe symmetric stretching vibrations [117, 119]. The band at 683 cm^{-1}, often assigned to OH libration vibrations, has recently been considered as an artefact [119]. Actually, there is some disparity between reported values for akaganéite IR bands that can be due to different Cl^- content in the samples [120]. For instance, ref [105] reports bands at 850+820 cm^{-1}, 650 cm^{-1}, 487 cm^{-1} and 420 cm^{-1}, whereas Ref. [104] finds bands at 848 cm^{-1}, 633 cm^{-1} and 404 cm^{-1}. The spectrum of the nanocomposite sample can be interpreted as the sum of polymer and powder spectra. Characteristic bands of akaganéite powders are clearly distinguishable,

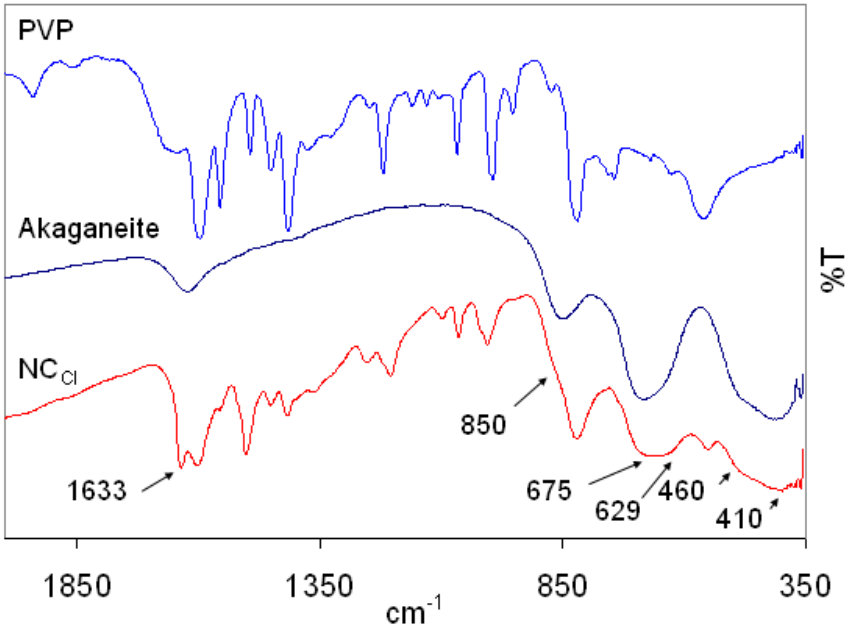

Figure 3.2: FTIR spectra of nanocomposite sample NC_{Cl}, akaganéite nanoparticle powders from spontaneous precipitation and PVP polymer.

as indicated in figure 3.2. No bands are observed from any other iron oxide phase apart from akaganéite.

3.3.3 Electron microscopy

Transmission electron microscopy was performed with a Jeol-2000 FXII microscope, with point-to-point and line-to-line resolutions of 2.8 Å and 1.4 Å, respectively. Samples for TEM observations were prepared in two different ways: 1) grounding the nanocomposites in acetone and evaporating drops of the suspension on carbon-coated copper grids; and 2) embedding the grounded composite in an epoxy resin and cutting ultrathin slices by ultramicrotomy. Both low and high-magnification images were recorded, the latter revealing details of the crystallite structure.

Figure 3.3 shows a TEM image of akaganéite nanocomposite sample NC_{wash} after grinding in a mortar. The particle density is very high and therefore particle shape is only distinguished on the grain edges. The image shows rod-like particles with average length and thickness of 23.7±5.5 and 5.1±1.1 nm, respectively. These dimensions are smaller than those found in akaganéite powders from slow hydrolysis of iron (III) chloride solutions whose typical dimensions are between 0.2-0.5 μm in length and 0.02-0.1μm in width [18].

Figure 3.4 shows a TEM image of a grounded sample NC_{Cl}. The particles are also rod-like with average length and width 17.9±5.7 and 5.4±1.5 nm, respectively.

The Cl/Fe atomic ratio in NC_{wash} and NC_{Cl} samples estimated from EDS analysis over the nanoparticles was 0.33 and 0.78, respectively, indicating that washing effectively removed Cl^- ions from the akaganéite nanoparticles.

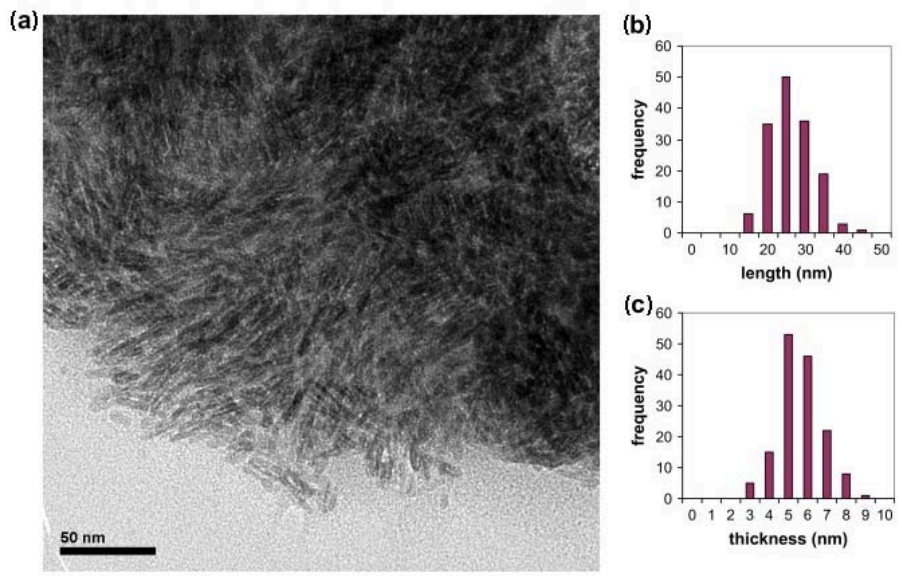

Figure 3.3: (a) TEM image of grounded akaganéite/PVP nanocomposite sample NC_{wash}; (b) histograms of particle length and (c) particle width.

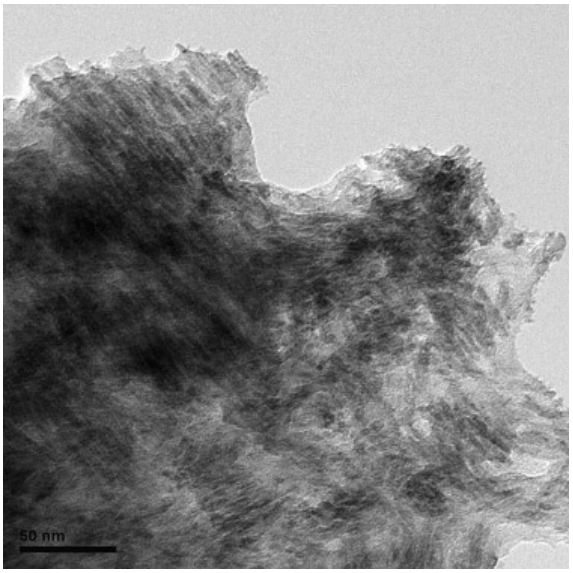

Figure 3.4: TEM image of grounded akaganéite/PVP nanocomposite sample NC_{Cl}.

High-magnification images enabled us to measure the interplanar atomic distances of nanoparticles with different orientations. One of these images is shown in Figure 3.5 together with its FFT pattern. Lattice plane distances of 1.87, 2.03 and 2.62/2.66 were measured, corresponding to (4 4 0), (1 5 0) and (4 0 0) planes of akaganéite crystal structure [19, 20, 95].

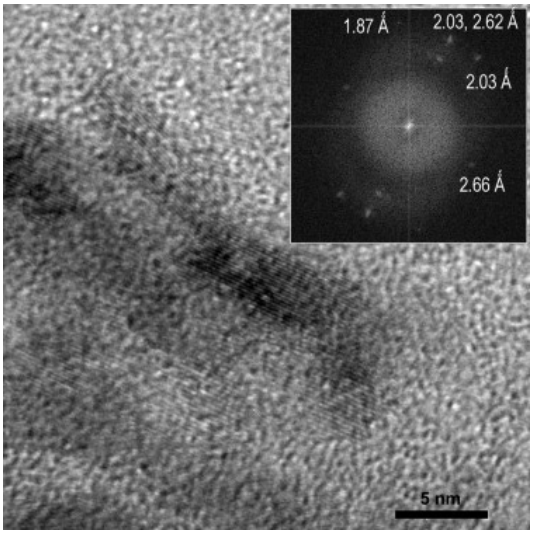

Figure 3.5: HRTEM image of a group of nearly parallel needle particles showing the same direction of elongation. In the inset, electron diffraction pattern of the area.

Analysis of different nanoparticle images yield other distances, such as 2.35/2.36, 2.79/2.80 and 3.02/3.03, that can be assigned to planes (2 4 0), (1 1 1) and (0 0 1), respectively.

In order to determine the disposition of the particles within the matrix, ultrathin slices of sample NC_{Cl} were observed by TEM as shown in Fig. 3.6. It is observed that, at short

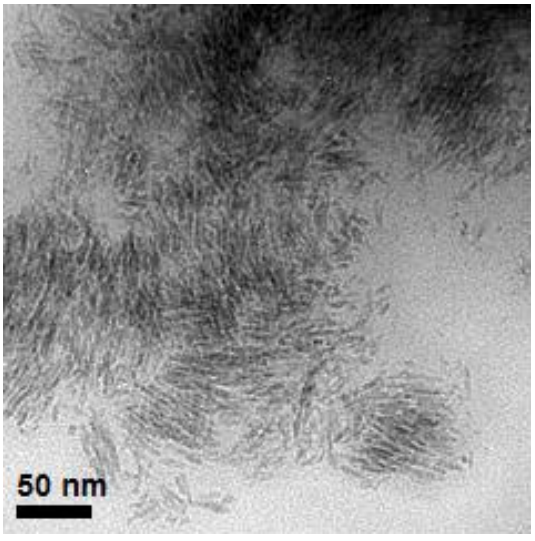

Figure 3.6: TEM images of an ultrathin slice of akaganéite/PVP nanocomposite sample NC_{Cl}.

length scales, the particles are arranged parallel, forming sheets.

3.3.4 SAXS

SAXS experiments were carried out at beamline ID01 of the European Synchrotron Radiation Facility (ESRF). Nanocomposite samples for small-angle X-ray scattering measurements were prepared by grounding the as prepared films in a mortar and then pressing the grains into pellets having an approximate thickness of 0.2 mm. The nanostructure of composite samples was examined by SAXS following a procedure similar to that previously applied to maghemite/PVP nanocomposites [121].

Fig. 3.7 shows SAXS plots of pellets of powdered polymer and composite samples. The

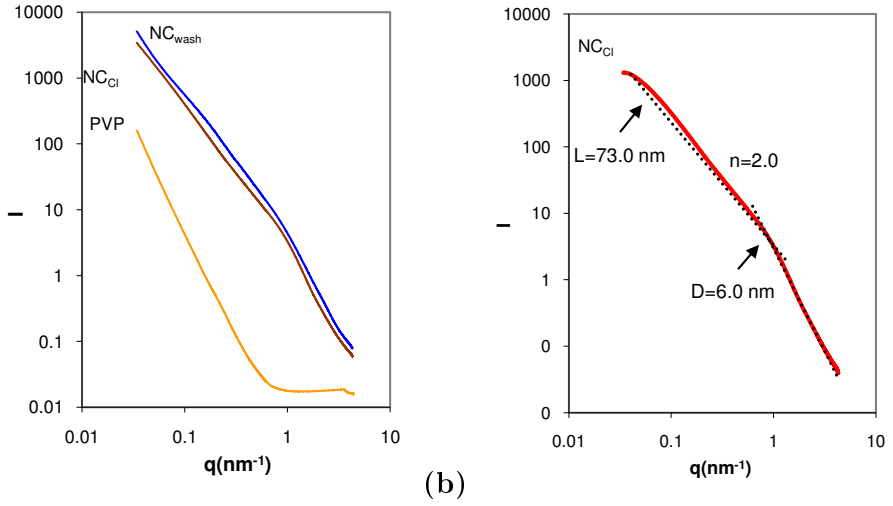

Figure 3.7: **(a)** SAXS log plots of pellet samples of poly(4-vinylpyridine) polymer (PVP) and akaganéite/PVP nanocomposite samples NC_{wash} and NC_{Cl}; **(b)** SAXS curve of NC_{Cl} sample after subtracting the polymer scattering.

polymer curve shows a region of constant intensity at higher q values, implying that the structure is homogeneous in the corresponding length scale. At lower q values, the scattered intensity follows a region of linear increase with a slope of 3.3. This power-law behavior is not far from the typical scattering behavior of smooth surfaces (n=4), usually referred as Porod regime [122] and can be assigned to surface scattering from folded polymer chains [121]. The SAXS curves of the two nanocomposite samples are very similar to each other, consisting of a region of steep linear increase at higher q values followed by another region of linear increase with a lower slope. As in previous SAXS analysis [121], it can be considered that the observed intensity is the sum of polymer and particle contributions.

Figure 3.7 (b) represents the scattering intensity after subtracting the contribution of the polymer for sample NC_{Cl}. The plot shows a central region of linear increase with a slope n=2.0, which is usually associated to tabular objects and not a slope n=1, expected for rod-like particles. These tabular objects could correspond to the planar arrays of acicular particles, observed in TEM images. The central linear region starts and ends at q- values corresponding to distances of 6 and 73 nm, respectively. The first distance is close to the average particle thickness determined by TEM and consequently to the height of tabular objects. The ending distance is clearly higher than particle length but it is comparable to the width of these objects (Fig 3.6).

3.3.5 Magnetic properties

Magnetic characterization including zero-field cooled (ZFC) and field cooled (FC) dc susceptibility, ac susceptibility and magnetization versus field measurements were performed in a commercial SQUID MPMS magnetometer from Quantum Design.

Figure 3.8 shows the variation of magnetization with the applied field, H, for NC_{wash} and NC_{Cl} samples. Curves from both samples show the presence of a contribution saturating at

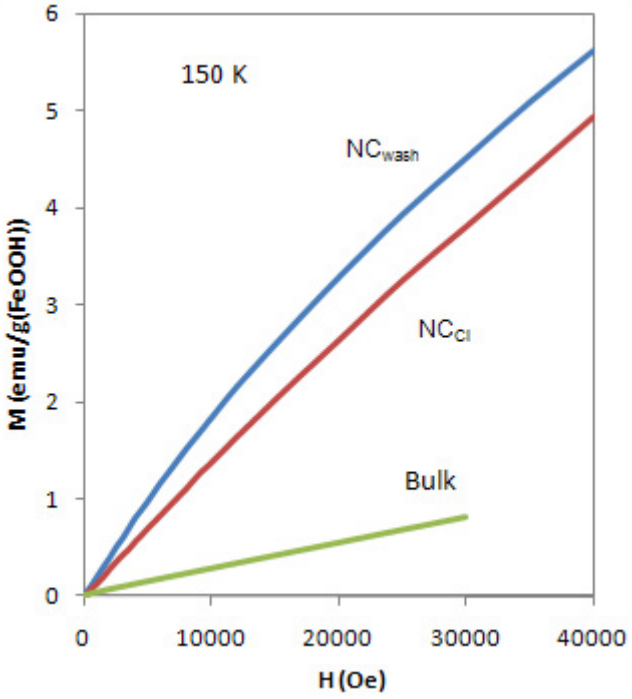

Figure 3.8: Field dependence of the magnetization of akaganéite bulk and akaganéite nanocomposite samples NC_{wash} and NC_{Cl} at 150 K.

relatively low magnetic fields plus another contribution that increases approximately linearly with H. The former contribution is larger for NC_{wash} sample than for the NC_{Cl} one. In fact, at high fields ($H \simeq 30000$ Oe) the NC_{Cl} curve is almost linear, as expected for a perfect antiferromagnet, whereas NC_{wash} still shows a slight curvature, indicating the presence of a small magnetic moment in the particles.

Figures 3.9 shows plots of the in-phase, χ' and out-of-phase, χ", ac susceptibility components, respectively, for composite and powder samples. χ" is zero over the whole temperature range for the powder. Consequently, there is not a relaxation phenomenon associated to bulk antiferromagnetic akaganéite that might become noticeable within the measuring temperature range. The sample NC_{Cl} shows a similar behavior down to 20 K. However, below 20 K and for decreasing temperatures, χ' increases steeply and χ" increases constantly from zero and both of them are frequency dependent. This suggests the appearance of a slow magnetic relaxation phenomenon due to finite size effects. In a first instance, this phenomenon could be associated with a small magnetic moment arising from uncompensated surface spins. Sample NC_{wash} shows a more complex behavior. χ' and χ" show a peak around 20 K and

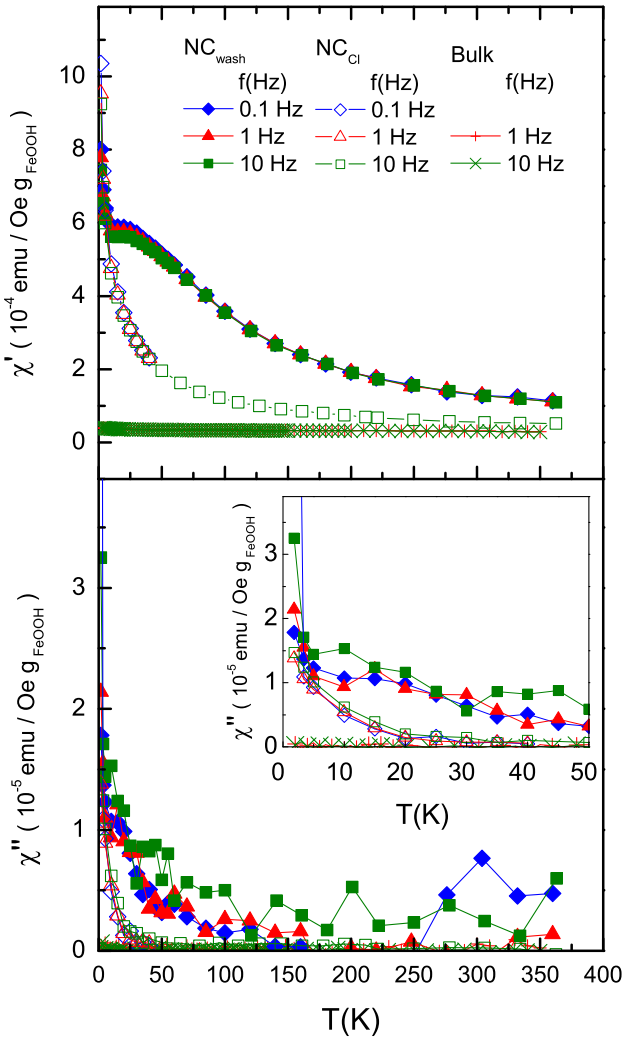

Figure 3.9: Temperature dependence of the in-phase χ' and out-of-phase χ" ac magnetic susceptibility of akaganéite powders (bulk) and nanocomposite samples NC_{wash} and NC_{Cl}.

they become frequency dependent at 70 K already. Moreover, the equilibrium magnetic susceptibility of NC_{wash} is clearly larger than the equilibrium susceptibility of NC_{Cl} (per unit of FeOOH mass). Thus, the former sample has an additional source of uncompensated magnetic moment with respect to the latter one, which is in agreement with magnetization results. The additional contribution to χ' apparently vanishes below 5 K. Indeed, below 5 K, χ' and χ" data are fairly coincident in both samples. This suggests that the additional moment in NC_{wash} blocks at a higher blocking temperature, T_B. This can be associated with a

slower relaxation process or with a higher magnetic anisotropy. Notice that, because particle sizes are similar, this additional moment and longer relaxation is not likely associated with differences in particle sizes between the two composites, but rather to a lower Cl^- content. An incomplete filling of Cl^- sites may alter the perfect compensation of antiferromagnetic sublattices and consequently it may lead to the appearance of an associated magnetic moment. In other words, Cl^- ions play a role in magnetic exchange interactions and a perfect sublattice alignment is only achieved when the crystal lattice is saturated with Cl^- ions.

The effect of Cl^- deficiency on the magnetic properties of akaganéite has been outlined before [23] in relation to a decrease of Néel temperature, T_N, although other authors attribute this decrease to the water content [123]. Reports on ac measurements of akaganéite nanoparticles describe susceptibilities χ' and χ" that increase from a certain temperature find a maximum around 10 K (T_B = 8 K, 11 K) and decrease again [110]. The measured samples were commercial iron dextran preparations containing particles with an approximate size of 20 x 4 nm. Studies based on ZFC-FC dc susceptibility measurements, yielded T_B = 18 K for spherical particles [100] and T_B = 15 K for two different rod-like particle samples with sizes 120 x 25 nm and 200 x 50 nm respectively [112] and they also showed a constant decrease of susceptibility at temperatures below T_B. Muon spin relaxation experiments (measuring time, $\tau_m = 10^{-8}$ s) yielded a blocking temperature of 10 K on akaganéite nanoparticles with an average size of 6 nm [124]. Much higher T_B values (150 - 290 K in [115] and 65 - 215 K in [116]) have been derived in Mössbauer measurements from doublet-to-sextet conversions. However, these conversions have also been interpreted as an order-disorder magnetic transition (T_N) [24], in agreement with our own measurements that indicate Néel temperatures in the range between 220 K and 250 K (see Chapter 4). Thus, studies of relaxation phenomena in akaganéite nanoparticles with a size of the same order of those studied here yield T_B values in the range 8 - 18 K that are usually related to small magnetic moments originated from uncompensated spin lattices on particle surface [125]. However, we have observed that nanoparticle samples that have not been thoroughly washed after synthesis, ensuring a full Cl^- site occupation, show relaxation effects with an associated T_B well below these values (< 2 K). On the other hand, samples undergoing a more extensive washing that may cause a structural Cl^- deficiency, at least in a part of the particle population, show an associated blocking temperature in the range of those previously reported. Since it is expected that samples used in most of previous studies were commercial and probably deeply washed with water during their preparation, the observed blocking may actually arise from a defective occupation of Cl^- crystal sites, as in our case. As a consequence, moments arising from uncompensated surface spins would have a lower blocking temperature and thus an anisotropy lower than that derived.

3.4 Conclusions

The resulting akaganéite nanocomposites contain rod-like nanoparticles grouped in parallel planar arrays. Magnetic measurements show a small magnetic moment in akaganéite nanoparticles due to size effects that is not totally blocked at temperatures above 2 K. An additional contribution to magnetic moment appears after washing the samples that could arise from a deficient Cl^- sites occupancy. Thus, our preparation method provides access to samples with intermediate content in Cl^- which enables us to ascertain the different origins of magnetic moment in nanosized akaganéite.

Chapter 4

Thermoinduced magnetic moment in akaganéite nanoparticles

In this chapter we present experimental evidences supporting the existence of thermoinduced magnetic moments in akaganéite nanoparticles. In many antiferromagnetic nanoparticle systems it has been reported an increase of the magnetic moment with temperature [126–129]. These results were presented as an evidence of the thermal population of uniform spin-precession modes by S. Mørup and C. Frandsen [61]. However the increase of the magnetic moment found in these works were questioned [39] and attributed to artifacts of the experimental method followed in the determination of the magnetic moment. One of the difficulties is the lack of knowledge of the magnetic properties in the bulk in most of the reported observations. For instance, ferrihydrite, in which the thermoinduced magnetic moment is usually reported, cannot be found in the form of a massive material. To overcome this problem we have studied the thermoinduced magnetic moment in akaganéite nanoparticles. Bulk akaganéite can be synthesized and then, bulk magnetic properties can be determined in a rather straightforward manner.

In this work, we have studied the thermoinduced effect in akaganéite nanocomposites. These composites contain isolated akaganéite nanoparticles embedded in a polymer matrix. We found that the nanoparticle magnetic moment increases with temperature above the blocking temperature, an increase that can be attributed to the thermal population of uniform spin-precession modes.

We first present the physical properties of the bulk akaganéite. We will extract information about relevant parameters such as the Néel temperature and the intrinsic antiferromagnetic susceptibility. Then, we characterize akaganéite nanocomposites. Its magnetic relevant properties are compared with those of the bulk material and we will show that some of them are size dependent. We then determine how the magnetic moment of the nanoparticles depends on temperature. Finally, we calculate the energy of spin waves modes and argue that the thermoinduced effect is indeed present in akaganéite nanoparticles.

4.1 Synthesis

We have synthesized three samples: bulk akaganéite powders, akaganéite nanocomposites and a ferrofluid made from the nanocomposite. The synthesis and characterization of the first two samples are described in Chapter 3. The nanocomposite sample corresponds to the sample defined as NC_{Cl}.

The ferrofluid was prepared to discard the existence of magnetic interactions between nanoparticles in the akaganéite nanocomposite by comparing the magnetic behavior of both samples. The nanocomposites can be readily dissolved in slightly acidic media to obtain nanoparticle dispersions. The ferrofluid was prepared by diluting 5 mg of powder nanocomposite in 1 mL of HNO_3 0.1 N. The resulting fluid was left 2 - 4 days and then it was sonicated.

4.2 Structural properties

4.2.1 XRD and FTIR

XRD and FTIR characterization of the samples is given in Chapter 3, Sec. 3.3.1 and Sec. 3.3.2, respectively. The XRD pattern and FTIR spectrum of the nanocomposite sample correspond to sample NC_{Cl}. They show that the only iron oxide phase present in nanocomposite and bulk powder samples is akaganéite.

4.2.2 Electron microscopy

Studies of electron microscopy were performed in the nanocomposite, ferrofluid and bulk powder samples. TEM images of the nanocomposite sample are shown in Chapter 3, Fig. 3.4, Fig. 3.5, Fig. 3.6. Images of various regions show isolated nanoparticles and no signs of coalescence. The analysis was carried out with Digital Micrograph software. Particle size histograms were obtained analyzing 340 particles. They are shown in Fig. 4.1. The nanoparticles are elongated with a mean length of 18±5.7 nm, a 5.4±1.5 nm diameter and an average volume of $\langle V \rangle = 298.5 \pm 204$ nm^3. From the volume distribution it is possible to estimate the mean number of particles N per gram of β-FeOOH as:

$$N = \frac{\int n(V)dV}{\int n(V)\rho V dV} = 11 \times 10^{17} \text{particles}/g_{\beta-\text{FeOOH}} \tag{4.1}$$

Using N we can also estimate the number of Fe ions in a particle to be about 6140 at Fe/particle.

A drop of the ferrofluid was evaporated on the grid to be observed by TEM. Figure 4.2 shows that the nanoparticles are of the same size as that encountered for the nanocomposite. Besides, no aggregate of nanoparticles can be observed. We can conclude that the polymer of the nanocomposite is completely and homogeneously dissolved.

For the akaganéite bulk powder, we performed SEM and TEM. SEM studies were performed with a JEOL JSM 6400 microscope with a resolution down to 3.5 nm. The sample for SEM studies was prepared embedding the grounded powder in an epoxy resin and polishing it. A typical SEM image is shown in Fig. 4.3.

The image shows the existence of elongated particles with an average volume of about 12 μm^3. TEM images (not shown) were also taken in order to discard the existence of any

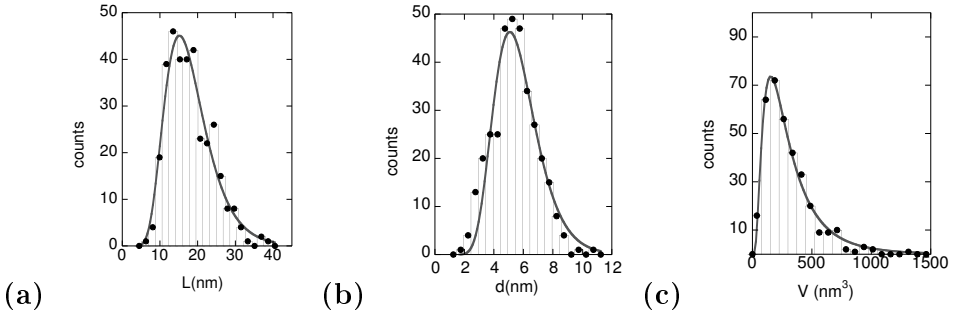

Figure 4.1: **(a)** particles length histogram and lognormal distribution fit; **(b)** particles diameter histogram and lognormal distribution fit; **(c)** particles volume histogram and lognormal distribution fit.

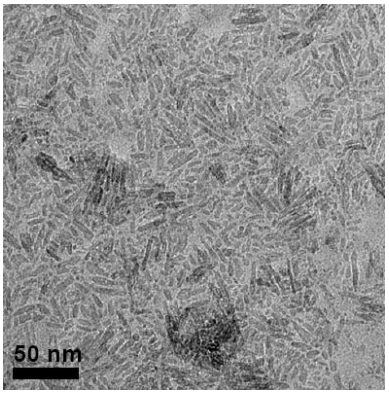

Figure 4.2: TEM image of the akaganéite ferrofluid.

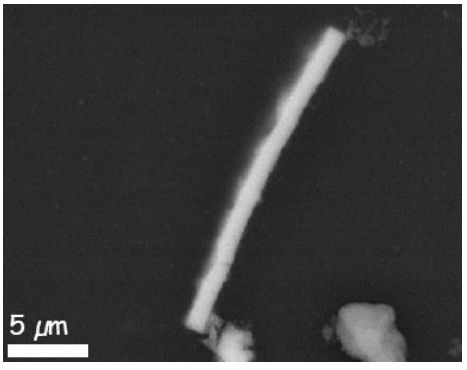

Figure 4.3: SEM image of the bulk akaganéite sample.

particle with sizes in the nanometer scale. A Cl/Fe atomic ratio of 0.21 is estimated from the EDS analysis. Using the model proposed by D. G. Chambaere and E. De Grave [24, 130] the chemical composition is $Fe(OOH)[Cl^{-}_{0.21},(OH)_{0.04}]H_{0.25}{\cdot}0.125xH_2O$, where the square brack-

ets contains the atoms located in the channels and x accounts for the number of interstitial and adsorbed water molecules that will be determined from the thermo-gravimetric analysis in the following section.

4.2.3 TGA

The weight percentage of water in the bulk sample was estimated by thermo-gravimetric analysis. The measurements were done under nitrogen atmosphere, heating from 318 K to 972 K with a scan rate of 10 °C/min. The weight loss thermogram is shown in Fig. 4.4. In a

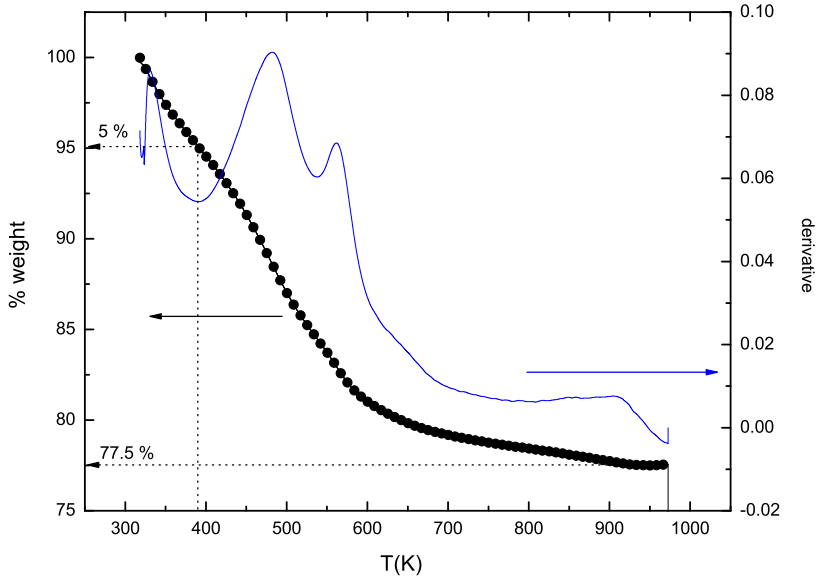

Figure 4.4: Weight Loss thermogram and its derivative. The weight loss of 5 % corresponds to water adsorbed on the surface. The residual weight is in accordance with the one expected from the stoichiometry of the phase transformation.

first step, 318-380 K approximately 5% weight is lost. This loss is usually attributed to loss of water adsorbed on the surface [96]. In the thermal decomposition of 1 mol of akaganéite to hematite 1/2 of water molecules are released. Chloride is also released from the structure in the transformation to hematite [96]. We calculate the weight loss associated to the release of Cl using the Cl/Fe atomic ratio determined from EDS analysis in the last section. Finally, looking at the stoichiometry for the akaganéite to hematite phase transformation,

$$Fe_8(OOH)_8[Cl_{1.68},(OH)_{0.32}]H_2{\cdot}xH_2O \rightarrow xH_2O + 4Fe_2O_3 + 4H_2O + 1.68HCl + 0.32H_2O$$

the amount of the weight loss of the interstitial and adsorbed water molecules xH_2O is readily calculated as ~ 5.53 %.

4.3 Intrinsic antiferromagnetic properties: size - dependent T_N and χ_{AF}

In this section we describe experiments leading to the determination of the magnetic properties of bulk akaganéite, which will be later compared with those found in the nanoparticles. In particular, we show that the Néel temperature as well as the effective spin value are similar for both bulk and nanocomposite samples. Additionally, we show that the dependence with temperature of the antiferromagnetic susceptibility, χ_{AF}, is similar for nanocomposite and bulk samples but the magnitude of χ_{AF} is larger in nanoparticles.

4.3.1 Néel temperature and exchange interaction constants

First, we have determined the Néel temperature for the bulk akaganéite sample by means of ac and dc susceptibility experiments. The magnetic measurements were performed using a commercial SQUID magnetometer (MPMS-XL, Quantum Design). Susceptibility data are plotted in Fig. 4.5 as a function of T.

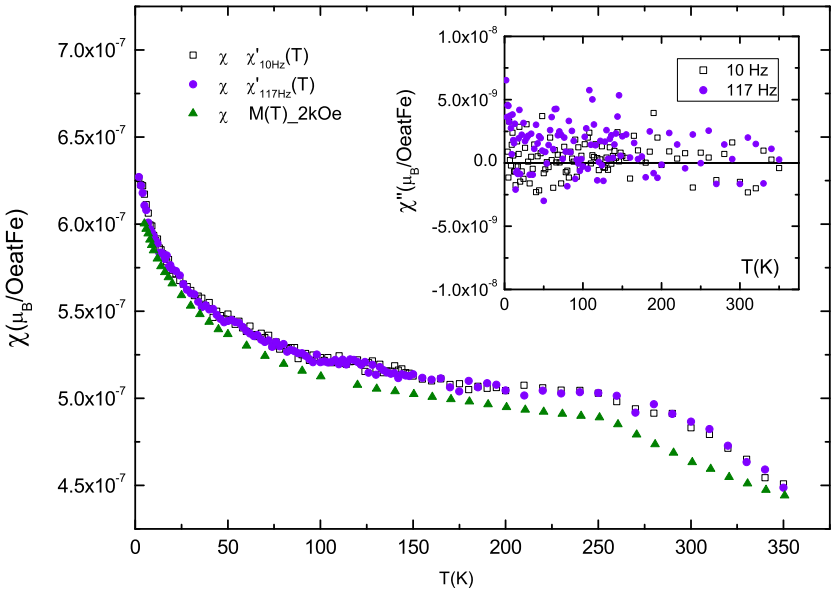

Figure 4.5: χ is obtained from: a)□, •, in phase ac susceptibility component for 10 Hz and 117 Hz, b)▲, dc magnetic measurements with an applied field of 2 kOe ($\chi = M(T)/2$ kOe). Inset: out of phase component shows bulk material does not have any nanoparticle.

At low temperatures the susceptibility does not follow the classical behavior for an antiferromagnet, as it was already shown by D. S. Kulgawczuk [131]. Moreover, the susceptibility

depends on the magnetic field, so that ac susceptibility data do not agree with dc susceptibility data. This effect may arise from a spin canting in the magnetic structure. The spin-canted structure for the akaganéite was also proposed by C. A. Barrero [23] on basis of their Mössbauer experiments.

We have plotted the reciprocal dc and in phase ac susceptibilities (10 Hz and 117 Hz) versus temperature to determine the Néel temperature. These data are shown in Fig. 4.6. The Néel temperature is determined as the temperature at which the susceptibility deviates from the Curie-Weiss behavior, $T_N = 260 \pm 1$ K.

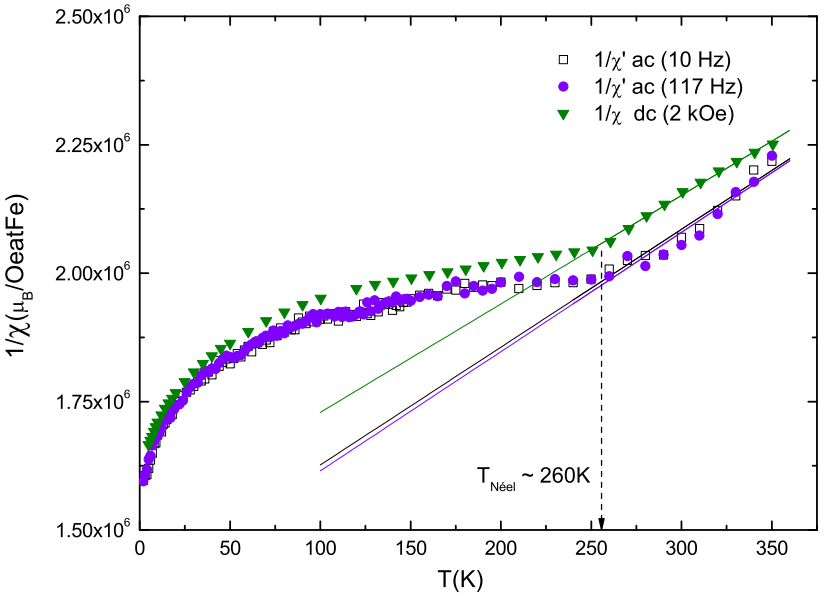

Figure 4.6: Reciprocal in-phase ac susceptibility (10 Hz, 117 Hz) and dc susceptibilities with 2 kOe. Both measurements show Néel temperature $T_N = 260$ K.

Above the Néel temperature this susceptibility follows the Curie-Weiss law,

$$\chi = \frac{N_{\text{atoms}} \mu_{\text{eff}}^2 \mu_B^2}{T - \theta} \tag{4.2}$$

where θ = -595 ± 28 K is the Weiss temperature, and $\mu_{\text{eff}} \equiv \sqrt{g^2 \mu_B^2 S(S+1)}$ = 4.4 ±0.2 μ_B is the effective magnetic moment of each Fe^{3+} ion, with a gyromagnetic ratio g and spin S. Using $g = 2$, for the Fe^{3+} with an octahedral coordination [132], this gives $S = 1.75 \pm 0.1$ for the Fe^{3+} ions.

This value of S agrees with values reported in Ref. [24]. However, S is lower than $S = 5/2$ expected from the application of Hunds's rules, as observed in other iron oxides [18]. A possible spin reduction mechanism might be associated with the compression of the coordination octahedra towards the Fe^{3+} ions by the interstitial ions in the structure. This compression would then enhance the covalency of the Fe-O bond and consequently diminish

the effective 3d-spin [24]. This mechanism was proposed by D. Chambaere and E. De Grave [24] in order to explain the reduction of the effective spin S as the number of interstitial water molecules accommodated in the structure was increased. They show that the effective spin is lower for those akaganéite structures with larger crystal water content. They propose that as the number of interstitial water molecules accommodated in the channels increases, the coordination octahedra compresses towards the Fe^{3+} ions. The effective spin $S \simeq 1.83$ reported by D. G. Chambaere for the sample with similar chlorine and water content as the sample we studied here is of the same order as the S we have determined.

The sublattice magnetization is estimated as $M_S = \frac{1}{2} N g \mu_B S = 413.6$ emu / cm^3, where $N = 2.5 \times 10^{22}$ atFe / cm^3 for akaganéite.

From the values for θ, T_N and S, we can estimate exchange constants for the akaganéite magnetic structure. We apply a mean field approximation [33] and assuming that the akaganéite magnetic structure is that shown in Fig. 1.2. Each iron Fe^{3+} interacts with six neighbors with an antiferromagnetic constant J_{AB} and with two neighbors with an exchange constant J_{AA} that can be either ferro or antiferromagnetic. If we assume that J_{AA} is antiferromagnetic,

$$\theta = -\frac{S(S+1)}{3k_B}(2J_{AA} + 6J_{AB}) = -595\text{K} \tag{4.3}$$

$$T_N = \frac{S(S+1)}{3k_B}(2J_{AA} - 6J_{AB}) = 260\text{K} \tag{4.4}$$

It follows that $J_{AB} = 44.41 \pm 3.86$ K, $J_{AA} = 52.20 \pm 2.02$ K. Although both exchange constants are antiferromagnetic, the most energetically favorable configuration for the akaganéite magnetic structure is that proposed in Fig. 1.2. We notice that the calculated intra-lattice constant (J_{AA}) is larger than the inter-lattice one. However, as we already discussed the antiferromagnetic interaction between A-A iron atoms is expected to be weaker than between A-B iron atoms. We should perhaps consider the possibility that the temperature range where the Curie-Weiss fit was performed is not sufficiently far from T_N. The temperature θ may be determined more accurately when a larger temperature range becomes available.

We have performed heat capacity (C_p) measurements to support the Néel temperature determined from the magnetic data. We have used a commercial DSC (differential scanning calorimeter) Q1000 from TA instruments. The measurements were made under helium atmosphere, heating from 312 to 450 K with a scan rate of 10 K/min. Then, the sample was removed from the apparatus. The C_p is measured again with the same heating routine. We display in Fig. 4.7 the heat capacity and its derivative for the temperature region of interest.

We notice that the heat capacity measured in the second experiment is lower than that measured in the first one, so that some desorption takes place, considering that the sample holder used in these experiments was not hermetic. The difference in C_p agrees with the weight loss found in TGA (see Fig. 4.4) within the experimental errors. The C_p is about 40 % larger than the one calculated by B. E. Lang for bare akaganéite [133]. This discrepancy can be interpreted as follows. First, the sample measured in DSC has more water than the sample used in TGA experiments. In addition, the Cl^- moles per mol of akaganéite is 9.6×10^{-3} for the sample studied by B. E. Lang while the one studied in this work is about 0.21. So that the large discrepancy between the two values of C_p can be also associated to the additional specific heat contribution arising from the Cl^- ions residing in the channels. Finally, differences due to the accuracy of the DSC measurement (typically around 5 %) may also contribute.

We now turn our attention to the determination of T_N. In Fig. 4.7 we can hardly observe

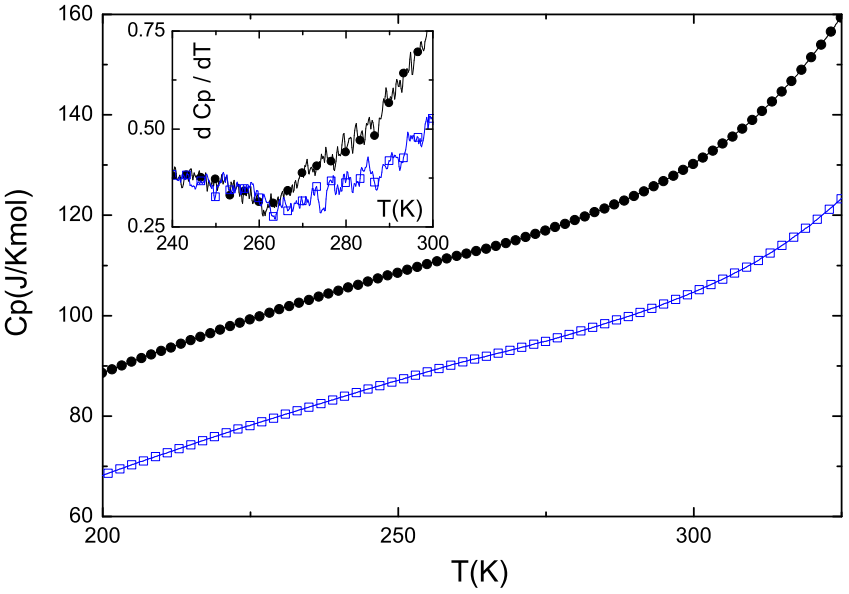

Figure 4.7: Heat capacity measurements of bulk akaganéite for the experiment 1 (•) and experiment 2 (□). Derivative of C_p is also displayed.

a small anomaly or change in the trend (close to the experimental resolution) at about ~ 260 K in which magnetic measurements reveal the antiferro to paramagnetic transition. The absence of any strong anomaly in the heat capacity over the temperature range for the antiferromagnetic transition is also observed in the measurements of B. E. Lang [133]. In this work, the absence of a sharp peak at the antiferromagnetic transition is associated to finite-size effects. This effect is reflected in the absence of long range magnetic ordering and a spread out of the magnetic transition over a wide temperature range. The anomaly shown in Fig. 4.7 is of the order of that found by B. E. Lang. The particle size of the akaganéite sample used in our experiments (see Fig. 4.3) is an order of magnitude larger than that of B. E. Lang. But it seems that this increase is still not enough in order to give a clear sharp anomaly. We can therefore tentatively associate the small anomaly found in ~ 260 K to the antiferromagnetic transition considering its agreement with the T_N value determined from magnetic measurements.

4.3.2 Néel temperature of nanoparticles

Heat capacity was also used to determine the Néel temperature of the akaganéite nanoparticles. The measurements were done under helium atmosphere heating from 193 K to 453 K with a scan rate of 10 K/min. In Fig. 4.8 we appreciate only a small anomaly (near the experimental resolution) at around 260 K. The absence of a sharp peak at the antiferromagnetic transition can be ascribed to finite-size effects. Considering this anomaly as the evidence of the magnetic ordering and its agreement with the magnetic value for the bulk

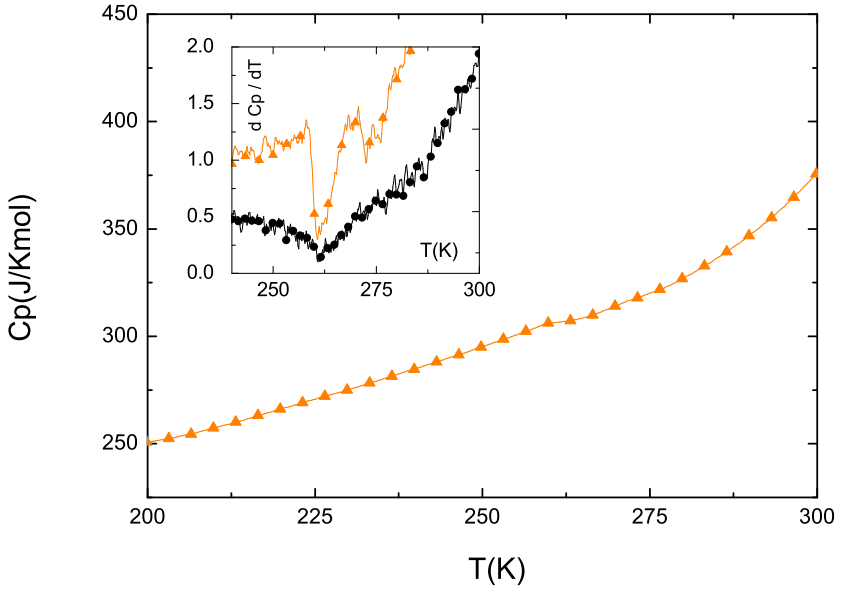

Figure 4.8: Heat capacity measurements for akaganéite nanocomposites displays an anomaly at $T \sim 260$ K. Inset: Derivative of C_p for the bulk (•) and nanoparticles (▲) have a minimum at $T \sim 260$ K.

akaganéite sample, we can conclude that the Néel temperature does not show any significant variation when the size changes by two orders of magnitude.

We should also mention that the spread in the values of T_N reported in the literature has been usually attributed to variations in the content of the ions inside the channels of the akaganéite structure [23, 24]. We have already mentioned that the magnetic properties of akaganéite have been shown to strongly depend on the chlorine content [31].

Now, we determine the effective spin of Fe^{3+} for the akaganéite nanoparticles. The reciprocal paramagnetic susceptibilities, in units of μ_B/Oe atFe, of the bulk and nanocomposite samples show nearly the same slope for temperatures $T > T_N$, as displayed in Fig. 4.9. Above the Néel temperature T_N, the susceptibility follows the Curie-Weiss law giving θ = -49 ± 13 K and μ_{eff} = 3.41 ±0.08 μ_B. Using a gyromagnetic ratio $g = 2$ this gives $S = 1.28 \pm 0.04$ for the Fe^{3+} ions. This slight discrepancy in the value of the effective atomic spin can be associated to the lower coordination of the Fe ions in the nanoparticles surface. By contrast, θ is 12 times smaller for the nanoparticles as compared with the bulk.

We can finally conclude that the Néel temperature does not present any significant variation with size. By contrast, θ is smaller for the nanoparticles as compared to the bulk.

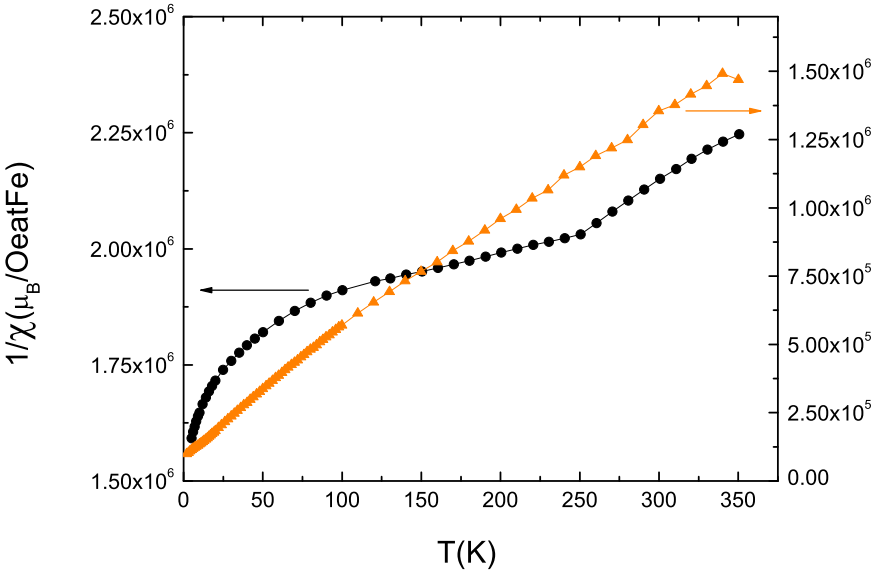

Figure 4.9: Reciprocal equilibrium susceptibility shows similar effective spin for the nanocomposite (▲) and (•) the bulk samples.

4.3.3 Antiferromagnetic susceptibility χ_{AF}

As explained in Sec. 1.2.6, an external magnetic field applied perpendicular to the easy axis of an antiferromagnetic material produces a small net magnetization that is proportional to the magnitude of the applied magnetic field. The slope is $\chi_\perp$. For randomly oriented powders, this linear contribution is $\chi_{AF} = (2/3)\,\chi_\perp$ at $T = 0$. This linear component can be determined in a bulk antiferromagnetic material from susceptibility measurements (ac or dc) and from the extrapolation to high fields of magnetization curves.

We first determine χ_{AF} from extrapolation to high field of the magnetization measured in the SQUID magnetometer setup. The curves are shown in Fig. 4.10. The magnetization is approximately linear with the applied field, as expected for an antiferromagnetic material. The linear antiferromagnetic component is determined from a linear fit of the high field region at each temperature.

We also measured magnetization isotherms in the High Field Magnet Laboratory (HFML). After subtraction of the diamagnetic contributions, the resulting magnetization curves do not fully superimpose with the ones obtained in the SQUID. Nevertheless, they have the same variation with temperature. The discrepancies observed can be accounted to differences in the calibration factor and in the diamagnetic contribution from the sample holder. Magnetization curves were scaled with respect to those obtained in previous section. In the scaling procedure we search for the calibration factor and diamagnetic contribution such that derivatives versus temperature of experimental data from both setups superimpose. The scaling factors determined in this section will be further used in the following sections to scale magnetization curves measured for akaganéite nanoparticles.

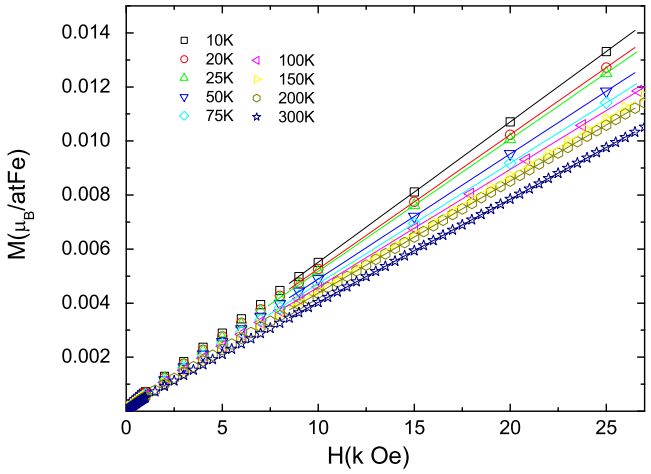

Figure 4.10: Magnetization isotherms for bulk akaganéite. The solid lines are linear fits at high fields.

The magnetization curves are shown in Fig. 4.11 together with those measured in the SQUID setup. The antiferromagnetic susceptibility is determined for the high-field

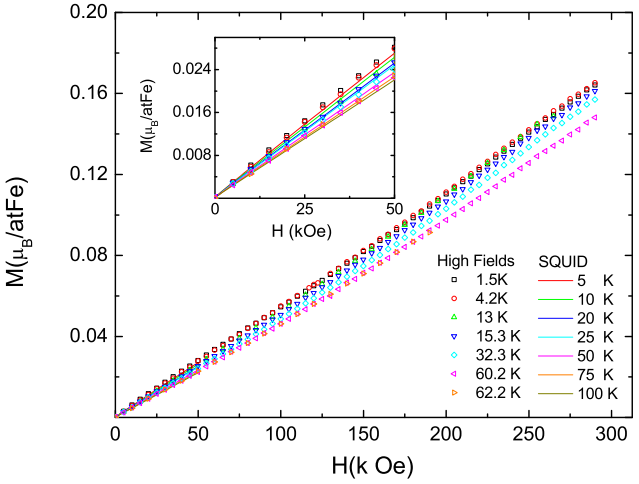

Figure 4.11: Magnetization isotherms for bulk akaganéite; Inset: low field region magnification.

measurements with a linear fit at an intermediate field region of ~ 5 T. It is shown in Fig. 4.12 together with the ones we obtained from ac susceptibility and dc susceptibility data.

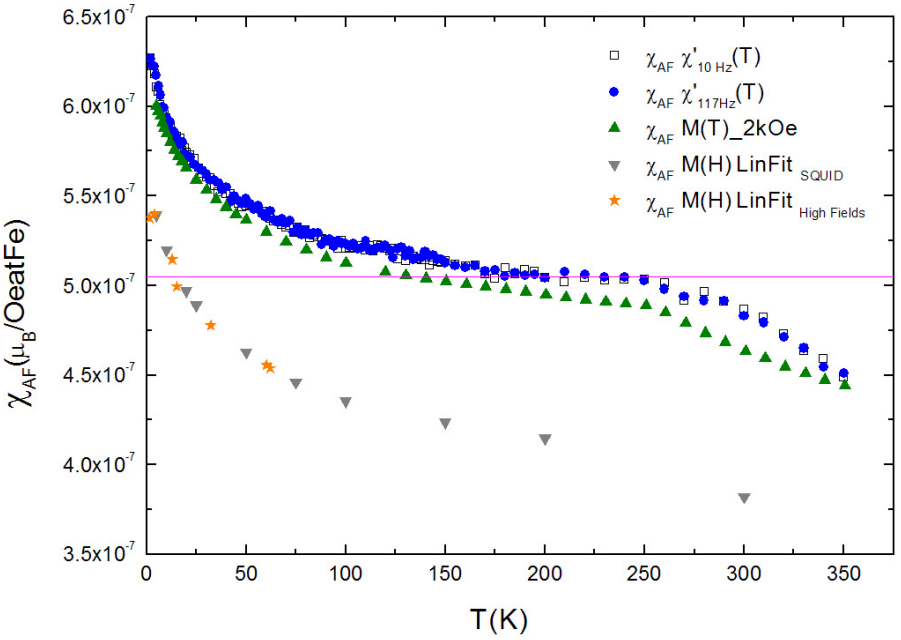

Figure 4.12: Antiferromagnetic susceptibility obtained through four different techniques: a) in phase component of ac susceptibility (□ 10 Hz, • 117 Hz) , b) ▲ dc susceptibility measurements at 2 kOe ($\chi_{AF} = M(T)/2$ kOe), c) linear fit of magnetization curves ▼, d)★ linear fit of high field magnetization curves. The solid line is the calculated value using a mean field approximation.

We notice that the temperature dependence of χ_{AF} determined from high-field data is the same as that obtained from the SQUID device. However, χ_{AF} determined from magnetization isotherms is smaller than that obtained from susceptibility measurements. This effect may arise from a slight spin canting in the magnetic structure found for akaganéite. This contribution will be studied in detail in the next section.

Thermal dependence of χ_{AF} at high fields is interpolated scaling the χ_{AF} determined from dc susceptibility measurements at 2 kOe to the antiferromagnetic susceptibility determined from magnetization data at high fields. Similarly, the χ_{AF} at low fields is interpolated scaling the dc susceptibility to the ac susceptibility.

We have also calculated χ_{AF} at T_N using a mean field approximation [33]. At $T = 0$ both sublattices lie in the easy sublattice axis antiparallel to each other. A magnetic field applied perpendicular to the easy axis produces a tilting of sublattice magnetization opposite to that arising from the exchange interaction. At equilibrium, we have

$$|\vec{M}_A \times (\vec{H} - \vec{H}_E)| = 0 \tag{4.5}$$

where $H_E = H_{E(AA)} + H_{E(AB)} = \gamma_{AA} M_A + \gamma_{AB} M_B$ is the exchange interaction field for an Fe^{3+} atom from sublattice A. Using the equilibrium equation we get $\chi_\perp = 1/\gamma_{AB}$. The

molecular field constant $\gamma_{AB} = n_{AB} J_{AB} / \left[N/2(g\mu_B)^2\right]$ is calculated using exchange constants determined from T_N and θ values. N is the number of iron atoms per unit volume and $n_{AB} = 6$ for the magnetic structure shown in Fig. 1.2. At $T = T_N$ the antiferromagnetic susceptibility $\chi_{AF} = \chi_\perp = 5.05 \times 10^{-7}$ μ_B/Oe atFe coincides with that measured for bulk akaganéite.

4.3.4 Antiferromagnetic susceptibility of nanoparticles

In antiferromagnetic nanoparticles, the magnetization curves measured above T_B do not seem to saturate and, at high fields, they increase almost linearly with the applied field. L. Néel [58] proposed that this behavior can be modeled with the antiferromagnetic susceptibility $\chi_{AF} H$ plus an additional magnetization due to uncompensated moments. In addition, the antiferromagnetic susceptibility χ_{AF} of antiferromagnetic nanoparticles is usually larger than what it is found in bulk for temperatures below T_N. This effect was also explained by L. Néel [57]. He proposed that an additional susceptibility χ_{SAF} arises from the continuous rotation of the antiferromagnetic ordering axis within the nanoparticle, when a magnetic field is applied perpendicular to it. He called this contribution 'superantiferromagnetism'. He also estimated that χ_{SAF} decreases with temperature [60]. In order to extract the temperature dependence of the magnetic moment from magnetization measurements we should first determine χ_{AF} for the nanoparticles. This work will be described in the present section and the results compared with those obtained for the bulk.

Magnetization isotherms of the nanocomposite sample are shown in Fig. 4.13. They

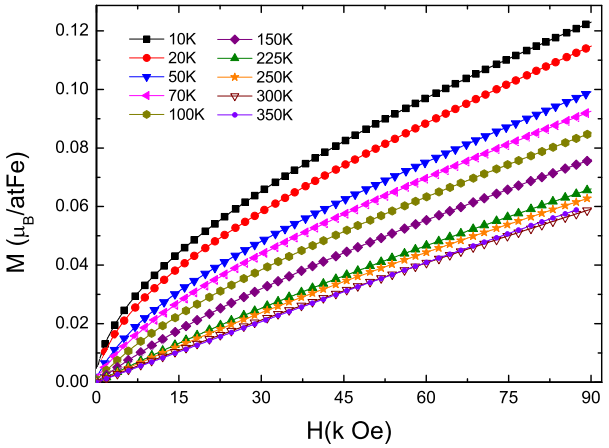

Figure 4.13: Magnetization isotherms for akaganéite nanoparticles.

display the two contributions just mentioned. The contribution from uncompensated spins becomes noticeable at low fields. At higher fields, the magnetization approaches a linear behavior. The latter region emerges at lower fields as we increase temperature. At temperatures higher than the Néel temperature, the magnetization curve is just proportional to the applied field.

We also measured magnetization isotherms in the High Field Magnet Laboratory (HFML). The curves were scaled after subtraction of the diamagnetic contributions. We apply the same scaling constants that were determined in Sec. 4.3.3 for the bulk material. Some magnetization curves are shown in Fig. 4.14. Again, the two contributions to the magnetization can be seen.

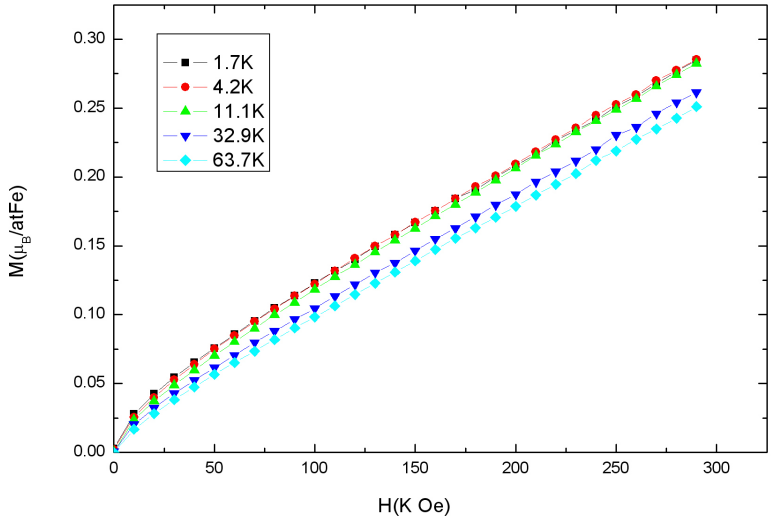

Figure 4.14: Magnetization isotherms for akaganéite nanoparticles from high field measurement laboratory.

However, we notice that the contribution arising from the uncompensated moments seems to be smaller in the data measured at HFML than in the data measured in the VSM magnetometer. In Fig. 4.15 we compare magnetization curves measured at two temperatures in the VSM, SQUID and high field magnetometers.

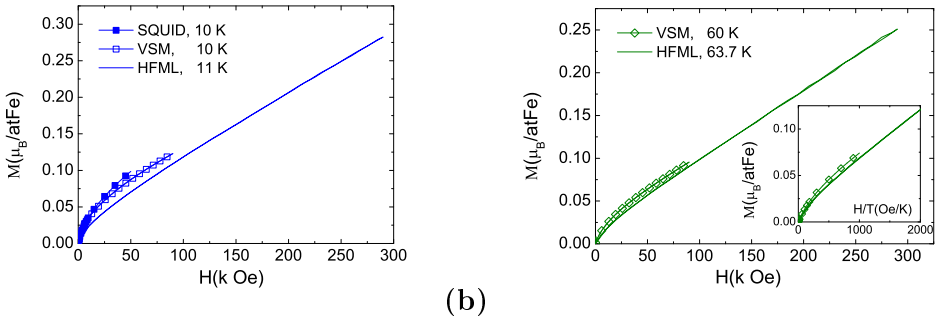

(a) (b)

Figure 4.15: Magnetization curves obtained from three setups **(a)** at 10 K and **(b)** at 60 K. Inset shows magnetization versus H/T at superparamagnetic regime

The differences between these sets of data are much more noticeable at 10 K, that

is, below the blocking temperature. For larger temperatures, these differences gradually decrease, actually vanishing in the superparamagnetic regime. We conclude that differences between the magnetization curves obtained with the different magnetometers arise from their different sweep rates of the applied magnetic field. In the superparamagnetic regime there is no magnetic relaxation and magnetization curves fully superimpose. This explains also why we have determined the scaling factors for the data measured with the HFML from data measured of the bulk samples which shows no relaxation at any temperature.

Next, we shall determine the antiferromagnetic susceptibility for the nanoparticles. Different methods to obtain $\chi_{\mathrm{AF}}(T)$ have been proposed. As a first approximation, the magnetization curves of antiferromagnetic nanoparticles can be modeled by [126],

$$M = M_{\mathrm{S}} L\left(\mu \frac{H}{k_{\mathrm{B}} T}\right) + \chi_{\mathrm{AF}} H \tag{4.6}$$

where M_{S} is the saturation magnetization, μ is the uncompensated magnetic moment, $L\left(\mu \frac{H}{k_{\mathrm{B}} T}\right)$ is the Langevin function (see section Sec. 1.2.3) and χ_{AF} is the linear antiferromagnetic susceptibility. However, N. J. O. Silva et al [39] showed that a direct fitting of magnetization isotherms with this expression can give parameters with an erroneous temperature dependence. They propose an alternative approach to determine the linear magnetization component. In what follows, we apply such method to estimate χ_{AF} for akaganéite nanoparticles.

When the antiferromagnetic nanoparticles follow Eq. (4.6), the derivative of the magnetization with respect to the applied field $\partial M/\partial H$ is

$$\frac{\partial M}{\partial H} T = F\left(\frac{H}{T}\right) + \chi_{\mathrm{AF}} T \tag{4.7}$$

where F is an unknown function of (H/T). If the magnetic moment does not depend of the temperature and if the anisotropy can be considered negligible, for any two temperatures T_1 and T_2,

$$\frac{\partial M}{\partial H} T_1 = F\left(\frac{H}{T_1}\right) + \chi_{AF_{T_1}} T_1 \tag{4.8}$$

$$\frac{\partial M}{\partial H} T_2 = F\left(\frac{H}{T_2}\right) + \chi_{AF_{T_2}} T_2 \tag{4.9}$$

$$\frac{\partial M}{\partial H} T_2 - \frac{\partial M}{\partial H} T_1 = F\left(\frac{H}{T_2}\right) + \chi_{AF_{T_2}} T_2 - F\left(\frac{H}{T_1}\right) - \chi_{AF_{T_1}} T_1 \tag{4.10}$$

The last term being equal to

$$\chi_{AF_{T_2}} T_2 - \chi_{AF_{T_1}} T_1$$

only if

$$F\left(\frac{H}{T_2}\right) - F\left(\frac{H}{T_1}\right) = 0$$

The temperature dependence of the linear component $\chi_{\mathrm{AF}}(T)$ is estimated using the lowest isotherm measured at T_1 as a reference. In our particular case, we take as a reference the magnetization curve measured at $T = 1.7$ K in the HFML. We plot $(\partial M/\partial H)_T * T - (\partial M/\partial H)_{1.7K} * 1.7$ data obtained at different temperatures in Fig.4.16. We now determine $(\partial M/\partial H)_{1.7K}$ from saturation value for $(\partial M/\partial H)$ as follows. We plot $(\partial M/\partial H)$ versus $1/(H/T)$ and extrapolate $1/(H/T) \to 0$. With χ_{AF} for the isotherm of 1.7 K known we can determine from $(\partial M/\partial H)_T * T - (\partial M/\partial H)_{1.7K} * 1.7$ the thermal dependence of $\chi_{\mathrm{AF}}(T)$. We also determined the antiferromagnetic susceptibility from plain linear fits of magnetization isotherms and the results are shown in Fig. 4.17. The antiferromagnetic susceptibility extracted from data measured at very high fields agrees well with that obtained from the VSM. Besides, we notice that $\chi_{\mathrm{AF}}(T)$ determined from the linear fit of VSM magnetization

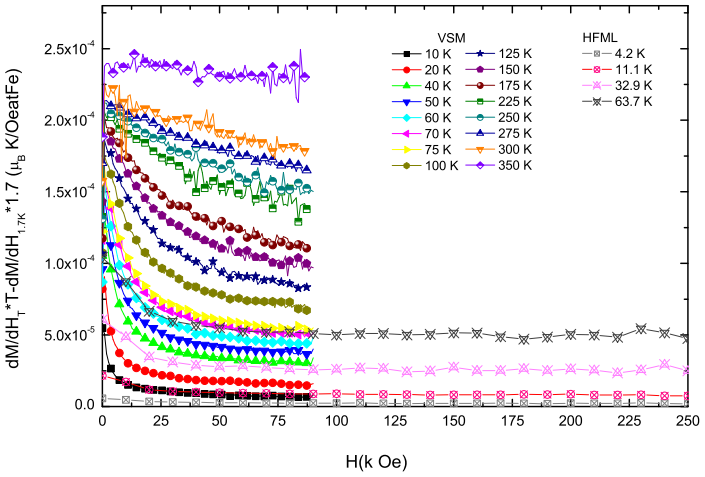

Figure 4.16: $(\partial M/\partial H)_T * T - (\partial M/\partial H)_{1.7K} * 1.7$

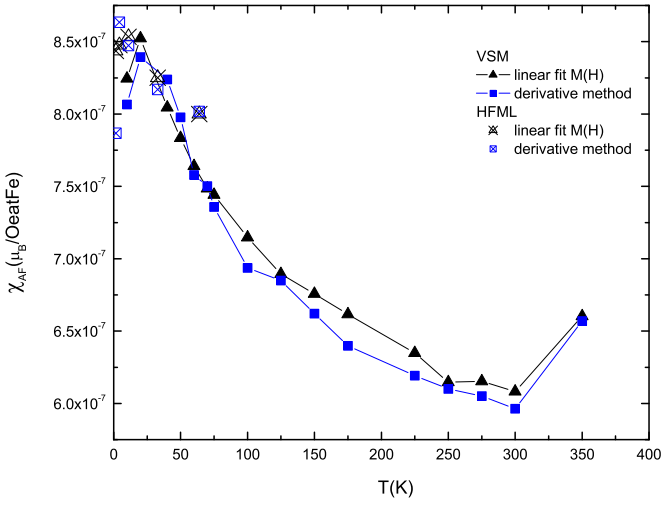

Figure 4.17: $\chi_{\mathrm{AF}}(T)$ akaganéite nanoparticles determined with the method proposed in Ref. [39] and from a linear fit of magnetization isotherms measured with the VSM (full symbols) and the high-field magnetometer (crosses).

isotherms is comparable with that obtained from the method proposed by N. J. O. Silva et al [39]. Therefore, this shows that the uncompensated magnetic moments are virtually

saturated at fields of order of 9 T. The linear antiferromagnetic susceptibility is then the main contribution to the magnetization.

We compare the linear susceptibility component obtained for bulk and for the nanoparticles in Fig. 4.18. They show a similar dependence with temperature although χ_{AF} is 1.5

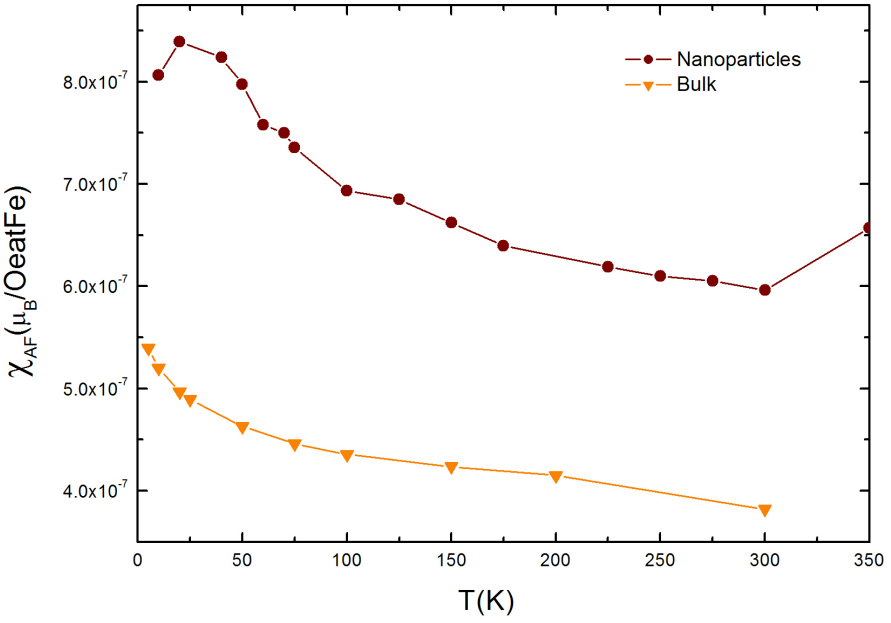

Figure 4.18: $\chi_{\mathrm{AF}}(T)$ of akaganéite nanoparticles determined with the method of Ref. [39] and $\chi_{\mathrm{AF}}(T)$ of bulk akaganéite.

times larger for the nanoparticles. This decrease can be justified as follows. At first sight it might seem that the model proposed by N. J. O. Silva et al may not be applicable to this system, because the anisotropy can not be assumed negligible. However, this argument should be disregarded because there is an excellent agreement between the χ_{AF} calculated from this model and that determined from the linear fits. We conclude that the enlargement observed in χ_{AF} can be associated to the effect of superantiferromagnetism [57].

4.3.5 Anisotropy constant: Spin-flop transition

In this section, we determine the anisotropy constant of akaganéite from HFML measurements.

Typical magnetization curves measured at high fields were shown in Fig. 4.10. At the lowest temperature of $T = 1.5$ K, the magnetization curve shows a small change of slope at $\sim$ 24 T. The derivative of the magnetization shows indeed a peak near this field, as displayed in Fig. 4.19. This feature can be attributed to a spin-flop transition. Some antiferromagnetic materials can exhibit a spin-flop transition to a state where the moments lie almost perpendicular to the applied field when a sufficiently large field H_{sf} is applied

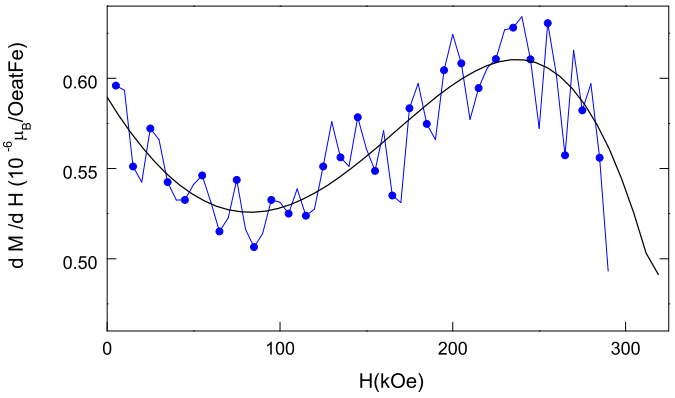

Figure 4.19: The derivative of the high field magnetization vs field, showing evidence for a spin-flop transition at 1.5 K. The solid line represents the derivative of the interpolated magnetization data.

parallel to the easy magnetization axis. The expression for H_{sf} is [33],

$$H_{sf} = \sqrt{\frac{2K}{\chi_{\perp} - \chi_{//}}} \tag{4.11}$$

where K is the anisotropy constant. The spin-flop transition is sensitive to the crystal orientation with its easy axis of antiferromagnetic alignment parallel to the direction of the applied field. However, when the field is applied at a small angle ψ with respect to the direction of the easy axis, the spin-flop transition takes place at

$$H = \frac{1}{\cos(\psi)} \sqrt{\frac{2K}{\chi_{\perp} - \chi_{//}}} \tag{4.12}$$

The maximum angle with respect to the easy axis under which a SF transition can be observed [134] is $\psi_{max} = H_{AN}/2H_E$, where $H_{AN} = K/M_S$ is the anisotropy field for an antiferromagnet. In a sample with a random orientation of the easy axis Eq. (4.12) is averaged up to this critical angle. For our sample, this angle ~ 0.08 ° is very small, so that only those particles with the easy axis oriented close to the direction of the applied field contribute to the average and

$$\langle H \rangle \simeq \sqrt{\frac{2K}{\chi_{\perp} - \chi_{//}}} \tag{4.13}$$

This is in accordance with the small anomaly shown in the magnetization curve at the transition.

At low enough temperatures, $T \sim 0$, the parallel component of the susceptibility is $\chi_{//} \simeq 0$ and then

$$H_{sf} \simeq \sqrt{\frac{2K}{\chi_{\perp}}} \tag{4.14}$$

A direct method of calculating $\chi_{\perp}$ is to extrapolate $\partial M/\partial H$ at high fields and use the condition $\chi_{\perp} = \frac{3}{2}\chi_{AF} = \frac{3}{2}(\partial M/\partial H)$. At fields $H \sim 5$ T, $\chi_{\perp} = \frac{3}{2}\partial M/\partial H = 5.1 \times 10^{-5}$ emu/Oe

$g_{\beta-\mathrm{FeOOH}}$, giving K =5.5 × 10 ^{6} erg/cm^3. This value is of the order of that expected for the iron atom that can be in a first approach calculated from [33]

$$K_1 = J_e(g-2)^4 \sim 10^6 \mathrm{erg/cm}^3$$

where J_e is the exchange integral for the iron atom and (g-2) is a measure of the orbital momentum which is present because of incomplete quenching.

Alternatively, we could also have calculated the perpendicular component of the susceptibility $\chi_\perp$ with

$$\chi_\perp = \frac{1}{\gamma_{AB} + K/2M_S^2} \simeq \frac{M_S}{H_E + H_{AN}/2} \tag{4.15}$$

neglecting other than nearest neighbors interactions. The molecular field constant γ_{AB} can be determined from the Néel temperature and θ using mean-field calculation (see section Sec. 4.3.3). However, since the mean field calculation overestimates T_N and since it is actually the transverse susceptibility which actually enters in the spin-flop process we prefer to estimate the anisotropy constant from the experimental $\chi_\perp$.

We mentioned in previous sections that the magnetic structure of akaganéite can be slightly canted. The uncompensated magnetic moment arising from the canting makes the spin-flop to take place at higher fields than for the perfect antiferromagnetic alignment [135]. We calculated the anisotropy constant with the expression provided in Ref. [135]

$$H_{sf} = mH_E + \sqrt{(mH_E)^2 + 2H_E H_{AN}} \tag{4.16}$$

and the uncompensated magnetic moment $m = M_{unc}/M_S \sim 2 \times 10^{-4}$ determined in the following section. We obtain then K=5.6 × 10^6 erg/cm^3 which agrees remarkably well with the value obtained for the perfect antiferromagnetic structure. The calculation of spin-flop transition in an uncompensated antiferromagnet was performed by J. M. D. Coey et al [135] in natural goethite. They found that an uncompensated moment of 4 × 10^{-3} μ_B more than doubles the threshold field for spin-flop transition, which is one order of magnitude larger than the uncompensated magnetic moment for akaganéite. So that we can conclude that although the magnetic structure is slightly canted for akaganéite, the influence on the magnetic anisotropy constant can be considered negligible.

The anisotropy constant can be compared with K=2.1 × 10^4 erg/cm^3, reported by J. Takagi et al [136] for akaganéite nanoparticles. This value was estimated using the relaxation rates determined from the analysis of Mössbauer spectra, in the range from 210 to 260 K. However, at these temperatures, close to T_N, the magnetic anisotropy can be significantly reduced by thermal fluctuations. The anisotropy constant strongly decreases with temperature and therefore, K should be obtained at temperatures $T \sim 0$. For the iron atom [137–139],

$$\frac{K_1(T)}{K_1(0)} = \left[\frac{M(T)}{M(0)}\right]^{10} \tag{4.17}$$

The anisotropy constant at temperatures $T \sim 240$ K, in which the superparamagnetic relaxation was analyzed by J. Takagi is two orders of magnitude lower than $K_1(0)$. Also, rotation modes other than the coherent rotation of the magnetic moment can contribute, or even become dominant in elongated nanoparticles. Then, one can still write the activation energy U for the thermally activated relaxation as $U = K\,V_{eff}$, but V_{eff} can be much smaller than the actual particle volume. This effect is enhanced in elongated nanoparticles where the domain can be nucleated at the edges, as it has been observed in nanowires [140]. The lack of proportionality between the anisotropy energy and the volume in antiferromagnetic nanoparticles has recently been reported by N. J. O. Silva et al [141].

For these reasons, we use here the anisotropy value $K \simeq 5.5{\times}10^6$ erg/cm^3 estimated above, to interpret the low temperature susceptibility of the akaganéite nanoparticles.

4.3.6 Effect of spin-canting

Derivatives of magnetization isotherms measured on bulk akaganéite samples are shown in Fig. 4.20. We notice that up to a critical field $\partial M/\partial H$ depends on field. Besides, this critical field is the same ~1.3 T for all the temperatures. This fact suggests that the observed features originate from an uncompensated magnetization arising from spin canting.

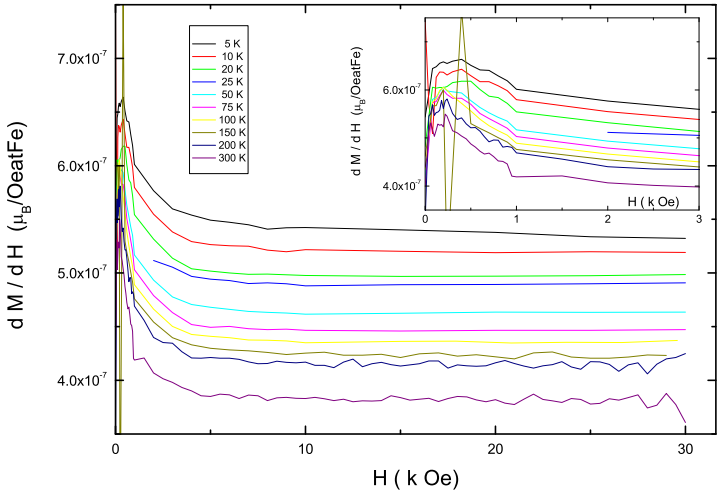

Figure 4.20: Derivatives of magnetization isotherms for bulk akaganéite; Inset: low field region magnification.

Previous works on akaganéite have proposed that there are different sites for the iron atoms located in the channels of the akaganéite structure [23, 24]: those near to the ion occupying the channel and those near a vacant site. In particular, A. Barrero [23] proposed that this feature can produce a spin-canted structure for the akaganéite.

In order to quantify the uncompensated magnetization arising from the spin canting we determined remanence extrapolating the magnetization curves shown in Fig. 4.10 to zero field. The remanence curve is shown in Fig. 4.21. The remanent magnetization at $T \sim 0$ K is $M_r \sim 3.5 \times 10^{-4} \mu_B$/atFe. We obtained the effective magnetic moment $\mu_{eff} = 4.4$ for the Fe^{3+} in Sec. 4.3.1, so that the sublattice magnetization is canted an angle 0.002 °.

Finally, we calculate the contribution of the canting to the magnetic moment of the nanoparticle. For an average particle size of $\langle V \rangle = 298.5$ nm^3 there are 6140 atFe/particle. The average magnetic moment arising from canting in the structure is therefore $\mu_{sc} \sim 2\ \mu_B$ per particle.

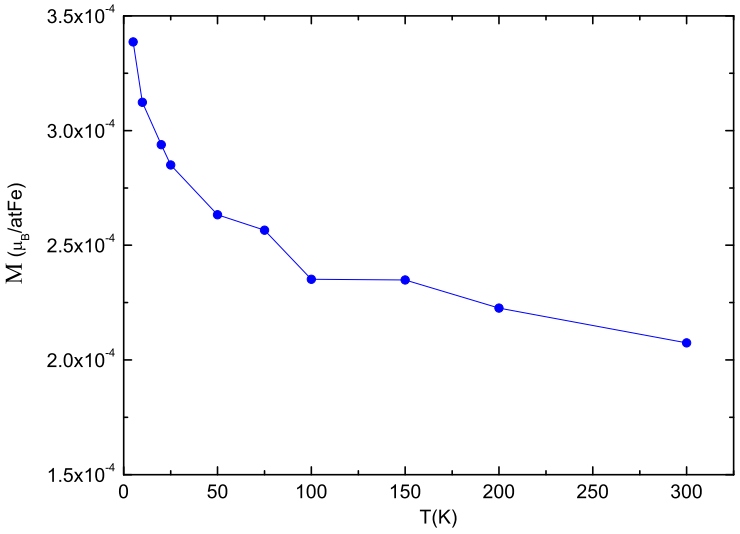

Figure 4.21: Remanence nearly disappears at $T \sim 125$ K.

4.4 Akaganéite nanoparticles: a model for the study of spin waves

4.4.1 Magnetization isotherms

In a first approach, magnetization curves for antiferromagnetic nanoparticles can be described by [126],

$$M = M_S L\left(\mu \frac{H}{k_B T}\right) + \chi_{AF} H \equiv M_\mu + \chi_{AF} H \tag{4.18}$$

where M_μ is the contribution from uncompensated magnetic moments in the antiferromagnetic nanoparticle and χ_{AF} is the linear antiferromagnetic susceptibility. The term $L\left(\mu \frac{H}{k_B T}\right)$ is the Langevin function we introduced in Sec. 1.2.3, where μ is the uncompensated magnetic moment.

To study the intrinsic magnetic behavior of nanoparticles is necessary to subtract from the magnetization curves $\chi_{AF}(T) * H$ as determined from bulk akaganéite. The results are shown in Fig. 4.22. In the superparamagnetic regime M_μ data should collapse into a single curve when plotted as a function of H/T, provided that the magnetic moment μ is temperature independent. Actually, as Fig. 4.22 shows, the magnetic moment depends with the temperature, increasing first with temperature for $T < 60$ K and then decreasing for $T > 75$ K (see the inset).

Magnetization curves were fitted using Eq. (4.18), allowing a temperature dependence of the magnetic moment with temperature. The fitting curves do not fully superimpose with the experimental data, probably because the influence of anisotropy is very strong. In addition, the magnitude of the antiferromagnetic susceptibility determined from the fit approaches the χ_{AF} of the bulk as $T \to T_N$. Actually, the $\partial M/\partial H_T * T - \partial M/\partial H_{1.7} * 1.7$

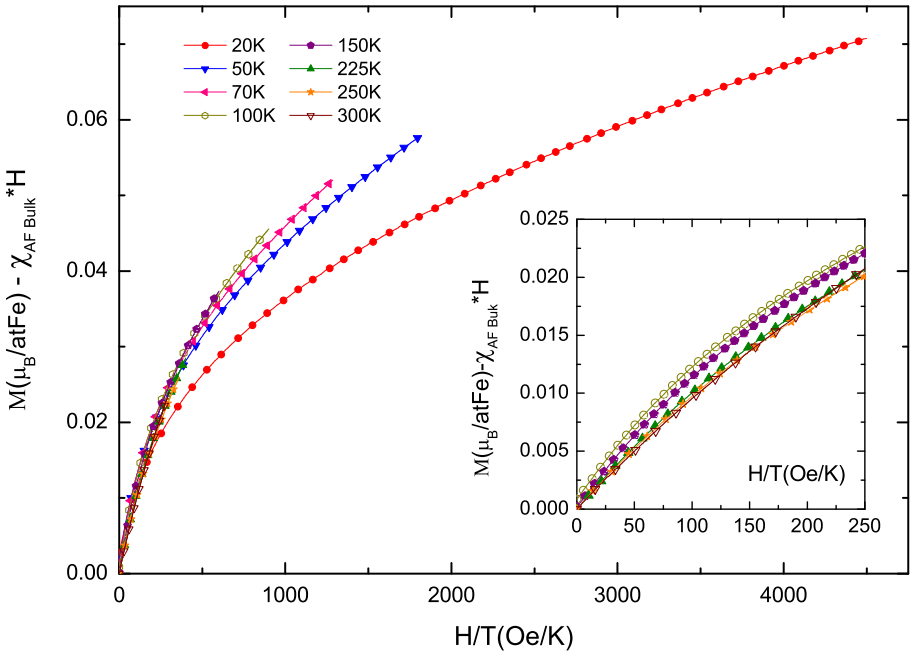

Figure 4.22: Superparamagnetic contribution for nanoparticles obtained subtracting $\chi_{\mathrm{AF}}(T) * H$. The lines are included as eye guide. Inset: high temperature detail.

curves shown in Fig. 4.16 are not fully saturated for temperatures $T > 125$ K. The difference between the antiferromagnetic susceptibilities in Fig. 4.18 for the temperature range $T \sim 125$ K - 260 K can be therefore considered an artifact in the derivation of χ_{AF}. For temperatures above 125 K, the magnetization arising from the uncompensated spins is not yet completely saturated, meaning that χ_{AF} cannot be properly determined under these conditions.

We conclude that we can obtain qualitative information from the magnetization curves. However, the derivation of quantitative information is hindered by the influence of anisotropy and therefore, it is better to extract the magnetic moment from a magnitude where the influence of anisotropy can be neglected, such as the equilibrium susceptibility.

4.4.2 In phase component of ac susceptibility

Below T_{N}, χ' becomes much larger than the AF susceptibility χ_{AF} measured on the bulk sample (see Fig. 4.23). This reveals the existence of uncompensated spins, as already pointed out by Néel on his seminal papers [57–60]. The susceptibility of a set of AF nanoparticles can then be approximated by the following expression [41, 64]

$$\chi' = \chi_{\mathrm{AF}} + \chi_{\mathrm{unc}} + \chi_{\mathrm{th}} \tag{4.19}$$

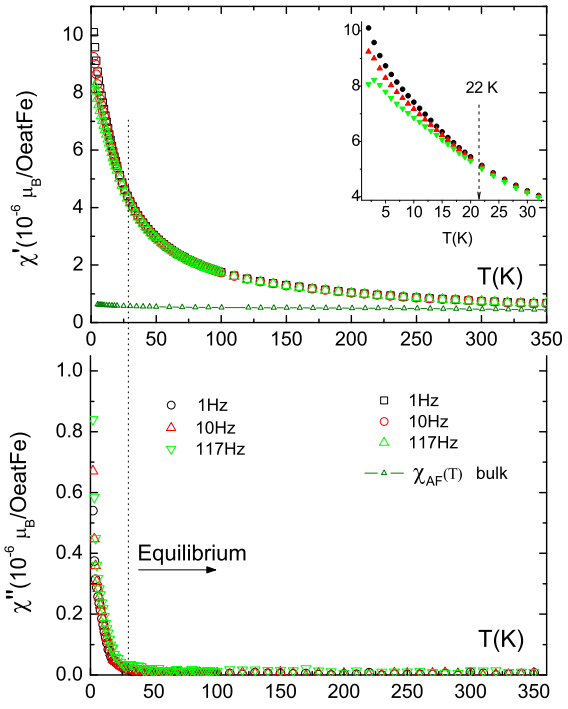

Figure 4.23: In-phase and out-of-phase components of ac susceptibility measured at different frequencies shows that superparamagnetic regime begins at 22 K.

where χ_{unc} and χ_{th} are the contributions due to the uncompensated and thermoinduced magnetic moments respectively. χ_{unc} can be expected to show the superparamagnetic blocking, associated with relaxation. Surprisingly, considering the values of the estimated magnetic anisotropy constant and particle volume, the susceptibility does not show the typical superparamagnetic blocking, as shown in Fig. 4.23. This confirms that rotation modes other than the coherent rotation are contributing to the magnetic relaxation, as discussed previously. This may also account for the lack of proportionality between the energy barrier and the particle volume found by N. J. O. Silva et al. [141] and for the small value of K, compared to the one we obtained here from the spin-flop transition, reported in Ref. [136]. Fig. 4.23 shows that the out-of-phase susceptibility becomes zero for $T \geq 22$ K, indicating that for temperatures higher than 22 K the nanoparticles are in the superparamagnetic regime.

We next discuss the origin of the magnetic moment, which is estimated from the linear susceptibility. Using Eq. (4.19) and the expressions provided in Sec. 1.2.7, it is possible to write

$$\left(\chi' - \chi_{\mathrm{AF}}\right) T = n\left[\frac{\mu_{\mathrm{unc}}^2}{\mathrm{k_B}} + 8\mathrm{k_B}T^2\left(\frac{g\mu_{\mathrm{B}}}{\hbar\omega_0}\right)^2\right] \tag{4.20}$$

where n is the number of particles per akaganéite volume, which can be determined using the size distribution obtained by TEM. In order to extract the thermoinduced contribution χ_{AF} of the nanoparticles was taken, at each temperature, as the value measured on the bulk

sample multiplied by 1.5 (see Fig. 4.18). The quantity $(\chi' - \chi_{AF})\,T$, displayed in Fig. 4.24, increases from 22 to 50 K, shows a maximum near 50 K and then decreases with increasing T. For temperatures higher than 22 K and below T_N, $(\chi' - \chi_{AF})\,T$ follows Eq. 4.20. The fit gives $\hbar\omega_0 = 7.66 \pm 0.05$ K. For temperatures $T > T_N$ the material is paramagnetic so

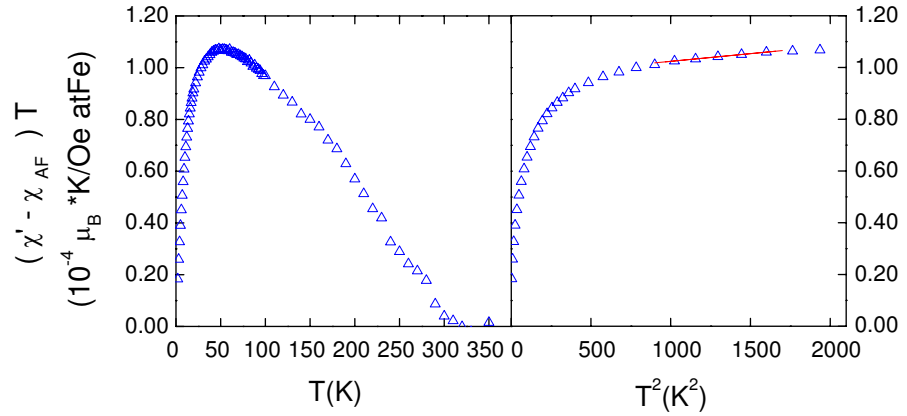

Figure 4.24: $(\chi' - \chi_{AF})\,T$ of akaganéite nanoparticles; the solid line is a fit to Eq. (4.20).

that χ' equals χ_{AF} and, therefore, the term in the brackets in Eq. (4.20) becomes zero. Fig. 4.24 shows that $(\chi' - \chi_{AF})\,T$ is proportional to T^2, as predicted by Eq. (4.20) [64] for the population of the homogeneous mode of spin waves. The decrease is probably caused by the population of higher energy modes.

At $T \to 0$ the thermoinduced contribution should vanish. The uncompensated magnetic moment can then be estimated to be $\mu_{unc} = 93.87 \pm 0.05\ \mu_B$. Let us notice that μ_{unc} contributes significantly to the susceptibility (see Eq. (4.20)) following a Curie dependence with temperature in the superparamagnetic regime [64]. When this contribution is larger than the contribution due to the thermoinduced magnetic moment the susceptibility decreases increasing T. This is clearly our case, as shown in Fig. 4.23. Although the magnetic moment increases from 22 to 50 K, the susceptibility still decreases as T increases.

In order to support our interpretations, we calculate the spin wave energy modes for the akaganéite nanoparticles. As we explained in Sec. 1.2.7, at finite temperatures an antiferromagnetic material can access higher energy states and the system is perturbed from its ordered configuration at T=0. These states of higher energy can be described as a population of spin wave modes. The energy of the ground state $k = 0$ at $H \to 0$ reduces the Eq. (1.42) to

$$\hbar\omega_0 = g\mu_B \{H_{AN}\,(2H_E + H_{AN})\}^{1/2} \tag{4.21}$$

The anisotropy field for akaganéite is $H_{AN} = K/M_S = 13$ kOe, where $K = 5.5 \times 10^{6}$ erg/cm^3 and $M_S = 413.6$ emu / cm^3 were determined in Sec. 4.3.6 and Sec. 4.3.1 respectively.

The exchange field H_E may be inferred from the Néel temperature, using mean field theory that predicts $T_N = H_E g\mu_B (S+1)/3k_B$, which gives $H_E = 2.1 \times 10^6$ Oe. In principle, H_E could also be estimated from $\chi(T_N) = 5 \times 10^{-7} \mu_B$/OeatFe, using the relation $H_E = M_S/\chi(T_N)$, which gives $H_E = 3.5 \times 10^6$ Oe. However, this expression only holds for magnetic structures in which next nearest neighbor interactions can be neglected. Since the magnetic

structure of akaganéite involves second neighbor interactions (see Sec. 1.1.1) we will use the mean field value $H_E = 2.1 \times 10^6$ Oe.

Using H_{AN} and H_E values determined above, gives $\hbar\omega_0 = 31.5$ K. In this mode all the atomic spins precess in phase and a thermoinduced contribution arises because the amplitude of the precession is different for each sublattice. In this mode all the atomic spins precess in phase and a thermoinduced contribution arises because the amplitude of the precession is different for each sublattice. This energy is nearly 4 times larger than the value determined from the experimental susceptibility. This discrepancy means that the simple Eq. (4.21) does not properly describe the elemental magnetic excitations of akaganéite nanoparticles.

The energy for the higher excited population modes is calculated from Eq. (1.42),

$$\hbar\omega_k = g\mu_B \left[(H_E + H_{AN})^2 - H_E^2 \left(1 - \frac{2k^2a^2}{z} \right) \right]^{1/2} \tag{4.22}$$

The first excited state for the spin-wave traveling through the length of the nanoparticle $k = \pi/L$ will be populated for a nanoparticle of 18 nm length at an energy $E_{k=\pi/L} = 64$ K. When the second excited state $k = 2\pi/L$ becomes populated at 97 K the decreasing of the average magnetic moment with the temperature is noticeable. Higher modes become populated with increasing temperatures and finally at the Néel temperature the sublattice magnetization becomes zero.

The value obtained from the fit for $\hbar\omega_0 = 7.66$ K is much lower than the one we have just calculated. This fact suggests that the model we employed for the fitting, that was actually developed for a bulk material, might be too simple to describe the spin wave propagation in this system.

Effect of uncompensated magnetic moments

The energy levels population described in previous section have been calculated for a perfect antiferromagnet in which at $T = 0$ the spontaneous magnetization completely vanishes. However, the existence of an uncompensated magnetic moment also influences the spin wave excitation energies, as described in Refs. [64, 142]. The spin wave excitation energy of the uniform mode of a system with an uncompensated magnetic moment can be calculated using the expression provided in Ref. [142],

$$\hbar\omega_0 = g\mu_B \left[\pm \frac{H_E}{2} (\zeta - 1) + \sqrt{2H_E H_{AN} + H_E H_{AN} (\zeta - 1) + \left(\frac{H_E}{2} (\zeta - 1) \right)^2 + H_{AN}^2} \right] \tag{4.23}$$

where $\zeta - 1 = \mu_{unc}/M_S V$. Assuming that the uncompensated magnetic moment $\mu_{unc} = 93.87$ μ_B, this gives energies $\hbar\omega_{0,+} = 32.8$ K and $\hbar\omega_{0,-} = 30.4$ K for the upper and lower modes, respectively. The energy of the latter modes are still four times larger than the experimental $\hbar\omega_0 = 7.66$ K. We suggest that the excitation energies of the modes that determine this phenomenon are lower than those assigned to the homogeneous spin-wave mode. This can be associated to the fact that bulk H_E and H_{AN} values have been used to calculate the energy levels of nanoparticles. As we mentioned previously, this result may also indicate that other energy excitations, perhaps associated with the local excitation of surface spins contribute, or even become dominant, in the case of AF nanoparticles.

Magnetic interactions

In Sec. 1.2.5 we said that the increase of the magnetic moment with the temperature is attributed by some authors to an inappropriate use of Langevin expression in systems where magnetic interactions are not negligible. In this section we will check if the magnetic moment increase with temperature in akaganéite nanoparticles can be attributed to magnetic interactions. First we will apply the model developed by P. Allia described in Sec. 1.2.5 to calculate what they called 'actual magnetic moment'. Then, we calculate an average distance from the interaction energy. Finally we will show that the ferrofluid obtained from the dilution of the nanocomposite show similar magnetic properties as that found for the composite.

We first apply the model of P. Allia to the susceptibility of akaganéite nanoparticles. We should point out that this model was developed in ferromagnetic nanoparticles, although it has been used to explain also the increase of magnetic moment in antiferromagnetic nanoparticles systems. We pointed out in Sec. 1.2.6 that antiferromagnetic nanoparticles have a finite contribution to the spontaneous magnetization from the decompensated magnetic moments such that the magnetic response is the superposition of both the intrinsic antiferromagnetism and the uncompensated magnetic moment contribution. If the antiferromagnetic nanoparticles are close enough, dipolar interactions between the uncompensated magnetic moment of neighboring particles can appear

$$\mu \simeq \left[\frac{3k_{\mathrm{B}}T}{N}\left(\chi - \chi_{\mathrm{AF}}(T)\right)\right]^{1/2} \tag{4.24}$$

as described in Sec. 1.2.6.

The inverse of $\chi - \chi_{\mathrm{AF}}(T)$ is represented in Fig. 4.25. The antiferromagnetic susceptibil-

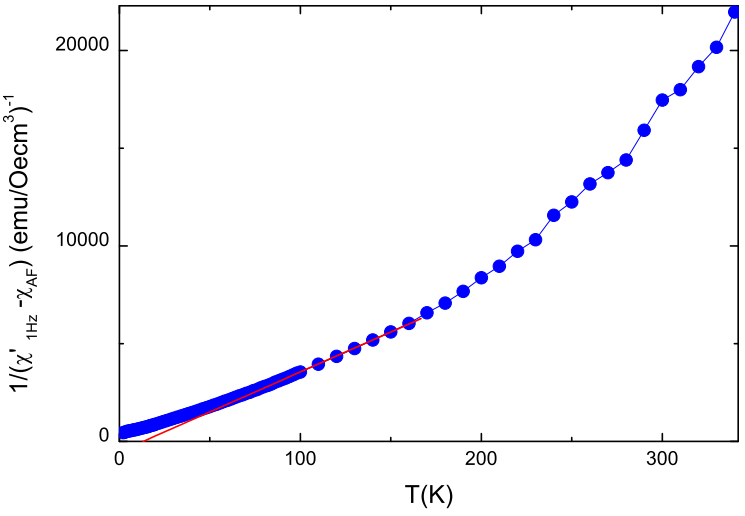

Figure 4.25: Inverse of $\chi - \chi_{\mathrm{AF}}(T)$ for the akaganéite nanoparticles to determine the ordering temperature T^*.

ity $\chi_{\mathrm{AF}}(T)$ is that obtained in Sec. 4.3.3 from bulk akaganéite. We notice that in superparamagnetic region ~ 22 K - 260 K is rather difficult to define a linear region to perform the linear fit. We choose the temperature region as far as possible from T_{N} to diminish as much as possible the sublattice magnetization dependence with temperature. In a first approximation we neglect the magnetic moment distribution that leads using equation Eq. (1.36) to a temperature $T^* = -13.14$ K. The magnitude that includes magnetic moment distribution ρ can be calculated assuming that uncompensated magnetic moments are randomly distributed on the surface nanoparticle. Then $\mu = \sqrt{N_{\mathrm{atSurf}}}\mu$ and $\rho = <\mu^2> / <\mu>^2 = <Surf> / <\sqrt{Surf}>^2$. Surface distribution is determined from TEM distribution analysis. This leads to $\rho \sim 1.$ and $T^* = -13.14$ K. At $T > 13.14$ dipolar interaction does not influence the value of the magnetic moment. Then the thermoinduced magnetic moment, observed in the region ~ 22 K - 260 K, can not be attributed to dipolar interaction effects.

To determine the actual magnetic moment from the reciprocal susceptibility fit to Eq. (1.39) we can follow procedure described in Sec. 1.2.5. It is displayed in Fig. 4.26. Notice

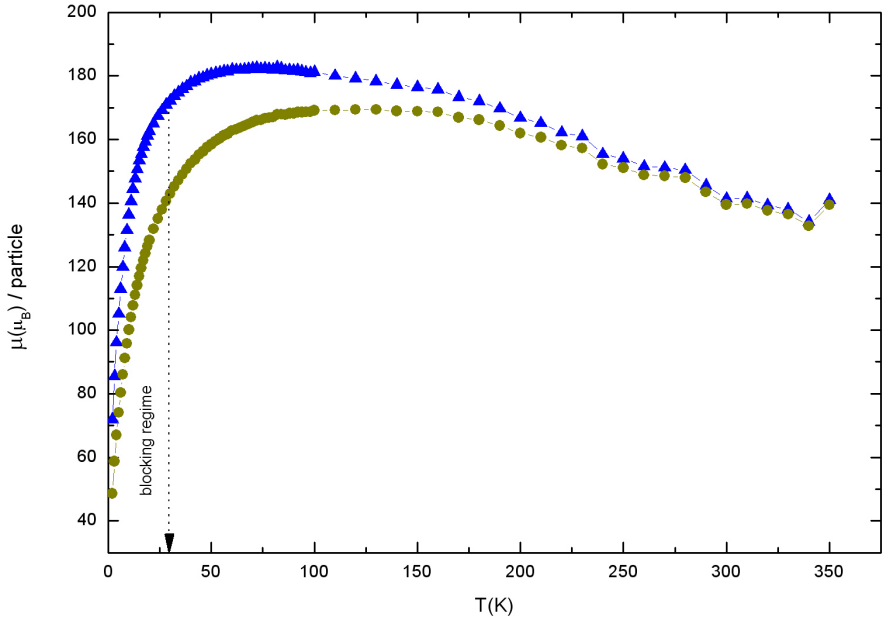

Figure 4.26: Magnetic moment per particle obtained through the model of P.Allia (•) and that obtained straight from $\chi - \chi_{\mathrm{AF}}$ (▲).

that the thermoinduced magnetic moment arises at larger temperatures than those obtained straightforward from $\chi - \chi_{\mathrm{AF}}$. Besides, the magnetic moment calculated through both methods tends to converge to the same value as the temperature $T \to T_{\mathrm{N}}$. We can conclude that the magnetic moment obtained taking into account dipolar interactions does also increase with the temperature.

Lets calculate for this interaction temperature T^* the average interparticle distance. The model of P. Allia relates the temperature $T^* = 13.14$ K to the dipolar interaction energy

for a particle with its nearest neighbors through the expression

$$k_B T^* = \varepsilon_D = \alpha\mu^2/d^3 \tag{4.25}$$

where d is the average interparticle distance and α is a constant that accounts for the geometrical arrangement of nanoparticles. For this parameter the value of $\alpha^2 \sim 10-20$ is proposed in Ref. [49]. We calculated in Sec. 4.4.2 that the uncompensated nanoparticle magnetic moment is $\sim 93.87\ \mu_B$. With these values, the interparticle distance to produce a magnetic interaction of 13.14 K should be about $d \sim$1 nm. This distance corresponds in the scale of the TEM images, shown in Sec. 4.2.2, to nanoparticles nearly overlapped. However although nanoparticles seem to form groups of particles they are not aggregated.

The model of P. Allia can be used to determine the strength of magnetic interactions through the calculus of the parameter T^*. However, as already pointed out by M. El-Hilo et al [56] parameters obtained with this model should be taken with care, as the influence of some parameters, such as the dependence of sublattice magnetization with temperature or the effect of the blocking temperature on the susceptibility, makes the value determined for T^* ambiguous.

Therefore we finally synthesized a ferrofluid diluting the akaganéite composite. In Sec. 4.2.2 we showed TEM image of the ferrofluid. In this images we appreciate that the polymer has been dissolved and the nanoparticles are completely separated from each other. In Fig. 4.27 we show $\sqrt{(\chi' - \chi_{AF})T}$ for both ferrofluid and nanocomposite. In this figure we

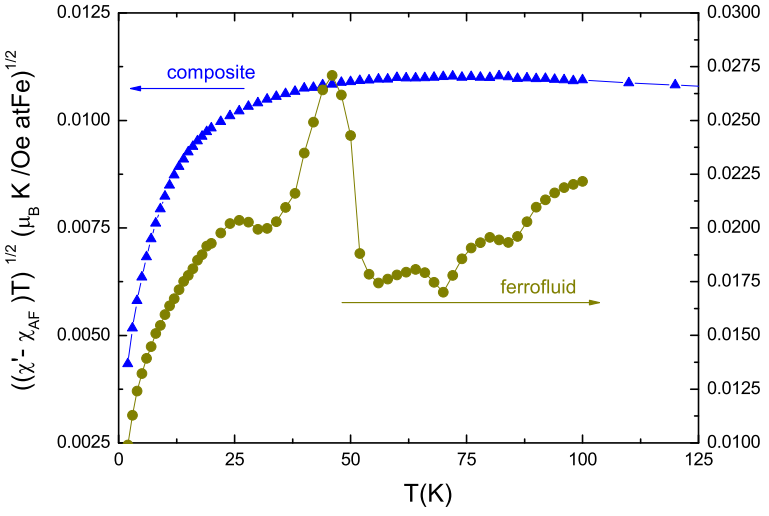

Figure 4.27: $\sqrt{(\chi' - \chi_{AF})T}$ for both ferrofluid (•) and nanocomposite (▲).

appreciate that $\sqrt{(\chi' - \chi_{AF})T}$ increases with the temperature for both samples in the region temperature where the thermoinduced effect is expected.

We finally conclude that although dipolar interactions may slightly influence the magnetic response for akaganéite nanoparticles, the thermoinduced effect does not arises from magnetic interactions.

4.5 Conclusions

In this chapter we have presented structural and magnetic properties of akaganéite bulk material. We have shown that it is an antiferromagnet with a Néel temperature around T_N=260 K, an effective magnetic moment of μ_{eff}=4.4 and an anisotropy constant K =5.5 × 10 ^{6} erg/cm^3.

We have also shown that the antiferromagnetic susceptibility is 1.5 times larger for the nanocomposite than the χ_{AF} of the bulk. The dependence with temperature of the antiferromagnetic susceptibility is quite similar for bulk and nanoparticles.

Finally, we show that the magnetic moment increases with temperature in the superparamagnetic regime and it can be attributed to the population of the ground state of spin wave mode [62].

Chapter 5

Surface effects in maghemite nanoparticles

A consistent model is presented for the variation of saturation magnetization with particle size in maghemite nanoparticles, based on the existence of a magnetically disordered layer with a constant thickness of 1 nm. Magnetization measurements have been performed on maghemite polymer nanocomposites with low size dispersion and a regular distribution of particles in the matrix. A representative number of samples have been studied with a diameter size in the range from 1.5 to 15 nm and ±10% of size dispersion. For particles smaller than 3 nm, layer thickness increases rapidly and M_S is already zero for 2.5 nm particle size. A good size characterization for the nanoparticles is a fundamental step in this analysis. Here, we also present results on the small-angle X-ray scattering examination of these maghemite nanocomposites.

5.1 Introduction

Despite the number of studies on the magnetic properties of ferrimagnetic iron oxide nanoparticles, their magnetic behavior is not yet well understood. Magnetization of ferrimagnetic nanoparticles is lower than that of bulk materials, it does not saturate at rather high fields and it shows open and shifted hysteresis loops as well as irreversibility in ZFC-FC curves. Some of these features can be explained by anisotropy effects or finite size effects such as misalignment of antiferromagnetic sublattices and structural disorder [143–146]. However, a variety of experimental techniques and computer simulations showed that the incomplete coordination of superficial ions and the likely occurrence of surface structure defects are determinant for this kind of behavior [147–155]. These defects can lead to magnetic disorder extending into the core within a layer of a given thickness. Thus, the most accepted theoretical model to explain the decrease of magnetization of nanoparticles with particle size is based on a bulk-like ferrimagnetic core and a shell composed of disordered moments [154–162]. Previous experimental determinations of shell thickness by Mössbauer, ZFC-FC measurements or neutron techniques [147, 148, 152, 158, 159, 162] are mostly based on just one sample or on various samples within a narrow particle size range. A comparison between these values shows large variations for similar particle sizes and no correlation between shell thickness and particle size. Shell thickness can be calculated from the decrease of saturation magneti-

zation, M_S, with respect to the bulk, using published values of M_S on series of samples with several average particle sizes [163–166]. This calculation also would lead to scattered values and inconsistency on the variation of shell thickness with particle size. Such a dispersion of values may come from differences in sample preparation and/or characterization, because the magnetization of nanoparticles is greatly influenced by a variety of factors related to sample quality (size dispersion, superficial and internal crystal defects [144, 145], inter-phase chemical interactions [8, 167–169] and inter-particle magnetic interactions [49, 170]). In this work, we propose a simple model for the variation of saturation magnetization with particle size, based on the existence of a magnetically disordered layer with a constant thickness of 1 nm. For particles smaller than 3 nm, layer thickness increases rapidly and M_S is already zero for 2.5 nm particle size. This model fits extraordinary well with obtained magnetization data, thanks to the use of nanocomposite samples containing isolated particles with narrow size distribution, high crystalline perfection and regular inter-particle separation. In addition, this model agrees with the scattered data of previous works.

5.2 Synthesis

We studied maghemite polyvinylpyridine (PVP) nanocomposites. The samples were prepared by basic treatment of PVP-Fe precursor films containing Rb, Fe(II), Fe(III) and bromide ions following procedure described in Ref. [30]. First, we prepare a stock solution by dissolving weighted amounts of RbBr, $FeBr_2$ and $FeBr_3$ in a volume of water. In the process of dissolution, $FeBr_3$ partially decomposed into $FeBr_2$ and Br_2. The final content of Fe(II) in the stock solution was determined by titration with $K_2Cr_2O_7$ using ferroine as an indicator. Two different stock solutions have been used: a) stock solution 1 contains 0.5 mol/L of RbBr and 1 mol/ L of total iron and 15 % of Fe(II) with respect to total iron; b) stock solution 2 contains 1.07 mol /L of RbBr and 2.14 mol /L of total iron and 35 % of Fe(II) with respect to total iron. Two series of maghemite/PVP composite samples were prepared using stock solutions 1 and 2, respectively. For the first series, different volumes of stock solution 1 were added to a solution of 0.1 g of poly(4-vinylpyridine) (PVP) in 4 mL of a water:acetone (1:1). The mixture was dried in an oven at 40 °C for 24 h to obtain a film of the Rb-Fe-Br-PVP precursor compund. This film was immersed in 5 mL of a 1 M NaOH solution for 1 h, washed with water and finally dried in an oven at 200°C for 24 h, in order to improve the crystallization of the particles. Samples S3, S4 and S7 were prepared in this way, using volumes of stock solution of 0.1 mL, 0.25 mL and 2 mL, respectively. The procedure for the preparation of the second series of samples was similar but using stock solution 2 and larger amounts of reactants. The amount of PVP was 0.6 g and the volumes of stock solution 2 were 0.1 mL, 0.3 mL, 0.6 mL, 1.2 mL and 4.5 mL for samples S1, S2, S5, S6 and S8, respectively. Additionally, we prepared maghemite powders samples in order to study the influence of the polymer scattering in the SAXS profiles of the nanocomposites. In this preparation, the stock solution (stock solution 3) contained 0.05 mol / L of RbBr, 0.1 mol / L of total iron and 11% Fe(II) with respect to total iron. The maghemite powders were prepared by addition of 300 mL of 0.1M NaOH to 100 mL of stock solution, with magnetic stirring, at room temperature. The precipitate was filtered, washed with a saturated sodium oxalate solution and then with water and finally dried in an oven at 200°C for 24 h.

5.3 Characterization

5.3.1 XRD

X-ray diffraction measurements were performed at RT with a Rigaku D-max B diffractometer. Diffraction patterns were recorded with 2θ ranging from 10 to 70 °. The XRD patterns shown in Fig. 5.1 have a broad peak around 20° also observed in the pattern of the isolated polymer matrix. The set of peaks shown in the XRD patterns of the nanocomposites match

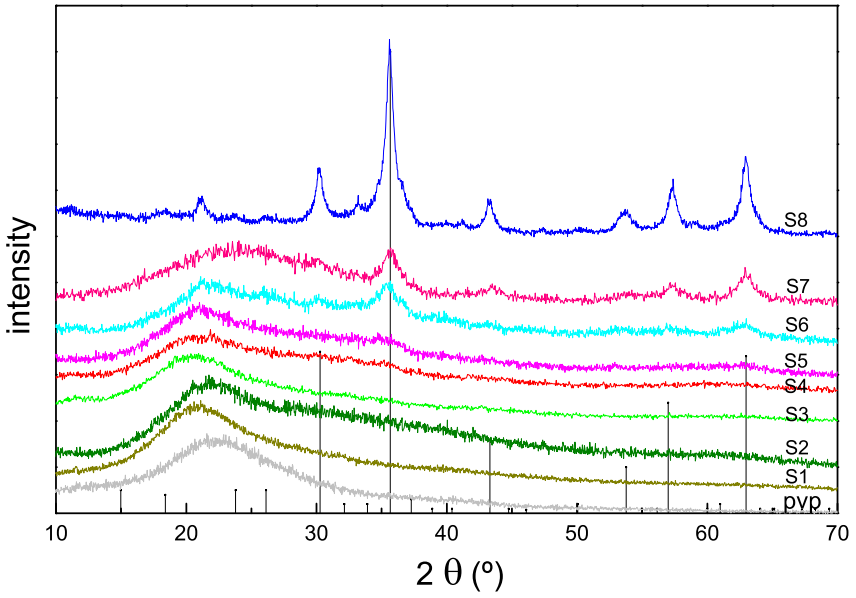

Figure 5.1: XRD patterns of γ-Fe_2O_3 database reference, the polymer and the maghemite nanocomposite samples S1 to S8.

well with the pattern of the maghemite. The narrowing of XRD peaks indicates a gradual increase in the particle size with the [Fe]/[PVP] ratio.

5.3.2 FTIR

The nanocomposites have also been examined by infrared spectroscopy in the region from 400 to 700 cm^{-1}. Infrared spectra were taken on KBr pellets using a Perkin Elmer Spectrum One instrument. The FTIR spectra of PVP polymer, nanocomposite and maghemite γ-Fe_2O_3 nanoparticle powders after annealing at 200 °C samples are shown in Fig. 5.2. The bands in the region from 400-700 can be attributed to Fe-O vibrations associated with cationic ordering and crystal perfection [171]. We notice that the absorption of the polymer matrix dominates the spectra of the composite. However, the spectra of nanocomposite shows bands

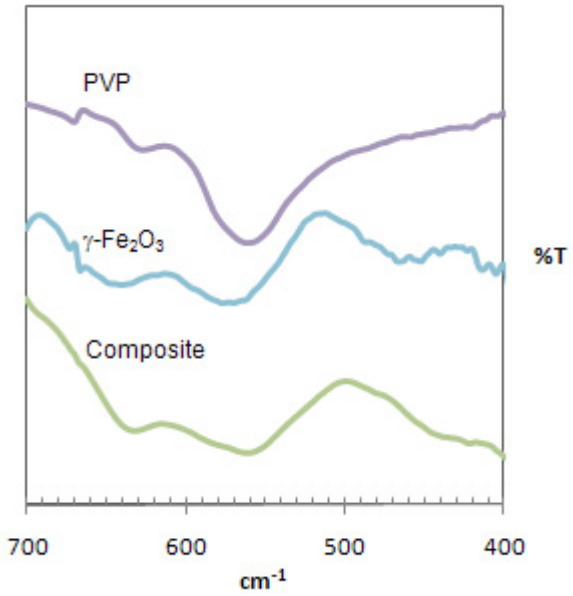

Figure 5.2: FTIR spectra of polyvinylpyridine (PVP) polymer, maghemite (γ-Fe_2O_3) nanoparticle powders after annealing at 200 °C and maghemite-polyvinylpyridine nanocomposite.

at 430 and a shoulder at 580 cm^{-1} and 640 cm^{-1}. Bands at 430 and 640 are forbidden in a perfect spinel structure, such as magnetite and they appear only in maghemite [171]. The other band at 580 cm^{-1} can also be assigned to maghemite structure.

From XRD and FTIR spectroscopy we can thus conclude that the only iron oxide phase present in nanocomposite is maghemite.

5.3.3 Electron microscopy

We performed transmission electron microscopy in a Philips CM30 with a 1.9 Å point resolution. All the composite samples used in this chapter have been characterized by TEM. Representative images of the samples are included in Fig. 5.3 and Fig. 5.4.

The images show particles with a size increasing regularly from sample S1 to sample S8. The shape of the particles is spherical, but in sample S8 most of them are already faceted. The particles are homogenously spread along the matrix. Particles in sample S1 showed a poor contrast with respect to matrix due to their low density, which made difficult to perform a particle size analysis.

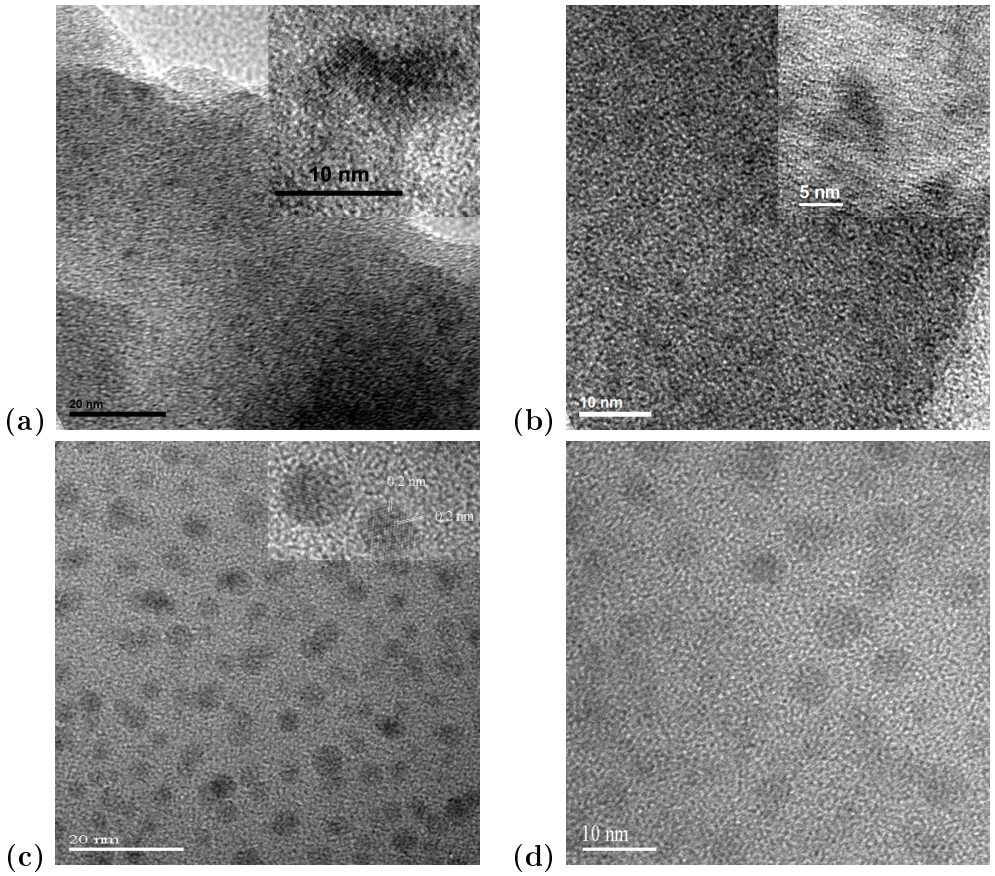

Figure 5.3: Representative TEM images of maghemite nanocomposite sample S1 (a), S2 (b), S3 (c), and S4 (d), show that nanocomposite contains isolated nanoparticles. The nanoparticle's average size increases regularly from sample S1 to S4.

Nevertheless, measurements on a few particles with a clear contour yielded a particle size of 3.1 ± 0.4 nm. For the rest of the samples, a particle size analysis was performed. The resulting distributions of particle's size are shown in Fig. 5.5. The average size and the standard deviations were calculated statistically over the sizes obtained from TEM analysis. They are shown in Table 5.1. The mean diameter increases with the [Fe]/[PVP] concentration, in accordance with the results obtained in XRD. However, we notice that the particle size in samples synthesized with stock solution 2 is larger than those synthesized with stock solution 1, for a similar [Fe]/[PVP] ratio. This is clearly shown in Fig. 5.6. Thus, the particle size depends not only on the [Fe]/[PVP] concentration, but also increases with the Fe(II)/Fe(III) ratio of the iron bromide solution used in the preparation [30]. In addition, the average sizes corresponding to those samples from the same stock solution increases almost linearly with the iron molar concentration. In fact, the data seem a bit scattered around this tendency, which can be assigned to some lost of accuracy in the determination of the size in the analysis of the TEM images, due to the low contrast of the particles.

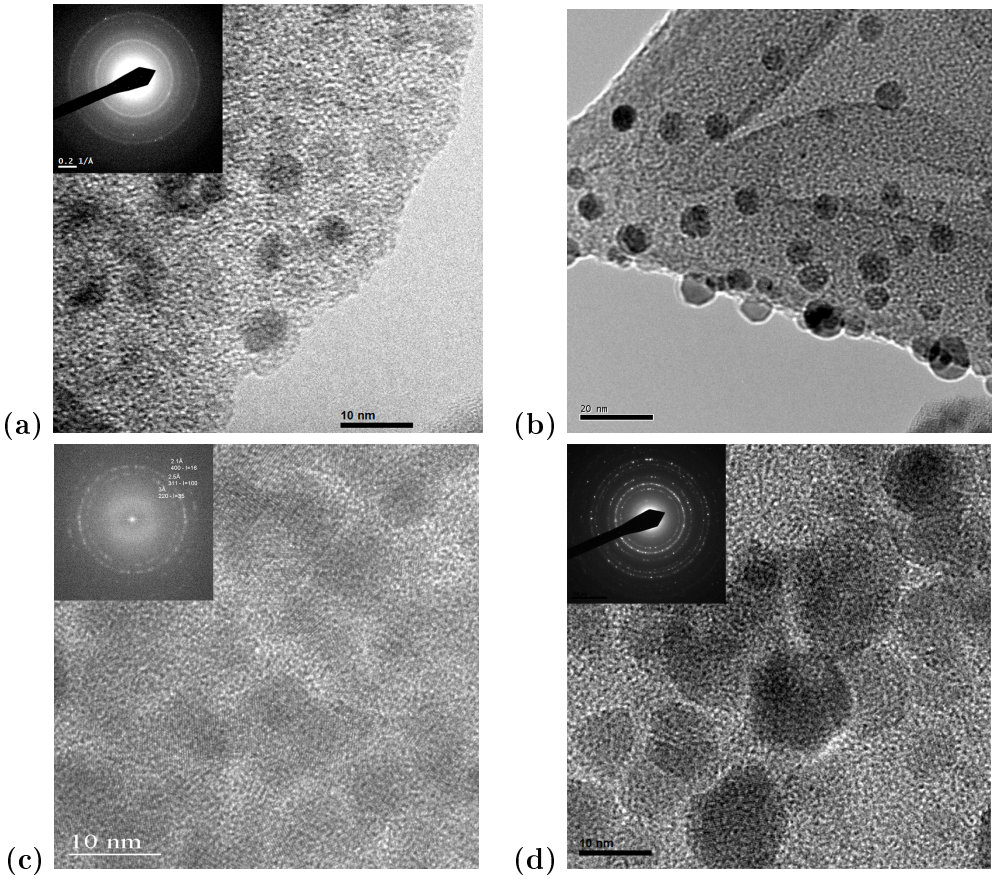

Figure 5.4: Representative TEM images of maghemite nanocomposite sample S5 (a), S6 (b), S7 (c), and S8 (d), show that nanoparticles are spread in the polymer matrix. The average particle's size increases regularly from sample S5 to S8.

Table 5.1: Characteristics of the nanocomposite samples.

	[Fe]/[PVP]	$\langle D \rangle$ (nm)	Std. Deviation
S1	0.032	3.1	0.4
S2	0.101	3.4	0.5
S3	0.107	4.1	0.6
S4	0.268	4.5	0.4
S5	0.194	5.2	0.9
S6	0.391	6.4	1.1
S7	0.828	7.2	1.4
S8	1.479	12.7	3.2

The crystal structure was determined from high resolution (HREM) images and electron diffraction (ED) patterns. In samples S1 to S4, ED patterns were diffuse, but interplanar

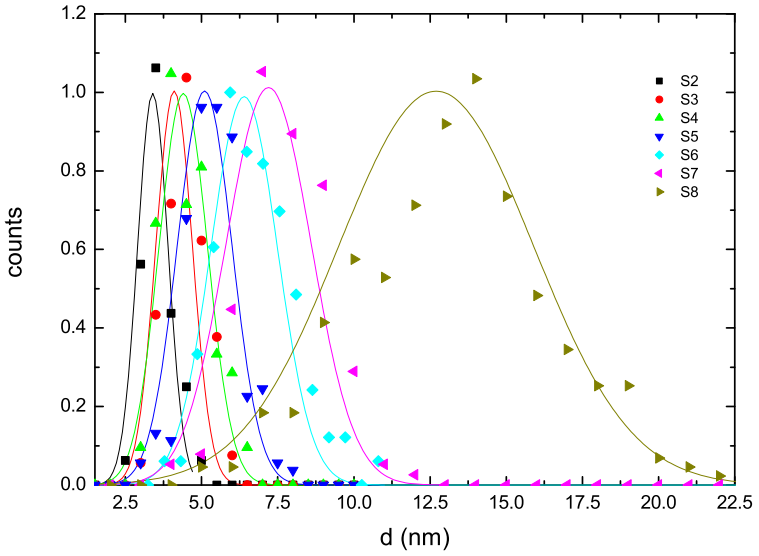

Figure 5.5: Size distribution histograms of the nanocomposite samples S1 to S8. Continuous line is the gaussian function calculated with the mean size and standard deviation calculated statistically.

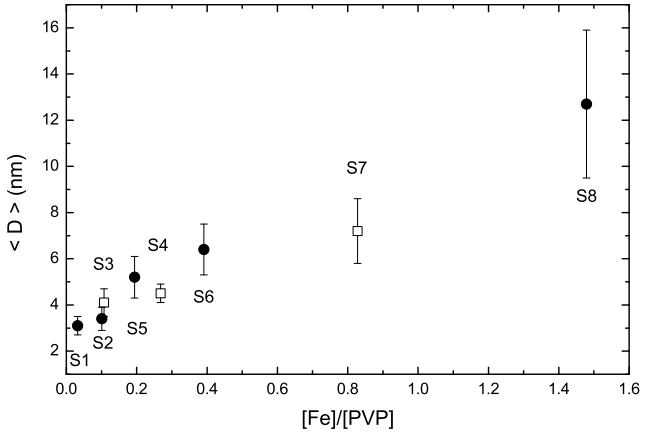

Figure 5.6: The average size obtained by TEM increases almost linearly with the [Fe]/[PVP] concentration in the nanocomposite samples.

distances in HREM images (insets in Fig. 5.3 (a)&(c)) were consistent with maghemite crystal structure. ED patterns in sample S5 (inset in Fig. 5.4(a)) showed already rings at distances that could be assigned to (220), (311) and (400) reflections in maghemite structure. Patterns in samples S6, S7 and S8 (insets in Fig. 5.4) were very clear and typical of maghemite structure, without any evidence of the presence of another iron oxide phase in the samples.

5.3.4 SAXS

Reliable particle size values have been obtained from small angle X-ray scattering data analysis [121]. SAXS experiments were carried out at beamline ID01 of the European Synchrotron Radiation Facility (ESRF). The nanocomposite samples for SAXS experiments were prepared by grinding the as-prepared films in a mortar and then pressing the grains into pellets. Maghemite pure powder samples were prepared in two ways: (1) by directly pressing the powders into pellets; and (2) by mixing maghemite powders and polymer grains in a mortar and pressing the mixture into pellets. Most of the pellets have a thickness of roughly 0.2 mm. SAXS images obtained from the nanocomposites consisted of isotropic rings and were integrated azimuthally for further analysis. Noise from slits and windows has been subtracted and statistical errors from the photon flux have also been taken into account in the integration. Measured curves were normalized for variations of the primary intensity. Absolute scattering intensities were calculated from the normalized intensity and film/pellet thickness. The intensity is represented as a function of the modulus of the scattering vector $q = (4\pi/\lambda)\sin\theta$, λ being the wavelength and 2θ being the scattering angle.

Polymer scattering contribution

We analyzed the contribution of the polymer scattering in the SAXS profiles of the nanocomposites. Fig. 5.7 shows that log-log plots of SAXS from the as prepared films and pressed powder pellets of another nanocomposite sample prepared using an iron/polymer ratio of 0.04. SAXS curves corresponding to a pure polymer pellet and a pellet prepared by mixing maghemite and polymer powders are also shown in this figure.

We notice that all the scattering profiles, including those of the pure polymer and the as prepared film, show a power-law regime in the low-q region ($q < 0.1$ nm^{-1}). Therefore, this scattering intensity is not an artefact introduced during the preparation of the pellet and can be associated to the scattering from the polymer. We fitted the polymer intensity to a Porod expression [69],

$$I_{\mathrm{PVP}}(q) = I_0 + Aq^{-\mathrm{n}} \tag{5.1}$$

that yields n = 3.31. The ideally smooth surface gives n = 4 and a Gaussian polymer gives n = 2. So that this scattering intensity probably comes from the rough surface of grains formed by folded polymer chains.

Fig. 5.8 shows the variation of the absolute scattering intensity with q for the nanocomposite sample S4. The scattering curve of the nanocomposite shows three regions in accordance with reports on granular and mesoporous media [172]: (I) a low-q region that follows a power-law regime; (II) an intermediate region that follows a Guinier regime; and (III) a high-q region that also shows a power-law regime. We notice in Fig. 5.7 that the polymer curve shows a constant scattering for $q > 0.1$ nm^{-1}, whereas the curves containing maghemite nanoparticles have enhanced intensities in this region. The scattering in region (I) can be therefore associated to the polymer. In the inset of Fig. 5.8, a high-resolution TEM image of a slice of the sample shows isolated spherical particles uniformly distributed in the matrix. A

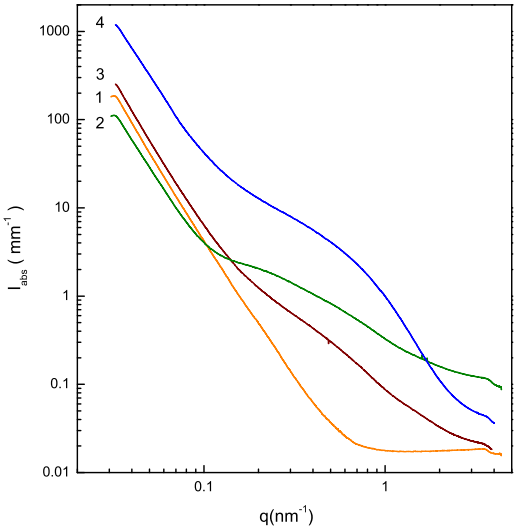

Figure 5.7: SAXS data of a pure polymer pellet (1), a maghemite-polymer as-prepared nanocomposite film (2), a pellet of the same sample (3) and a pellet made by mixing and pressing polymer and maghemite powders (4).

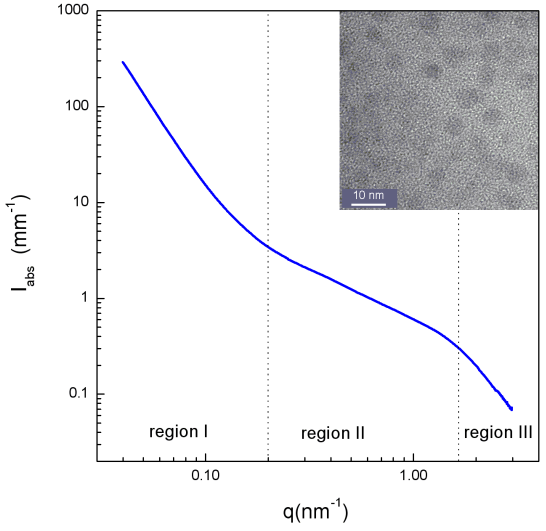

Figure 5.8: SAXS of a pellet of sample S4, containing a 3 % volume ratio of spherical particles with $D = 4.5 \pm 0.4$ nm. Vertical lines separate regions of Porod regimes (regions I and III) and a Guinier regime (region II). Inset: HRTEM image of S4.

particle population analysis on the TEM images yields a monomodal size distribution with an average particle size D of 4.5 ± 0.5 nm. The intensity of the scattering associated to this size is in the angular region (II) and (III), so that it can be associated to the scattering of the nanoparticles.

SAXS of a nanocomposite series

In this section we analyze the dependence of the average size determined by SAXS with the iron / poly(4-vinylpyridine) molar ratios used in the preparation of the nanocomposite samples. As we anticipated in Sec. 5.3.3 the mean size depends not only on the total iron concentration, but also on the Fe(II)/Fe(III) ratio, so that we will focus in this section on samples prepared from the same stock solution: S1, S2, S5, S6 and S8. The SAXS curves of the nanocomposites shown in Fig. 5.9 also display a power law in the low-q region due to the polymer and an enhanced intensity due to the nanoparticles. We notice that this enhanced

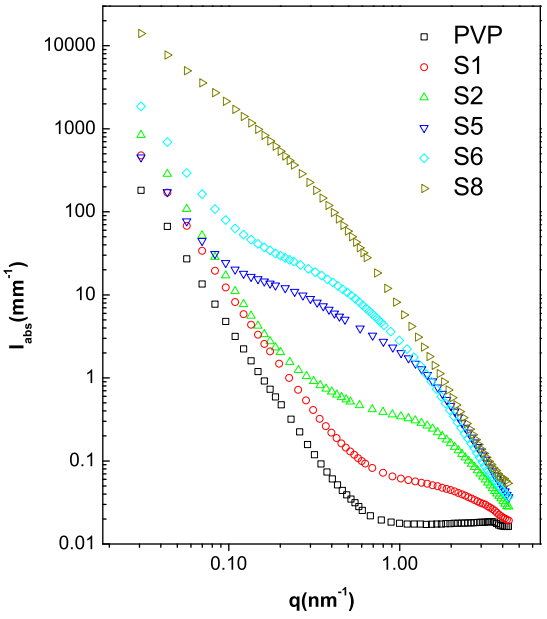

Figure 5.9: SAXS data of maghemite-PVP nanocomposites prepared from different iron/ polymer ratios: 0.032 (S1), 0.101 (S2), 0.194 (S5), 0.391 (S6) and 1.479 (S8).

intensity increases with the iron content, showing an increase of the particles density and/or size. In samples S1 and S2, with low iron content, the nanoparticle scattering shows clearly the Guinier and power-law regimes. As the iron content increases, the power law becomes more visible and its exponent approaches the value of n = 3.60, indicating the existence of particles with rough surfaces. As the iron content increases, the transition from the Guinier to the power-law regime occurs at successively lower q values, which gives a qualitative indication of an increase of the particles size. In samples S3 and S4, with intermediate iron content, the nanoparticle scattering also has a 'knee-like' feature at $q \simeq 0.37$ nm^{-1}. This

knee-like feature can be due either to a second particle population or to particle aggregates and will be analyzed in the following section.

Analysis

As pointed out above, the SAXS intensity of nanocomposites is the sum of the polymer and particle contributions. Polymer scattering is significant in the low-angle region and it can be fitted to equation Eq. (5.1) for all the samples. Regarding particle scattering, two approaches were considered: (i) the existence of a bimodal distribution of nanoparticles and (ii) the existence of a monomodal distribution of nanoparticles and interparticle interactions. The complexity of the system is increased by the fact that the particle size distribution shows a certain dispersion, however low. Consequently, we used an approximate approach for the data analysis.

Let us consider the nanocomposite as a two-electron-density system [69]. The intensity profile can be fitted to a unified equation proposed by Beaucage [72, 73],

$$I_{\mathrm{p}}(q) = G_{\mathrm{p}} \exp\left(-\frac{R_{\mathrm{g}}^2 q^2}{3}\right) + B_{\mathrm{p}} \left(\frac{\{\mathrm{erf}\left[qR_{\mathrm{g}}/\sqrt{6}\right]\}^3}{q}\right)^{\mathrm{p}} \tag{5.2}$$

For a two-electron-density model G_{p} is defined as

$$G_{\mathrm{p}} = N_{\mathrm{p}} \left(\rho_{\mathrm{p}} - \rho_{\mathrm{m}}\right)^2 v_{\mathrm{p}}^2 \tag{5.3}$$

where N_{p} is the number of particles, ρ_{p} and ρ_{m} are the electron densities of particle and polymer matrix, respectively, v_{p} is the particle volume, and R_{g} is the particle radius. For p = 4, B_{p} is the Porod constant defined as

$$B_{\mathrm{p}} = 2\pi \left(\rho_{\mathrm{p}} - \rho_{\mathrm{m}}\right)^2 S \tag{5.4}$$

where S is the nanoparticle surface area. This approach successfully describes scattering from polydisperse nano-objects with different shapes and scattering from multiple-size structures [72]. From the above expression it is possible to determine the parameters R_{g}, B_{p} and G_{p}, which allow us calculate the mean diameter and the standard deviation of the particle distribution [74].

In the samples with larger iron content we introduced another term, $I_{\mathrm{F}}(q)$, similar to that of Eq. (5.2)

$$I_{\mathrm{F}}(q) = G_{\mathrm{F}} \exp\left(-\frac{R_{\mathrm{gF}}^2 q^2}{3}\right) + B_{\mathrm{F}} \left(\frac{\{\mathrm{erf}\left[qR_{\mathrm{gF}}/\sqrt{6}\right]\}^3}{q}\right)^{\mathrm{p}} \tag{5.5}$$

to describe the above-mentioned 'knee-like' feature as arising from a second set of nanoparticles, so that the total intensity can be expressed as

$$I_{\mathrm{t}}(q) = I_{\mathrm{PVP}}(q) + I_{\mathrm{p}}(q) + I_{\mathrm{F}}(q) \tag{5.6}$$

A representative fitting of this expression to the data from sample S6 is shown in Fig. 5.10.

The particle average diameters were determined from $\langle D \rangle_{\mathrm{SAXS}} = 2\sqrt{5/3} R_{\mathrm{g}}$ and $R_{\mathrm{F}} = \sqrt{5/3} R_{\mathrm{gF}}$ using R_{g} and R_{gF} obtained from fitting the SAXS data to Eq. (5.6). Particle volume fractions, $\Phi = N_{\mathrm{p}} v_{\mathrm{p}}$, calculated from G_{p} are also shown in Table 5.2. The iron / poly(4-vinylpyridine) molar ratios used in the preparation of these samples are also included.

The average diameter $\langle D \rangle_{\mathrm{SAXS}}$ increases with the iron content, indicating that as the iron loading increases, particles grow larger. Actually, in Fig. 5.11 we show that the particle

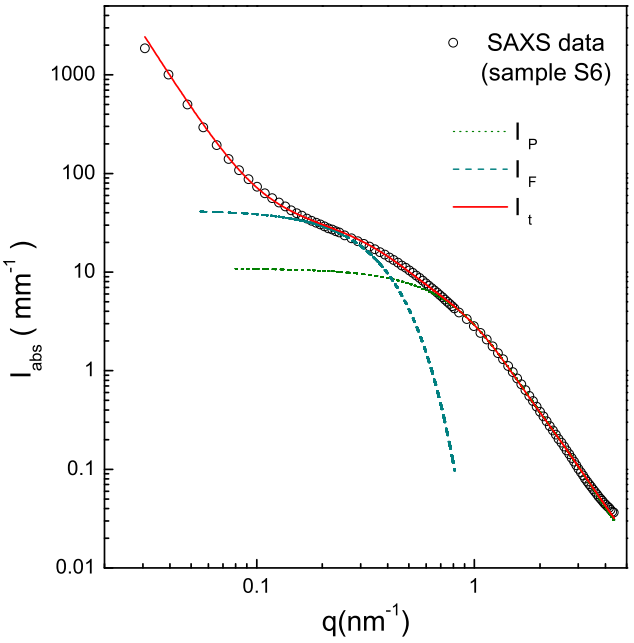

Figure 5.10: SAXS data of sample S6. Lines correspond to: total fitted intensity (I_t, straight line), particle scattering term (I_P, short-dashed line) and a term attributed in the first instance to a second set of nanoparticles (I_F, dashed line).

Table 5.2: Characteristics of some nanocomposite samples obtained from SAXS.

	[Fe]/[PVP]	Volume fraction estimated	Volume fraction SAXS	D_{SAXS}(nm)	Distance (nm) estimated	R_F(nm) SAXS
S1	0.032	0.0031	0.0041	1.55	6.99	7.75
S2	0.101	0.0098	0.0066	2.45	6.78	6.07
S5	0.194	0.0186	0.0178	3.49	7.12	6.07
S6	0.391	0.0367	0.0383	5.16	7.35	6.20
S8	1.479	0.1261	0.9067	10.45	6.35	–

diameter increases linearly with the iron content. The particle diameter obtained by SAXS is slightly smaller than those obtained from TEM analysis. In fact, as shown in Fig. 5.12, the average size determined with SAXS is proportional to that determined by TEM. This feature can be assigned to some systematic artefact performed in the determination of the particle size. Let us remind that the contrast of the nanoparticles in the TEM images (see Sec. 5.3.3) was very poor and, became worst as the size of the particle decreased. We might have skipped some small particles in the analysis of the TEM images and then, the average sizes determined by TEM were overestimated. In addition, the SAXS technique

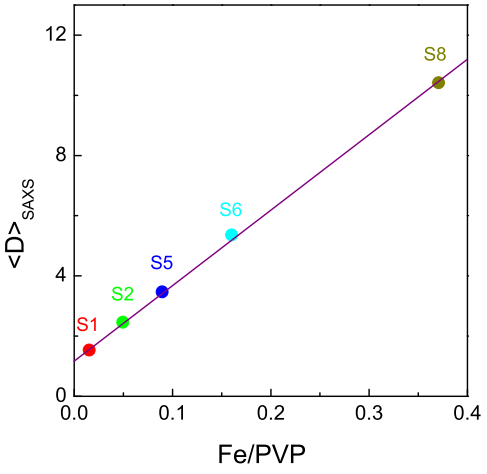

Figure 5.11: Variation of the calculated particle diameter with the iron mass ratio used in the preparation of the sample.

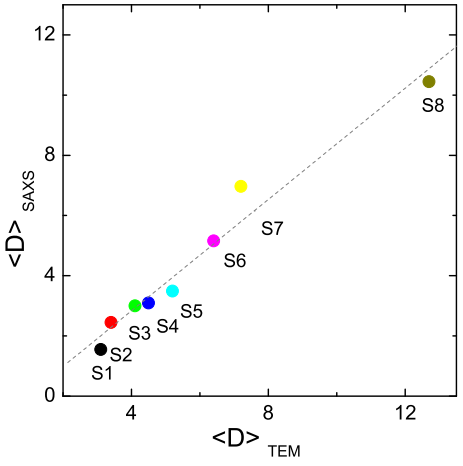

Figure 5.12: Particle diameter determined by TEM vs particle diameter determined by SAXS.

involves the analysis over a wider number of particles than TEM. Then, the average size determined by SAXS is more representative than the one obtained by TEM analysis. This fact is in accordance with the results shown in Fig. 5.11 and Fig. 5.6. We notice that the particle size determined by SAXS is not scattered and increases fairly proportionally with the iron content. Then, we can conclude that the average size determined by SAXS is more

representative than the one determined by TEM so that it will be subsequently used in the analysis of the magnetic properties. In addition, we conclude that the phenomenological Beaucage approach can be used to obtain reliable structural parameters in nanocomposites with multiple-size structures, in accordance with previous results [72, 74].

For moderate particle densities, the volume fraction Φ is in good accordance with the values calculated from the iron content in the sample. However, for large particle volumes, Φ is clearly exceeding the expected values, indicating an enhanced scattering probably due to a structure contribution.

The distance R_F associated with the 'knee-like' feature is roughly constant for samples S2-S6 (6.07-6.20 nm) and it increases in sample S1 (7.75 nm) with the lowest iron content. In approach (ii) we have considered the 'knee-like' feature as arising from interparticle interactions with the SAXS intensity being given by

$$I(q) = NP(q)S(q) \tag{5.7}$$

where $P(q)$ accounts for the particle form factor and $S(q)$ is the structure factor related to interparticle interferences. We studied the presence of interference effects with a Zernike-Prins liquid-like approximation [173], a Born-Green approximation [67, 173] assuming a hard-sphere potential interaction and a distorted one dimensional lattice [174] at the intermediate angle range scattering. However, none of the applied models seem to fit the scattering intensity. In this approach, the 'knee-like' feature corresponds to a smeared maximum corresponding to a characteristic interparticle average distance d that can be estimated as $2\pi/q_{max}$, where q_{max} is the 'knee' position: $d = 20$ and 17 nm for samples S5 and S6, respectively. In the case of sample S6, the value of R_F is not acceptable as being due to particle size, since it would yield a particle diameter of 12.4 nm, out of the distribution range obtained from TEM. In the case of samples with lower iron content (S1, S2 and S5), R_F is far from $\langle D \rangle_{SAXS}$ and if R_F is a particle radius, the samples shall have a distinct bimodal size distribution. Such marked bimodal size distribution would be also apparent in other properties of the nanocomposites, such as the magnetic susceptibility. It is well known that superparamagnetic nanoparticles yield a signal in the out-of-phase a.c. susceptibility, χ", *versus* temperature curve that is highly correlated to particle size and shape and to interparticle interactions. Plots of χ"(T) for samples S2, S5 and S6 (Fig. 5.13) show a single peak, which is strong evidence of a monomodal particle population along the whole sample. Moreover, the existence of a second population of maghemite particles with a radius R_F (Table 5.2) would yield a peak in the susceptibility χ" around 300 K, a feature that is clearly absent in the curves in Fig. 5.13. Furthermore, the Gaussian-like shape of the peak is also indicative of the absence of magnetic interactions between particles and consequently the absence of compact aggregates in the samples. Therefore, the low-angle peak on the scattering intensity profile can not arise from a second population of particles or from dense particle aggregates.

5.4 Magnetic properties

We performed magnetic measurements in a commercial MPMS SQUID magnetometer (Quantum Design). All the samples included in this study yield narrow single peaks in out-of-phase AC susceptibility measurements as shown in Fig.5.13. This confirms that they are composed of a single type of particle with a narrow size distribution.

Fig. 5.14 shows plots of the magnetization against H/T for various maghemite nanocomposites with different particle sizes. It is clear that the magnetization decreases rapidly with

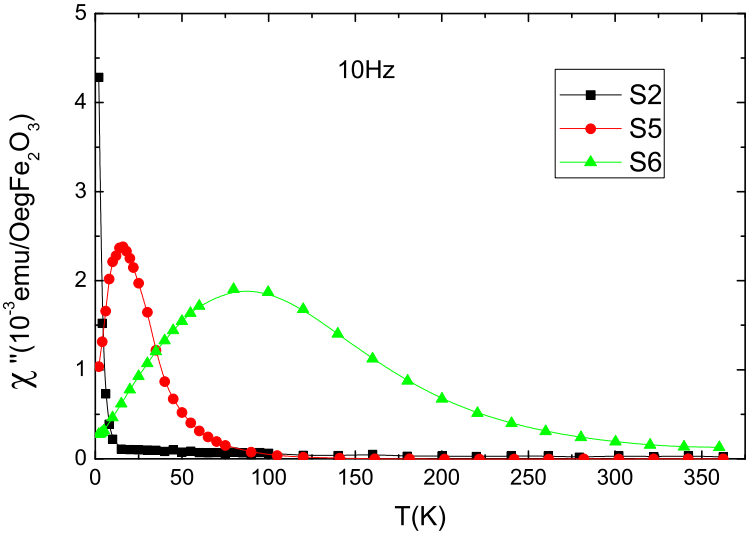

Figure 5.13: Temperature dependence of the out-of-phase a.c. susceptibility, at 10 Hz, for maghemite nanocomposite samples S2, S5 and S6.

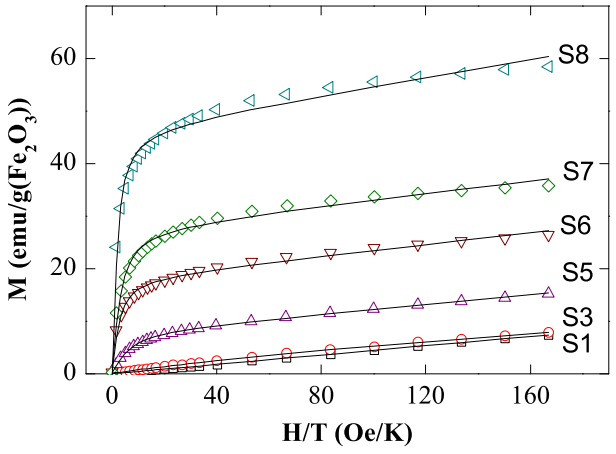

Figure 5.14: Magnetization per gram of iron oxide for a series of nanocomposite samples with different particle sizes, $T = 300$ K. Lines correspond to Eq. (5.8).

Table 5.3: D is particle diameter, M_S is the saturation magnetization derived from fitting to a modified Langevin equation and from high field extrapolation and d is the calculated thickness of the magnetically disordered layer.

Sample	Fe_2O_3 wt%	D (SAXS) (nm)	M_S extra (emu/g)	M_S Lang (emu/g)	χ Lang (emu/g Oe)	d (nm)
S1	2.3	1.55	0	0		–
S2	7.6	2.45	0	0		(1.3)
S3	7.6	2.96	1.5	2.2	1.0×10^{-4}	1.0
S4	16.5	3.05	3	2.9	9.4×10^{-5}	1.0
S5	12.9	3.49	8.5	7.6	1.5×10^{-4}	0.9
S6	22.9	5.16	20	17.4	1.8×10^{-4}	1.0
S7	58.1	6.97	31	26.4	1.9×10^{-4}	1.0
S8	52.9	10.45	52	46.9	2.8×10^{-4}	1.1

particle size. For a particle size of 2.5 nm the $M(H/T)$ curve is a straight line. Deviations from this linear behavior are apparent for the larger particles. For samples with sizes above 2.5 nm, the curves show a component that saturates at about 20 Oe/K and a component almost linear up to 170 Oe/K. These two components can be assigned to the contribution from a bulk like ferrimagnetic core and a shell composed of disordered moments, respectively. Assuming this core-shell model, the contribution of the core to the total magnetization of the particle must be negligible for a particle diameter, D≤2.5 nm. In this framework, the saturation magnetization of the core, M_S, is the relevant parameter to observe the evolution of the core and shell sizes with particles size based on $M(H)$ curves.

In a first approach, M_S can be estimated by a high field extrapolation (Table 5.3). This value can be refined by fitting data to a modified Langevin equation:

$$M = M_S L\left(\frac{\mu H}{k_B T}\right) + \chi H \tag{5.8}$$

where M_S is the saturation magnetization and μ is the average magnetic moment of the core. The linear contribution to the magnetization, χ, is an additional term that is usually used for antiferromagnetic and ferrimagnetic nanoparticles [126, 175]. In antiferromagnetic nanoparticles, such as ferritin, it is usually interpreted as bulk χ_{AF} susceptibility [57–60], which is enhanced in nanoparticles [126]. However, the χ values found here (Table 5.3) are larger than typical values for antiferromagnetic nanoparticles, probably due to the contribution of non-collinear spins in the magnetic structure arising from surface effects [175]. The characteristics of the samples are summarized in Table 5.3.
In Fig. 5.14 differences between data and fits are observed, mainly due to a deficient model for surface. In fact, the surface spins have some saturation in the 20-160 Oe/K range, which is not accounted by the linear term. This small saturation arises since the surface ions are not paramagnetic and/or antiferromagnets, being probably better described as clusters with a magnetic moment much smaller than that of the core but higher than that of isolated paramagnetic Fe ions. Magnetic moment distributions are also contributing to these differences [39]. However, the extracted values of M_S are similar to those estimated from a high-field extrapolation and may serve as a guide to follow the influence of particle size.

5.4.1 Core-shell model

It is evident in Fig. 5.15 that the decrease of M_S is steeper as the particle size decreases. For a size of 3 nm the value approaches to zero and for a size of 2.45 nm the M_S value is

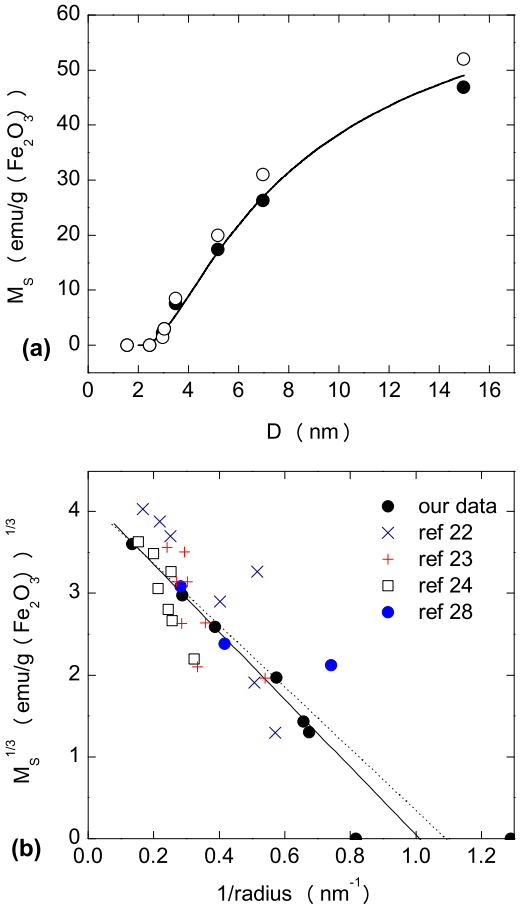

Figure 5.15: (a) Variation of the saturation magnetization, M_S, with the particle diameter. Full points correspond to values from fitting to Eq (5.8) and empty circles correspond to values from high-field extrapolation. The line corresponds to fit to Eq. (5.9); (b) linearization of previous plot, where the constancy of thickness of the magnetically disordered layer d with the particles size can be observed and comparison with data from other authors. The full line corresponds to the fitting of the data here reported and the dashed line to the overall fitting of data included those from other authors.

already zero (Table 5.3). In this core-shell model, M_S is proportional to the volume fraction

of the maghemite-like core

$$M_S = M_{S0}\left(\frac{(D/2)-d}{D/2}\right)^3 \tag{5.9}$$

where M_{S0} should be close to the bulk saturation magnetization (76 emu/g) [176]. The validity of this relation can be confirmed observing a $M_S^{1/3}$ versus $1/(D/2)$ plot (Fig. 5.15b). The results are surprisingly consistent: since this plot is quite linear, we conclude that the disordered layer d is almost constant in a 3-15 nm diameter range.

A linear fit yields a magnetically death shell of thickness $d = 1$ nm and $M_{S0} = 73$ emu/g, which is close to the bulk value and confirms the coherence of this model. We can also observe that the thickness of the disordered layer slightly increases when approaching the limiting size value for total magnetic disorder, since M_S is already zero for sample S2 where $D = 2.5$ nm.

Fig. 5.15b shows also series of M_S data for maghemite nanoparticles from different sources found in the literature [163–166, 171, 177–180]. One by one, these series do not show a clear and consistent tendency. However, the overall tendency is not far from the model proposed in this paper, in spite of a wide scattering. Deviations from the general tendency can be due to particle size dispersion, particle aggregation, interphase interactions and different degrees of crystallization. This could also be caused by uncertainties in the determination of the particle size. In our case, the use of small angle X-ray scattering for size determination has guaranteed statistical representability and no changes in particles due to specimen preparation.

In previous articles, shell thickness has also been estimated from the ratio of canted spins measured by Mössbauer spectroscopy. The shell thickness, d, would be 0.9 nm for $D = 5.9$ nm according to the Coey results [159], 0.5 nm for $D = 9$ nm according to the Hendriksen et al. [147, 148], 0.9 nm for $D = 7.5$ nm according to the Linderoth et al. [162] and 0.35 nm for all the particle sizes in the range 2.7-7.1 nm (at $T = 7$ K). From ZFC-FC measurements, Martinez et al. [158] suggest a spin-glass layer of 0.6 nm for $D = 10$-15 nm. Finally, Lin et al. [152] estimated a thickness of 1.2 nm for cobalt ferrite from polarized neutron experiments. Again, there is a disparity of values, though on average they are not far from the value found in this work. The degree of crystallinity on core and surface can have an important influence on the magnetic properties of maghemite nanoparticles [144, 145]. Actually, it has been proposed that this is the only cause of decrease of magnetization in nanoparticles [181]. This conclusion is based on measurements of saturation magnetization on 7 nm size maghemite nanoparticles that yielded a value (80 emu/g) close to the bulk (76 emu/g). However, values from other authors [177] using a similar synthetic method show a decrease of saturation magnetization that fits well to Eq. (5.9). This disagreement could be partially explained by a presence of magnetite ($M_S = 92$ emu/g) in samples prepared with this method as found in Ref. [182]. Nanoparticle samples used here, showed a high crystalline perfection after annealing as revealed by IR observations. An independent confirmation of our results have been recently reported by Komorida et al. [183] from pressure experiments made in our samples. Comparing structural and magnetic data under pressure the authors arrive at a value of 1 nm.

There are no other experimental evidences on the limiting size at which the core disappears apart from this work. However, according to Monte Carlo simulations by Iglesias and Labarta [184], this should occur for a size around 3 nm. They also announce an increase of the shell thickness as the particle size approaches this value. These predictions are in very good agreement with the results of this work.

5.5 Conclusions

The approach of G. Beaucage can be successfully applied in the analysis of the SAXS intensity of nanocomposites. The average size determined using this method is in agreement with the iron/polymer molar ratio used in the preparation of the nanocomposite. The size dependence of saturation magnetization of a series of nanocomposites, with an average particle size from 3 to 15 nm, follows an analytical function based in the 'core-shell' model. The fit to this function gives a shell thickness of 1 nm value and a saturation magnetization for the ferrimagnetic core close to the bulk value.

Chapter 6

Dipolar interactions in maghemite ferrofluids

Often, the magnetic nanoparticles are close enough such that the dipole-dipole interactions affect the superparamagnetic relaxation, susceptibility and magnetization curves. The interpretation of the results from the experiments is not straightforward and has been a subject of scientific studies during the last decades. One of the studied issues is the possibility of an enhancement of the magnetic relaxation by the dipole-dipole interaction [51, 185]. In an early report, J. L. Dormann [15] showed that magnetic relaxation slowed down as the strength of dipolar interaction increased in a system of iron nanoparticles dispersed in an alumina matrix. Later on, S. Mørup found the opposite trend in a system of maghemite particles embedded in a polymer [49]. In this work, it was stressed that this tendency may be expected in systems where the nanoparticles interact weakly. Some theoretical and numerical models developed afterwards [53, 54, 186] showed that for weak interactions relative to the anisotropy, the energy barriers are no longer governed by interactions and, in fact, decrease with growing interactions. Another interesting issue regarding the effect of dipolar interactions on the magnetic relaxation, is the experimental approach followed to modify the strength of the interactions. Usually, the effect that interparticle interactions have on the relaxation time is analyzed by modifying the particle-particle distance, for example diluting the system, and thus changing the strength of the dipolar interaction. However, this procedure may also modify not only the particle-particle distance but also the distribution of particle size or even, at high concentrations, particles may aggregate into small clusters. Often, it is hard to separate the influence of dipolar interactions on the magnetic relaxation from these other effects.

In this chapter we present results concerning these issues. First, we analyze the dependence of the relaxation time with the nanoparticle concentration in a maghemite ferrofluid where dipolar interactions are very weak and, in fact, are usually negligible. Let us remark that the main difference between Dormann's and S. Mørup's works is that the relaxation time was obtained from magnetization measurements in the former and from Mössbauer experiments in the latter which correspond to different experimental times. Magnetization experiments study the relaxation in a time window from 100 s to 10^{-5} s while Mössbauer from 10^{-7} s to 10^{-9} s. Up to our knowledge, there is no evidence of the effect reported by S. Mørup in experiments based on magnetization measurements. We show that, in our system, the relaxation time obtained from magnetization measurements decreases as the concentration

increases. Second, we propose an experimental procedure to study the influence of dipolar interactions that enables us to switch on and off the interactions. The magnitude of dipolar interactions is modified by orienting the easy axis of the nanoparticles. This feature arises from the anisotropic character of the dipolar interaction. We stress that in this approach we do not modify the number of nearest neighbors neither the distribution of particle size. So that differences between the effective energy barrier of the randomly oriented system and that of the textured system, can be associated only to an increase of the dipolar interactions strength. The effect of the dipolar interactions in ferrofluids by means of magnetically texturing the sample, have already been analyzed by small angle scattering [187, 188]. We prepared a 'magnetically textured' ferrofluid by cooling through the freezing point, under the influence of an external magnetic field. The strength of dipolar interactions is larger in the magnetically textured ferrofluid. In addition, magnetic relaxation becomes slower after the texture process.

6.1 Synthesis

The ferrofluid samples consist of maghemite nanoparticles dispersed in dioctyl ether. In order to study the issue concerning the magnetic relaxation in a weak interaction regime, we prepared a ferrofluid of maghemite nanoparticles with an average size of 12 nm (FF). The magnetic texture procedure was applied to a ferrofluid of maghemite nanoparticles with an average size of 8 nm (TX).

The synthesis of highly crystalline and monodisperse maghemite, γ-Fe_2O_3, nanoparticles was carried out in an organic medium by the Hyeon method [32]. This procedure, which allows varying particle size by controlling the amount of surfactant, is based on the thermal decomposition of iron pentacarbonyl in the presence of oleic acid. In the synthesis of 12 nm iron oxide nanoparticles ferrofluid, a reaction vessel containing 20 mL octylether and 3.41 g of oleic acid is heated under an argon flow to 100 °C. The amount of 0.4 mL of $Fe(CO)_5$ solution is rapidly injected through a septum into the hot vessel containing the dioctyl ether solvent and the oleic acid. This solution was then heated at 282 °C for 1 hour under vigorous stirring. Upon injection, the solution turns black in color and bubbles as $Fe(CO)_5$ decomposes, as the iron nanoparticles are nucleating and the CO gas is releasing. Then, the nanoparticle dispersion was cooled to room temperature. The resulting iron nanoparticles were transformed to monodisperse maghemite by controlled oxidation by using trimethylamine oxide as a mild oxidant. In this process, 0.34 g of $(CH_3)_3NO{\cdot}2H_2O$ were added. The mixture was then heated to 130 °C under argon atmosphere and maintained at this temperature for 2 h. Then, the reaction temperature was slowly increased to reflux and the reflux continued for 1 h. The solution was then cooled to room temperature. The resulting ferrofluid is named FF100. Five additional diluted ferrofluids were prepared by adding dioctyl ether to FF100 in ratios FF100 : octylether were 50:50, 25:75, 12.5:87.5, 5:95, and 2.5:97.5 and were labeled as FF50, FF25, FF12.5, FF5, and FF2.5, respectively, in relation with the decrease in nanoparticle concentration.

The synthesis of 8 nm nanoparticles followed the same chemical route but the amount of oleic acid in the reaction vessel is 2.56 g. The resulting ferrofluid is labeled as TX100. We prepared an additional solution with lower concentration diluting with dioctyl ether TX100. The volume proportions TX100:octylether is 1:8. The sample was labeled as TX8.

6.2 Structural properties

6.2.1 XRD

The crystalline phase of the nanoparticles was identified by recording X-ray powder diffraction patterns of the dried samples. Diffraction patterns were collected with 2θ ranging from 5 to 70°, a step size of 0.03° and a detection time of 1 s. The powder samples were prepared by precipitation with acetone, washing this solvent and then drying at room temperature. The X-ray diffraction patterns of the nanopowders corresponding to samples FF and TX, shown in Fig. 6.1, match well with that of an inverse spinel structure. The broad diffraction peaks are an indication of the small particle size. The diffraction pattern does not present any other peak than those from magnetite/maghemite. The diffractogram from these two phases are very similar in d spacing and intensities and it is therefore difficult to differentiate them only by using XRD. The absence of magnetite was confirmed by titration with $K_2Cr_2O_7$/ferroin that showed no presence of Fe (II).

The particle size was estimated from the broadening of the most intense peak (the (3 1 1) reflection) by using the Debye-Scherrer's equation,

$$D = \frac{0.9\lambda}{\Delta\cos\theta}$$

where λ is the radiation wavelength, Δ is the line broadening measured at half-height and θ is the Bragg angle. θ and Δ were estimated by fitting the peak to a Lorentzian. We obtained the average diameter of 11.2 nm and 7 nm for the FF and TX samples respectively.

6.2.2 Electron microscopy

Transmission electron microscopy observations of the nanoparticles were performed in a Philips CM-30 instrument working at an acceleration voltage of 300 kV. Samples were prepared by putting a drop of the as-prepared maghemite ferrofluid on a carbon-coated copper grid and drying in open air. The image analysis was carried out with a Digital Micrograph software.

The ferrofluids FF100 and TX100 consists of non-aggregated spherical nanoparticles as shown in Fig. 6.2 (a) and (b), respectively, with a distance between the boundaries of nearest neighbor particles ~1.5 nm that corresponds to the surfactant layer thickness. The particle size histograms shown in Fig. 6.2 were obtained by analyzing around 300 particles. From the gaussian fit of the histograms we conclude that the iron oxide nanoparticles have a mean diameter of 11.6±1.0 nm and 8.1±0.98 nm for samples FF100 and TX100, respectively, in agreement with the value obtained from X-ray diffraction data.

6.2.3 DLS

Dynamic light scattering measurements were performed using a Zetasizer NanoZS ZEN3600 from Malvern Instruments [66]. The analysis of the intensity profiles shown in Fig. 6.3, gives hydrodynamic diameters of ~ 13 nm and 11 nm for samples FF100 and TX100 respectively. Using these values and the average diameter determined using TEM we estimate a thickness for the surfactant layer of ~ 1.5 nm, in agreement with TEM images (see Fig. 6.2). The DLS results confirm that there are not large aggregates of nanoparticles at room temperature. Let us notice that the intensity profiles seem wider than expected for a particle size distribution

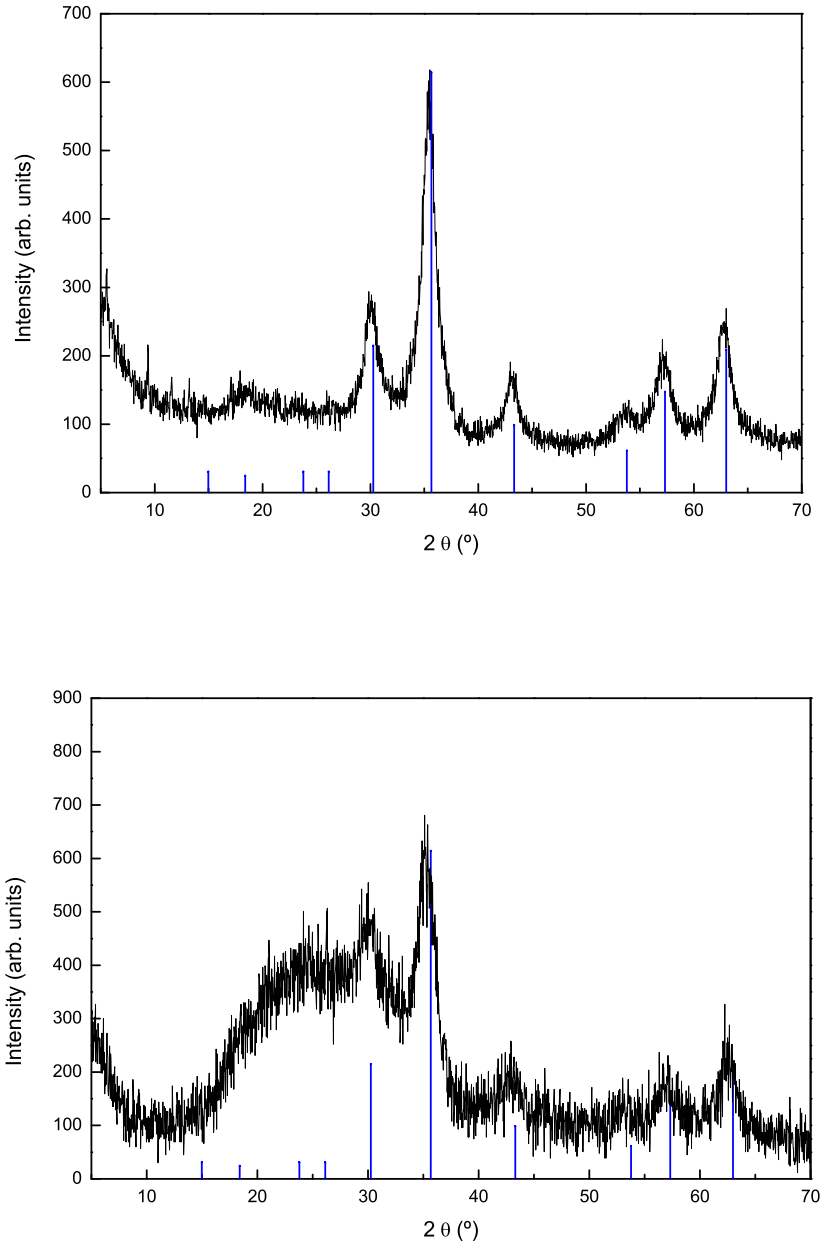

Figure 6.1: XRD patterns of FF (top) and TX (bottom) powder samples. The γ-Fe_2O_3 database reference pattern is also included.

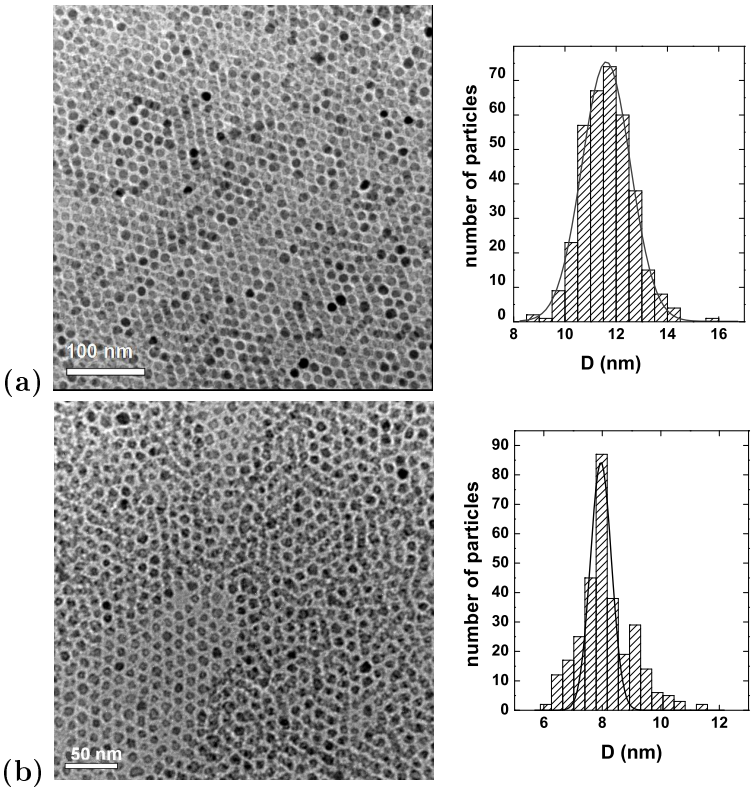

Figure 6.2: TEM images of the ferrofluid FF100 (a) and TX100 **(b)** together with their size distribution profile.

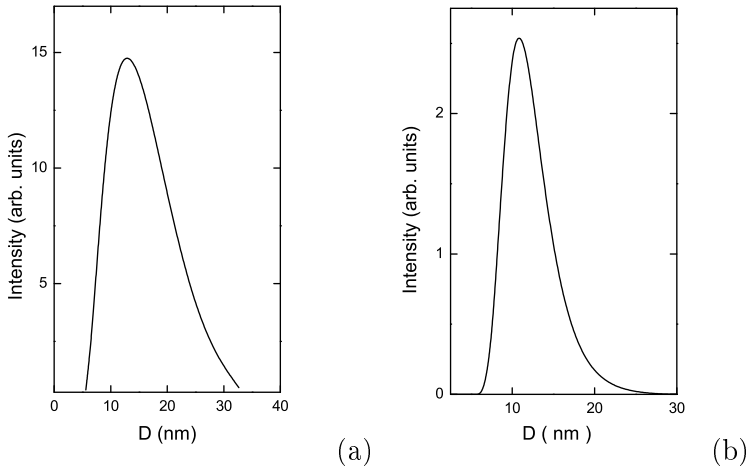

Figure 6.3: DLS intensity profiles of FF (a) and TX (b) ferrofluid samples, measured at room temperature.

with a standard deviation of ~ ± 1 nm. This effect may arise from the fact that the scattering intensity increases with the size, so that the frequency of larger particles is over-valuated.

6.2.4 TGA

The weight percentage of maghemite in the ferrofluids was evaluated by Thermo-gravimetric analysis, using a TGA 5000 apparatus from TA Instruments. The sample was placed in the TGA furnace and heated in nitrogen atmosphere at a rate of 10 °C/min up to 1000 °.

The TGA thermograms of samples FF100 and TX100, shown in Fig. 6.4, are in good agreement with the quantities of the chemical products employed in the synthetic procedure. The weight loss of about 81% and 87% in the temperature range of 100-200 °C are in agreement with the quantity of octyl-ether in the reaction. The second loss of about 10% and 7.5 % corresponds to the oleic acid content. The third loss of weight corresponds to the subproduct of the oxidant. The residual weight accounts for the amount of maghemite, 0.97% and 0.96% for FF100 and TX100, respectively. The resulting concentration are 8.14 and 7.9 mg of iron oxide per mL for FF100 and TX100 ferrofluids respectively.

6.2.5 SAXS

Small angle X-ray scattering experiments were performed to get information about the average particle size and the nanoparticle arrangement in the ferrofluid. Experiments were carried out at the Beam Line 16 (BM16) of the European Synchrotron Radiation Facility (ESRF). The scattered intensity is calculated in absolute units (cm^{-1}) by using a scaling method with water as a reference.

FF ferrofluids

First, the SAXS scattering intensity for the ferrofluid FF100 and the dilutions were analyzed in order to detect the presence of aggregates. The scattering profiles, shown in Fig. 6.5, are constant at low-q indicating the absence of large clusters in these ferrofluids. The extrapolation of the scattering curve to q=0 (I_0) is proportional to N_p/cm^3. $I(0)$ decreases as the concentration is lower, so that the number of particles per unit volume of the sample decreases with concentration, as expected. The scattering intensities show a maximum in the q-region corresponding to the scattering of the average size of the nanoparticles (see below). This maxima show up in similar angular regions for all the dilutions. A closer inspection of Fig. 6.5 reveals that a secondary maximum is observable in the scattering profiles. This feature suggests that these ferrofluids are highly monodisperse.

The volume fraction Φ can be calculated from the Porod invariant [67, 68]

$$Q = \int_0^\infty I(q)q^2dq = 2\pi^2\Phi(1-\Phi)(\Delta\rho)^2 \tag{6.1}$$

where $\Delta\rho$ is the contrast, i.e., the difference of scattering length density between the scattering material and the buffer (see Sec. 2.7). The density is,

$$\rho(cm^{-2}) = \frac{Ne^-}{V_{molecular}} b_T \tag{6.2}$$

where b_T=2.82 × 10^{-13} cm is the Thomson scattering length for an electron. The concentration, determined from the volume fraction, is shown in Table 6.1. The real concentration,

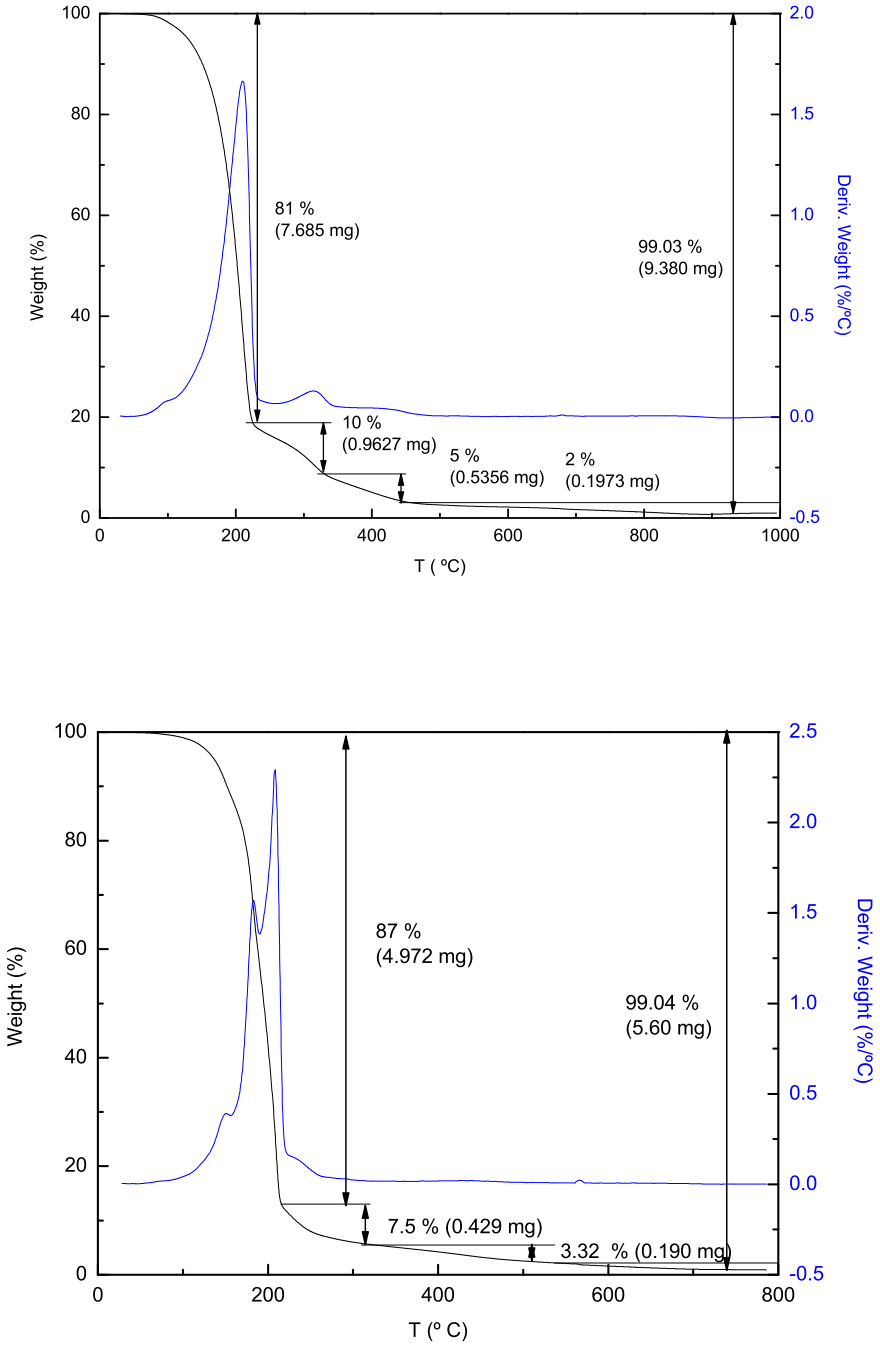

Figure 6.4: TGA thermogram of FF100 (top) and TX100 (bottom) ferrofluid samples show that the amount of maghemite is 0.97 % and 0.96 % respectively.

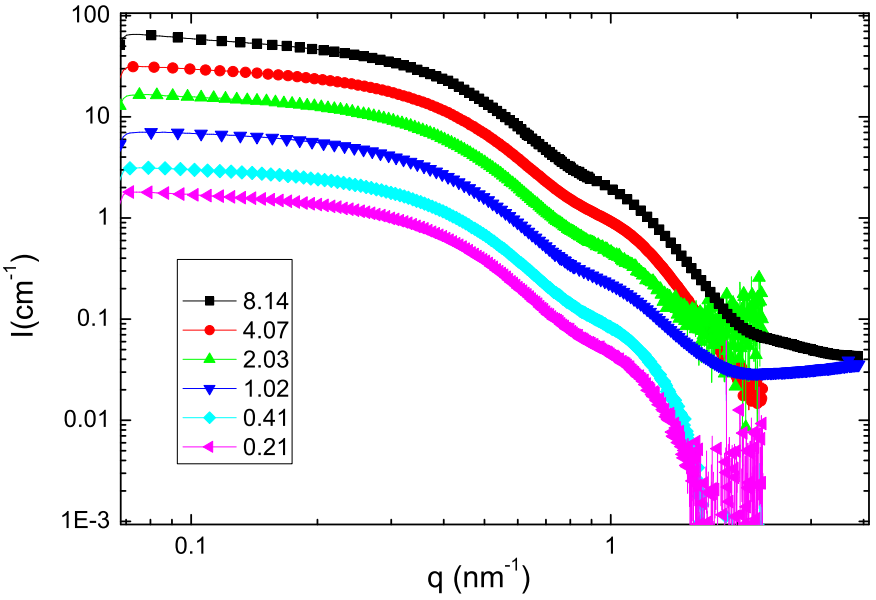

Figure 6.5: Intensity profiles for sample FF100 and dilutions. Concentration shown in the legend is expressed in mg Fe_2O_3 / mL.

calculated from the TGA analysis for the FF100 sample and considering subsequent dilutions, is also included in the table for comparison. The concentrations calculated using Eq. (6.1) are in agreement with the real ones. The actual volume fraction is obtained from Eq. (6.1) only in absence of aggregates. The scattering of clusters is reflected as an additional contribution to the intensity that appears around the angle position corresponding to the average cluster size. In this situation, Eq. (6.1) would give larger Φ values than the real ones. The agreement between calculated and real concentrations and the fact that the intensity profiles are constant at low-q suggest that there is not any aggregate in the ferrofluids.

Additionally, we plotted the normalized concentrations calculated from Eq. (6.1) as a function of the real ones in Fig. 6.6. The existence of aggregates would be reflected in a parabolic trend. From the linear dependence between both normalized concentrations we conclude that there is not any cluster in these ferrofluids, in agreement with DLS results.

The size distribution of sample FF100 was also determined from SAXS measurements and compared to that obtained by TEM. One of the advantages of the size analysis by means of SAXS is that the size distribution is determined from the analysis of a large number of particles. The fit of the intensity profile of the dilution FF12.5, with software GNOM, is shown in Fig. 6.7. The average diameter of 12.8 nm obtained from the fit is comparable to the diameter determined by TEM studies.

We can conclude that the average diameter of 11.6 nm determined by TEM is representative of nanoparticles' size and that the ferrofluid FF100 and its subsequent dilutions do not have any aggregate.

Table 6.1: Middle column is the real concentration, assuming the concentration obtained from TGA for sample FF100. The last column is the concentration calculated using Eq. (6.1).

Sample	gFe_2O_3/mL	gFe_2O_3/mL from Eq. (6.1)
FF100(100:0)	8.14×10^{-3}	8.46×10^{-3}
FF50(50:50)	4.07×10^{-3}	4.25×10^{-3}
FF25(25:75)	2.03×10^{-3}	2.50×10^{-3}
FF12.5(12.5:87.5)	1.02×10^{-3}	1.12×10^{-3}
FF5(5:95)	0.41×10^{-3}	0.53×10^{-3}
FF2.5(2.5:97.5)	0.21×10^{-3}	0.38×10^{-3}

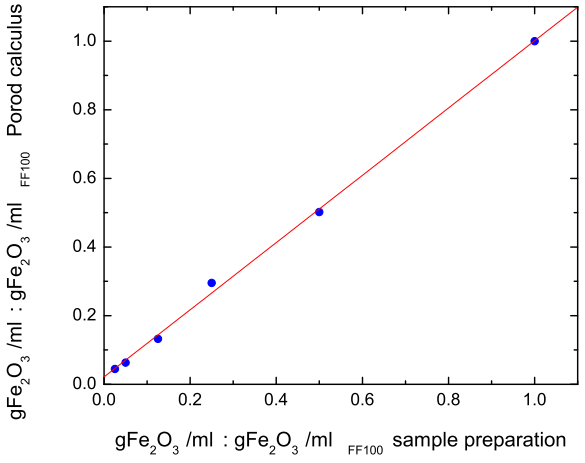

Figure 6.6: Calculated vs real concentration, both normalized to that of the FF100 sample in each case. The solid line is the linear fit.

TX ferrofluids

The SAXS scattering profiles of the TX100 and TX8, displayed in Fig. 6.8 show a constant scattering at low-q, indicating the absence of large aggregates. The extrapolated intensity $I(0)$ shows that the number of particles per unit volume decreases as the concentration decreases. The profiles of both dilutions show a maximum in the same angular region, which corresponds to the scattering of the average particle size. In addition, the secondary maximum is also noticeable, indicating that these ferrofluids are highly monodisperse, in agreement with the distribution obtained by TEM.

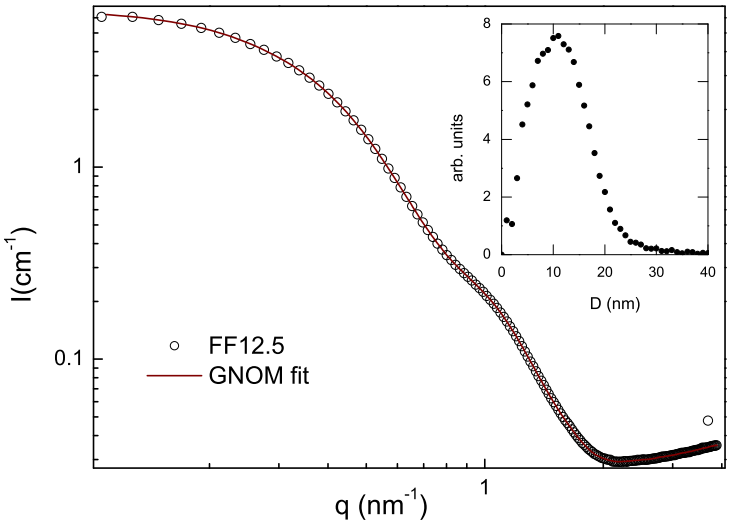

Figure 6.7: Size distribution profile obtained by SAXS. Inset: Scattering intensity for the sample FF12.5. Solid line is the profile fit with GNOM software.

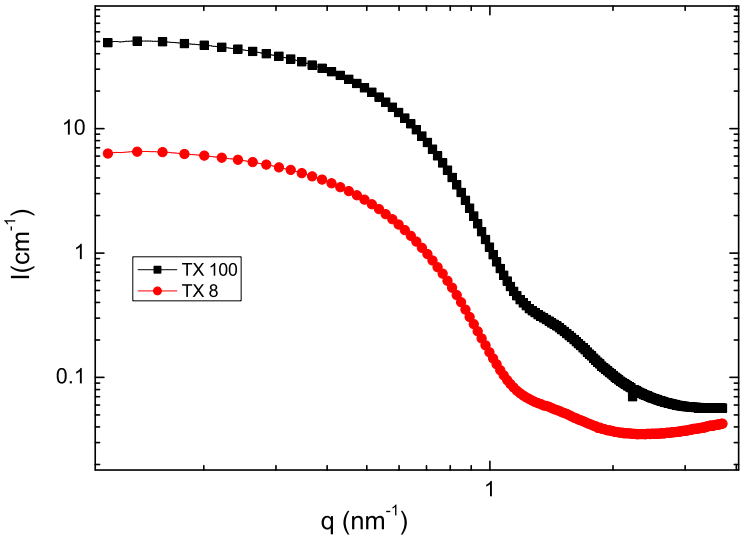

Figure 6.8: Intensity profiles for sample TX100 and TX8.

Table 6.2: The middle column refers to the as prepared concentration. The last column gives the concentration calculated from the Porod invariant.

Sample	gFe_2O_3/mL	gFe_2O_3/mL from Q
TX100(100:0)	7.9×10^{-3}	8.83×10^{-3}
TX8(1:8)	0.88×10^{-3}	1.23×10^{-3}

The concentrations were calculated following the same procedure as in the previous section. They are shown in Table 6.2, together with the concentration calculated from the TGA results. The concentrations calculated from the Porod invariant are in agreement with those determined by TGA, but the former are slightly larger. The agreement between calculated and measured concentrations, as well as the absence of any additional maximum in the SAXS profiles suggest that the ferrofluids are free from aggregation at room temperature, in agreement with the results obtained by DLS.

Now, we determine the size distribution as in the previous section. The fitting of the scattering intensity, shown in Fig. 6.9, gives an average diameter of 8.5 nm, in agreement with the one determined by TEM studies.

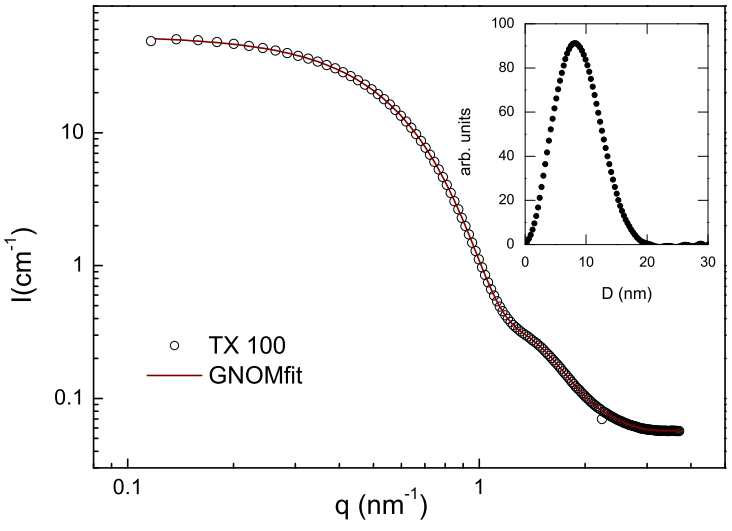

Figure 6.9: Scattering intensity for the sample TX100. Solid line is the profile fit with GNOM software.

We can conclude that the average diameter of 8.1 nm obtained by TEM analysis is representative of the nanoparticles' size.

Finally, the effect of the magnetic texture induced by a 1 T magnetic field on the fluids TX100 and TX8 is analyzed. The intensity profiles at room temperature, in the absence of an applied magnetic field and under the influence of a 1 T field are shown in Fig. 6.10. The scattering intensity under the influence of 1 T field agrees with the one in absence of

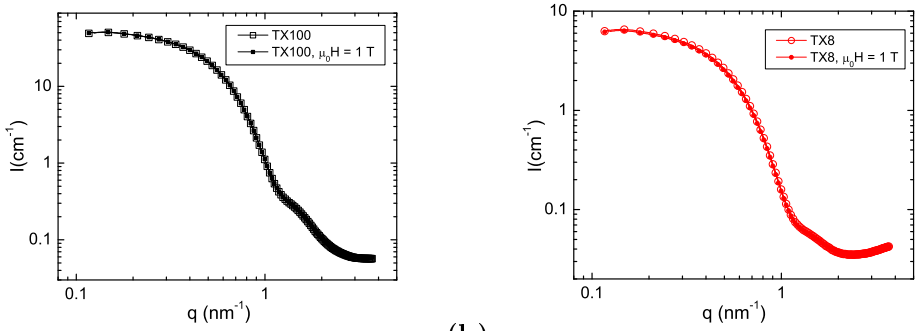

(a) **(b)**

Figure 6.10: SAXS curves for the samples **(a)** TX100 and **(b)** TX8 at room temperature. Filled symbols represent the scattering profiles in the presence of a magnetic field of ~ 1 T. The SAXS intensity in absence of an applied field is also included and represented with open symbols.

magnetic field for samples TX8 and TX100, indicating that the applied field does not induce any aggregation at room temperature. The formation of structures in the fluids is manifested in the scattering curves as a maximum at the characteristic distance of the structure [67]. The absence of this feature and of any additional maxima in the profiles of Fig. 6.10 suggest that in these samples the applied field does not induce any aggregation at room temperature.

6.3 Dipolar interactions at low concentrations

In this section we analyze the influence of dipolar interactions on the magnetic behavior of γ-Fe_2O_3 ferrofluids by means of magnetization and SAR experiments. In particular, we study the dependence of these magnitudes with the nanoparticle concentration. In these studies, we used samples FF100, FF50 and FF25. The magnetic signal of the samples FF12.5, FF5 and FF2.5 was close to the equipment resolution so they were discarded in these studies. The magnetic measurements were performed using a commercial SQUID magnetometer (MPMS-5S, Quantum Design) in the temperature range from 2 K to 325 K and under static magnetic fields up to 5 T. The diamagnetic contributions of the capsule and the buffer were subtracted from all experimental data.

To preserve as much as possible the state of distribution of particles in the carrier liquid at room temperature we have to avoid aggregate formation that may appear in the solidification process. We therefore cooled down the magnetometer to a temperature much lower than the solvent's melting point (T_m ~ 250 K) before the introduction of the fluid samples in order to quench the arrangement of particles in the carrier liquid.

The specific absorption rate was measured at an average temperature of 315 K. To calculate the sample heat capacity, the contributions of the NPs, the carrier liquid, the quartz sample holder and the sealant were taken into account. The temperature increments

measured were small due to the low nanoparticle concentration in the ferrofluid and the relatively high heat capacity, so that final SAR values were obtained by averaging between 5 to 9 heating steps.

6.3.1 Equilibrium properties

Magnetization versus applied field curves measured at 300 K, 250 K, and 180 K are shown in Fig. 6.11. Magnetization curves, in emu per gram of maghemite, were calculated using

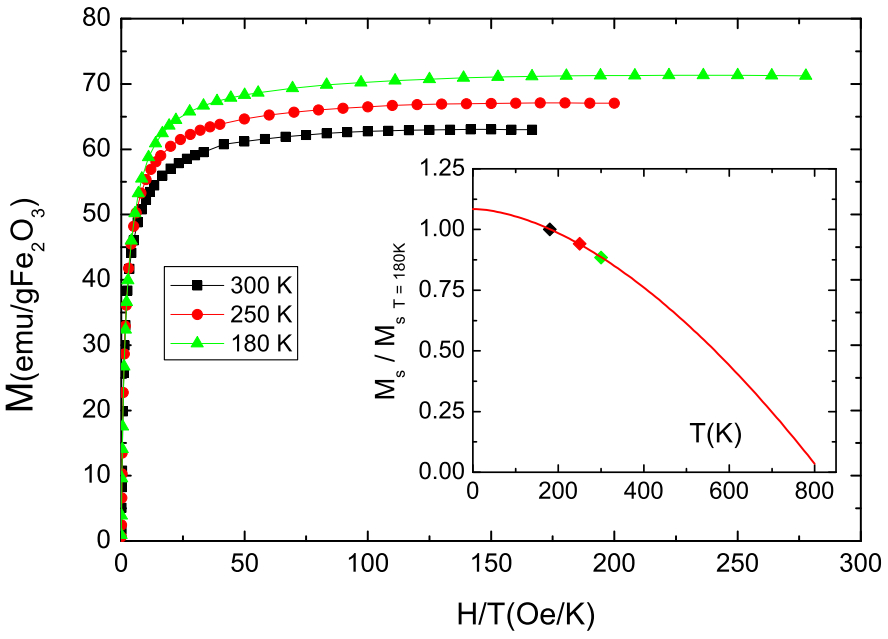

Figure 6.11: dc magnetization curves at room temperature of FF100 sample, at 300 K, 250 K and 180 K. Inset: $M_S/M_{S\ (T=180K)}$; solid line represents the the fitting to the power law expression.

the maghemite concentration obtained by TGA. The dependence $M_S\ (T)$ can be described by a power law [189] $M_S = M_{S\ (T=0)}\ (1 - b\ T^{\alpha}\ )$. The Bloch exponent $\alpha = 1.7$ we obtained is in the range predicted for ultrafine particles ($3/2 < \alpha < 3$), $b = 1.24 \times 10^{-5}$ and $M_{S\ (T=0)}$ = 77.3 emu/gFe_2O_3 (355.58 kA/m) coincides with magnetic saturation for bulk maghemite [18].

The equilibrium susceptibility values, χ_0, have been obtained from the thermal variation of the ac susceptibility, shown in Fig. 6.12. Out-of-phase χ'' susceptibility component vanishes at temperatures larger than 275 K and, correspondingly, in-phase χ' susceptibility component superimposes at the measurement frequencies. These features are also observed for samples FF50 and FF25. Then, above 275 K nanoparticle magnetic moments are super-

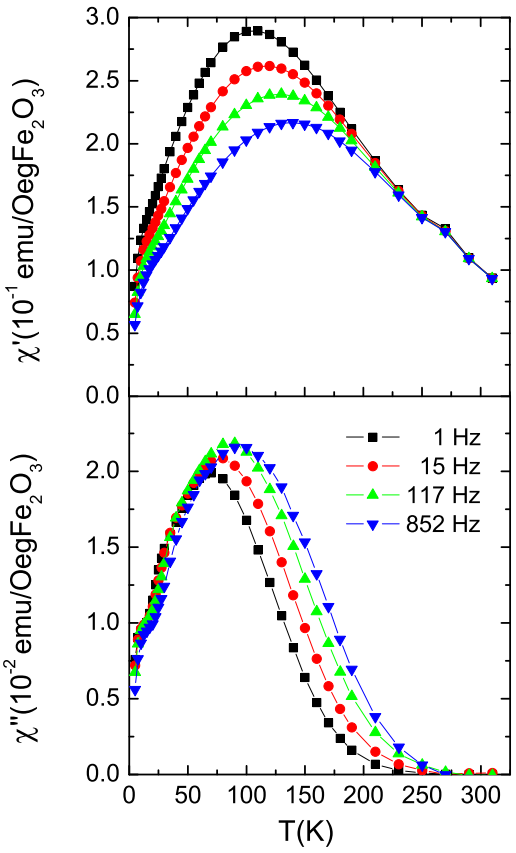

Figure 6.12: ac susceptibility for FF100. At temperatures larger than 275 K out-of-phase susceptibility component vanishes and in-phase susceptibility component superimposes for different frequencies.

paramagnetic and, χ' equals χ_0, the equilibrium susceptibility.

6.3.2 Relaxation

We investigated the dynamics through the analysis of the variation of the relaxation time with temperature. In this analysis, we employed two experimental techniques: ac susceptibility and SAR measurements. The latter explore the relaxation time at room temperature and frequencies of ~ 100 k Hz, while the former examine the range corresponding to temperatures between 4 and 300 K and frequencies between 1 and 852 Hz. Let us point out that, in our particular case, both techniques explore the relaxation in different states of the medium, which is liquid in SAR measurements and frozen in ac measurements.

In ac susceptibility the dynamics are analyzed from the magnetic response as a function of temperature when an alternating magnetic field of frequency f is applied. In particular,

we analyze the variation of the blocking temperature T_B with the relaxation time $\tau = 1/2\pi f$ (see Sec. 1.2.4). In a frozen-medium the particles are not allowed to rotate, so that we are just regarding information about the Néel relaxation time τ_N that we note as τ to abbreviate. The average blocking temperature T_B is the temperature corresponding to the maximum of the out-of-phase component at the measuring frequency f (see Sec. 1.2.4).

Fig. 6.13 shows that $\log_{10}\tau$, obtained from ac susceptibility, is proportional to $1/T_B$. Relaxation time can therefore be described by Néel expression [35] that for an isolated

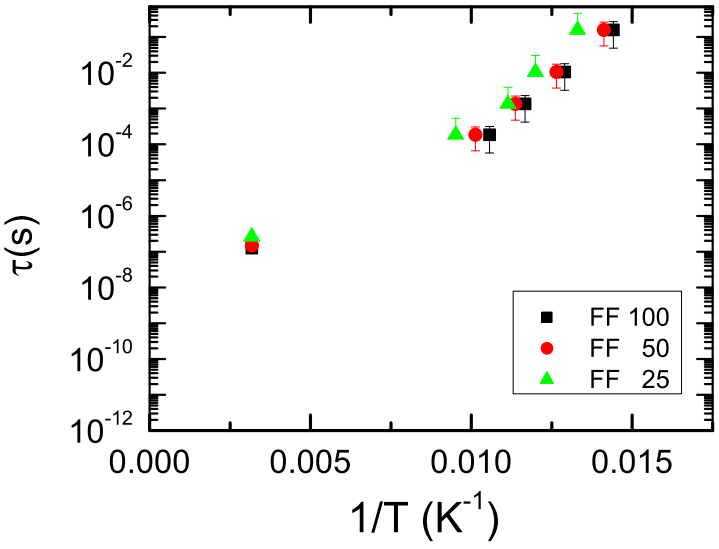

Figure 6.13: Relaxation time versus temperature follows Néel relaxation for the frozen ferrofluid (four points at lower temperatures). In the figure is also included relaxation time determined from SAR.

particle is

$$\tau = \tau_0 \exp(E_b/k_B T) \tag{6.3}$$

where E_b corresponds to the energy barrier. It is interesting to note in Fig. 6.13 that magnetic relaxation is faster for the most concentrated ferrofluid.

The specific absorption rate of the ferrofluids is measured under an oscillating magnetic field of amplitude 3 kA/m and frequency f of 109 kHz. The temperature of the sample is recorded before, during and after field application and the SAR values are calculated as SAR $= (1/m_{NP})\cdot C\cdot(\Delta T/\Delta t)$, where m_{NP} is the mass of magnetic material, C the heat capacity of the whole sample (estimated using the mass, concentration and specific heat capacity of each component) and ΔT the temperature increment during the field application interval Δt. Fig. 6.14 shows three pulses. The left ordinate axis is $(T_s - T_0)\cdot C/m_{NP}$ (J/g), where T_s is the sample temperature, T_0 is the initial temperature trend. This difference is multiplied by the C/m_{NP} ratio, to account for the different ratios. The right ordinate axis shows the field-application interval, with $t = 600$ s in all cases. Let us notice that the original and

diluted ferrofluids come from the same batch so that, in absence of magnetic interactions, the thermal power per unit mass (expressed in watts per gram of magnetic material) should be similar in samples FF25, FF50 and FF100 and so should the increments in Fig. 6.14. However, these increments are higher for the dilutions, about 24% and 134% larger, for samples FF50 and FF25, respectively. This is indicating a decrease of heating power with increasing concentration.

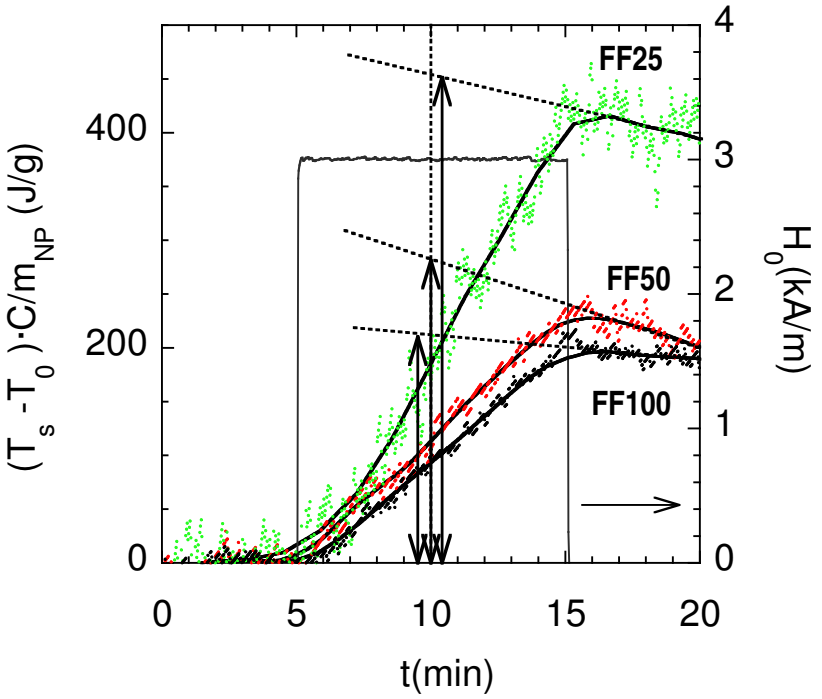

Figure 6.14: Heating steps at $f = 109$ kHz: experimental data with smooth fit. The dotted lines are the extrapolation of the T drifts after ac-field application. The double arrowhead lines stand for the $\Delta T \cdot \mathrm{C}/m_{\mathrm{NP}}$ values.

We determined the relaxation time from SAR values. According to R. E. Rosensweig [79] SAR can be expressed as:

$$SAR(\mathrm{W/g}) = \mu_0 \pi f H_0^2 \chi''/\rho \quad \text{with} \quad \chi'' = \chi_0 \frac{\omega\tau_{\mathrm{eff}}}{1+(\omega\tau_{\mathrm{eff}})^2} \tag{6.4}$$

where ρ is the mass density of maghemite, χ_0 is the equilibrium susceptibility, $\omega = 2\pi f$ and τ_{eff} is the effective relaxation time of the particles. The equilibrium susceptibility χ_0 at 315 K is obtained from the extrapolation of χ' at the superparamagnetic regime. At temperatures $T = 315$ K the ferrofluid is in the liquid state so that relaxation result through two processes: brownian and/or Néel mechanisms. Both contribute to the relaxation with an effective relaxation time

$$\frac{1}{\tau_{\mathrm{eff}}} = \frac{1}{\tau} + \frac{1}{\tau_{\mathrm{B}}} \tag{6.5}$$

where τ_{B} is the time associated with the rotational diffusion and τ is the time associated with the magnetic relaxation, mentioned previously. The Brownian relaxation time for spherical

Table 6.3: Relaxation times at 315 K, calculated by using SAR measurements.

Sample	τ_{eff} (s)	τ (s)
FF100	1.27×10^{-7}	1.32×10^{-7}
FF50	1.50×10^{-7}	1.57×10^{-7}
FF25	2.61×10^{-7}	2.83×10^{-7}

particles is given by the expression

$$\tau_{\text{B}} = (3V_{\text{H}}\eta)/\text{k}_{\text{B}}T \tag{6.6}$$

where η ~3.52 mPa·s is the viscosity for the octylether and V_{H} is the average hydrodynamic particle volume. Assuming that $V_{\text{H}} \simeq 1.2V$ where V is the average volume determined by TEM, we obtain τ_{B} =3.43 $\times$ 10^{-6} s. Neglecting the variation of viscosity with ferrofluid concentration, due to the low concentration values, this τ_{B} is the same for the three ferrofluids considered. Néel relaxation times can then be deduced and are collected in Table 6.3. The τ values determined from SAR are also depicted in Fig. 6.13. We notice that the magnetic relaxation is faster as concentration increases, in agreement with the results from the magnetic measurements of the frozen ferrofluids. In addition, it can be observed that τ values are 10 times lower than the τ_{B}, so that Néel relaxation is the dominant mechanism, because it is much faster. Then, $\tau_{\text{eff}} \simeq \tau$, that we will note in subsequent sections as τ to abbreviate.

6.3.3 Analysis

The effects observed in the previous sections could be due to the existence of aggregates in FF100 that have progressively disappeared when we have diluted the fluid. However, dynamic light scattering measurements provide an hydrodynamic size of the order of that obtained by TEM. This fact discards the existence of large aggregates. Also, due to its low concentration value, sample FF100 is not likely to contain such aggregates. Another possible explanation is the presence of dipolar interactions in the original fluid FF100: the dipolar interactions become weaker as the fluid becomes more diluted and the nanoparticle magnetic moments readily follow the applied field.

In order to better understand and to correlate the results obtained in the liquid and frozen states, we have compared our experimental data with some theoretical results about magnetic systems displaying dipolar interactions. At this point we compare the volume concentration, c_v, of our samples with those used in other works on dipolar interactions in ferrofluids [49, 50]. For FF100, FF50 and FF25 we have $c_v \approx 0.18\%$, $c_v \approx 0.10\%$ and $c_v \approx 0.04\%$, respectively. The low concentrations of our ferrofluids leads to large interparticle distances such that models based on spin-glass behaviors, characteristics of strong interacting systems, are far from being adequate in this analysis. The interaction effect usually attributed to these concentrations is negligible. For example, using the model proposed by S. Mørup and E. Tronc [49] for weak interactions, the change in T_{B} due to interactions in the FF100 sample would be ~5×10^{-3} %, which is inappreciable. However, it is very difficult indeed to avoid interactions completely.

The models usually applied to analyze the influence of dipolar interactions are described in Sec. 1.2.5. The Dormann-Bessais-Fiorani model (DBF) [51] differentiate two regimes of medium and weak interactions according to the value of the factor $[a_1 M_S^2 V/k_B T]$, where $a_1 \sim c_v/\sqrt{2}$. This factor for the FF100 takes values between 0.014 and 0.003 in the considered temperature range, so that the samples of this work lie in the weak interacting regime. Fig. 6.15 shows the fit of the relaxation time with the expression proposed by the DBF model. In the fitting we used the dependence of the magnetization with temperature calculated

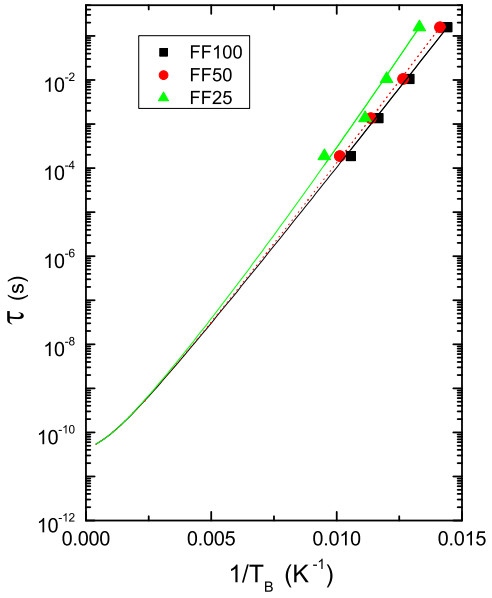

Figure 6.15: Relaxation times versus inverse blocking temperature and corresponding fits to the DBF model.

in Sec. 6.3.1 and the average particle volume from TEM analysis. We assume that the mean number of first neighbors is 12 (average close packing) for the three dilutions. With those parameters fixed, from the fitting we deduce the anisotropy barrier of the single-particle, E_{b0} = 1705 ± 100 K, η_r=0.9 ± 0.01 and the interaction energies $E_{i,FF100}$ = 8×10^{-4} ± 0.01 K, $E_{i,FF50}$ = 25.7 ± 0.5 K, $E_{i,FF25}$ = 53.9 ± 0.7 K. The value of η_r is in the range expected for interacting nanoparticles [50]. Besides, the value of E_{b0} is in agreement with the magnitude for the anisotropy energy of γ - Fe_2O_3. We first notice in Fig. 6.15 that the slope is larger as the ferrofluids become more diluted. In fact, the relaxation time is faster as the ferrofluid is more concentrated. This is in agreement with the dependence with concentration of the values determined from the fit for E_i. However, this means that the dipolar interaction increases when the particles become more separated, that is unreasonable. In this model, the expression for the total energy barrier E_b predicts an increase of this magnitude with increasing concentration. So that an increase of the relaxation time with increasing interactions strength is predicted. However in Fig. 6.13 we clearly show that the trend of the relaxation time is just the opposite for both the frozen and liquid state: it is faster for the concentrated samples. So the assumptions made within this model seem not

to be adequate to describe our results.

The Mørup-Hansen-Tronc model (MHT) was developed to describe the magnetic relaxation in weak interacting systems. In fact, it requires that

$$\sqrt{2}\left(\frac{\mu_0}{4\pi}\right)\frac{\mu^2}{d^3} \ll 2E_{b0} \tag{6.7}$$

where E_{b0} is the single-particle energy barrier, μ is the mean magnetic moment and d is the average distance between the neighboring particles. This condition is fully satisfied in the samples studied in this work where E_{b0} ~1800 K for γ-Fe_2O_3 and $\sqrt{2}\left(\frac{\mu_0}{4\pi}\right)\frac{\mu^2}{d^3}$ ~ 2.5 K for the most concentrated sample FF100. We fit the relaxation time with the expression

$$\tau = \tau_0 \exp[\alpha - (1/3)\beta_{av}^2(1 - 3/4\alpha^{-1})]$$

where $\alpha = E_{b0}/\ k_B T$ and $\beta_{av}^2 = 2[(\mu_0/4\pi)^2\mu^4 \sum d_{nn}^{-6}]/(k_B T)^2$. The best fit of the data with this expression provides values for the pre-exponential factor ~ 10^{-13} s, much lower than τ_0. So that we assumed that τ_0 depends with temperature following the expression [37]

$$\tau_0 = \tau_D \frac{\sqrt{\pi}}{2}\left(E_b/k_B T\right)^{-3/2} \tag{6.8}$$

where τ_D is the relaxation time of isotropic spins, and E_b is the energy barrier. From the fit, shown in Fig. 6.16, we deduce E_{b0} ~ 1830 ± 200 K, in agreement with the magnitude for the anisotropy energy of γ - Fe_2O_3. The dipolar energies determined from the fit $E_{i,FF100}$

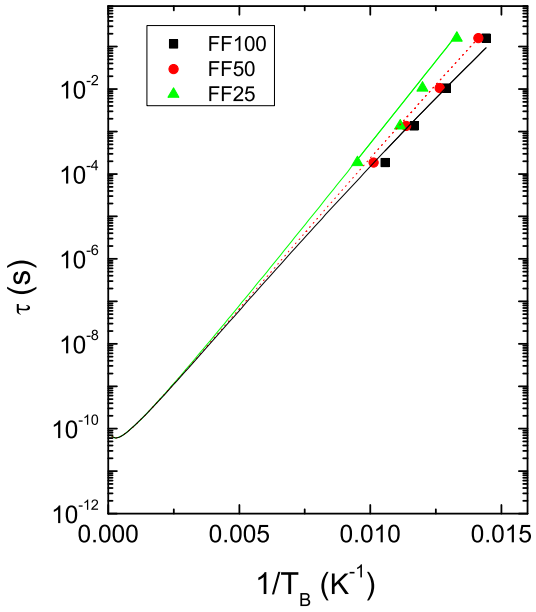

Figure 6.16: Relaxation times versus inverse blocking temperature and corresponding fits to the MHT model.

= 207 ± 5 K, $E_{i,FF50}$ = 165 ± 13 K, $E_{i,FF25}$ = 7 × 10^{-7} ± 3 × 10^{-10} K increase with

the volume concentration as expected when the distance between neighboring nanoparticles become smaller. However, the magnitude of the dipolar energies obtained from the fit are much larger than the value calculated by using the distance between particles determined by TGA, $E_{\mathrm{i,FF100}}$ = 24.8 - 49.6 K, $E_{\mathrm{i,FF50}}$ = 16.6 - 33.23 K , $E_{\mathrm{i,FF25}}$ = 6.3 - 12.7 K. We conclude that although the MHT model qualitatively describes the dependence of relaxation time with concentration, the magnitude of the fitting parameters derived is not real.

The model of P. E. Jönsson, J. L. García-Palacios, M. F. Hansen and P. Nordblad (JGP) [52] is valid at very weak interaction strengths. The dipolar interaction energy for the FF100 sample is $\mu_0\mu^2/4\pi a^3 k_{\mathrm{B}}$=1.75 K, so that the model might be applied in the entire temperature range. Fig. 6.17 shows the fits of the experimental relaxation time to the expression we mentioned in Sec. 1.2.5, $\tau_{\mathrm{m}} = \tau_0 e^{\sigma} g(\lambda, \sigma, d)$. We obtained $E_{\mathrm{b0}} \sim$ 1772 K, in

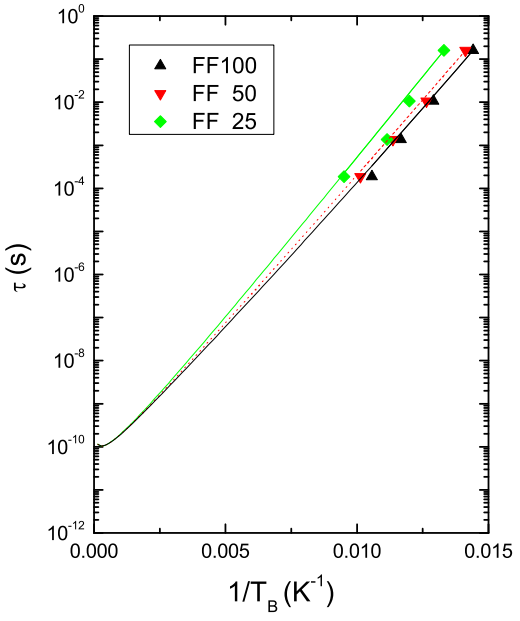

Figure 6.17: Relaxation times versus inverse blocking temperature and corresponding fits to the JGP model.

the range of the anisotropy energy value expected for γ-Fe_2O_3. We calculated from $\xi_{\mathrm{d}}T$ the concentration that might induce this interaction energy. It is two orders of magnitude larger than the experimental concentration. So that once again the model qualitatively describes the dependence of the relaxation time with the concentration but, the magnitudes determined are not acceptable.

Therefore none of the previous models give an analytical expression that provides reasonable physical parameters for our data, though MHT and JGP can describe them qualitatively.

We finally considered the model of D. V. Berkov and N. L. Gorn [53]. The value of the parameter β = 2 K / M_{S} in this ferrofluids is calculated with the anisotropy constant determined from the Néel relaxation time fit (1800 K) and the saturation magnetization from

dc magnetization measurements 355 emu/cm^3. This gives $\beta = 4.2 \geq 1$ that corresponds to the range of moderate and large anisotropies. Both features assigned to this regime are observed in Fig. 6.18: first, the peak in the $\chi''(T)$ shifts towards lower temperatures when increasing particle concentration; second, the out of phase susceptibility component also display non-monotonic dependence of the peak height on the particle concentration. The peak height of

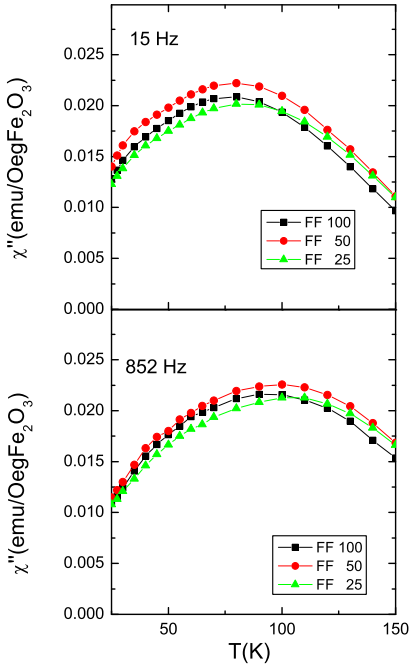

Figure 6.18: Out-of-phase susceptibility at two frequencies for the three dilutions.

$\chi''(T)$ increases from the FF25 to the FF50 ferrofluid and then it decreases again for FF100. The effect is small, in agreement with numerical simulations results. We also compared the peak height of $\chi''(T)$ for various frequencies. The corresponding numerical simulations for β= 2 in Ref. [53] show that when increasing frequencies the peak position is shifted to higher temperatures and the peak height decreases. In Fig. 6.12 we clearly observe that for FF100 the peak shifts also to higher frequencies and the peak height increases up to 117 Hz and decrease at 852 Hz. Such a change can be understood taking into consideration that the frequencies used in the numerical calculations of Ref. [53] are much larger than those we used in ac susceptibility measurements. So that only the diminishing in peak height is observed. This dependence of the peak height confirms that our system is in the moderate and large anisotropy regime in which interparticle interaction is not strong enough to govern the energy barriers. Let us notice that this model describes not only the dependence of the relaxation time with concentration for our samples but also the diminishing to the peak height at high frequencies.

6.4 Texture-induced magnetic interactions

The magnetic measurements were performed using a commercial SQUID magnetometer (MPMS-XL, Quantum Design) in the temperature range from 2 K up to 325 K and under magnetic fields up to 5 T. All the measurements were performed with the ferrofluid enclosed in a gelatin capsule. The diamagnetic contributions of the capsule and the buffer have been measured separately. They depend linearly with the applied field and are temperature independent. These diamagnetic contributions were subtracted from all experimental data.

The melting point of the solvent (T_m) is around 250 K. In order to vary the magnetic texture, we performed experiments using two different cooling down protocols depicted in Fig. 6.19. In the first, protocol 1, the sample was cooled down to the lowest temperature (1.8

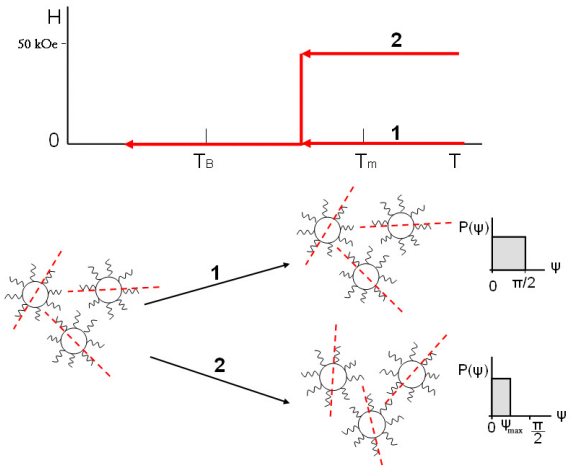

Figure 6.19: Experimental protocols employed to control the magnetic texture. Protocol 1: the sample is cooled down to 1.8 K under no applied field; the easy axes of the nanoparticles stay randomly oriented. Protocol 2: the sample is frozen to 110 K under a magnetic field of 50 kOe; it is subsequently cooled to 1.8 K (crossing T_B) under no applied field. The angle between the easy axis and the measuring field ψ range from zero to ψ_{max}, where ψ_{max} is zero for a perfect alignment and $\pi/2$ for a randomly oriented easy axis.

K) under no applied field (sample RDM). After this process the easy axes of the nanoparticles stay randomly oriented and the angle between the easy axis and the measuring field ψ can have any value between zero and $\pi/2$. The fraction of particles with the easy axes making angle $\psi(\pm d\psi)$ with the direction of the measuring field is $P(\psi)\sin\psi d\psi$, where the orientational distribution of easy axes $P(\psi)=1$, $0 \leq \psi \leq \pi/2$. In the second, protocol 2, the nanoparticles are subject to a magnetic field of 5 T when they are cooled down from 280 K to 110 K, i.e. crossing the melting point (sample TXT). Notice that since $T_m >> T_B$ (the largest blocking temperature is of the order of 100 K, see below) the two protocols are ZFC processes with respect to the blocking of the magnetic moments. The same qualitative behavior is observed for TX100 and TX8 ferrofluids after the texture process but the magnetic texture achieved in TX8 is larger, so that we only present the results obtained for the TX8 ferrofluid.

After process 2, the nanoparticles easy axes are expected to become closer to the direction of the texturing field, parallel to the measuring field. As a simple approximation, we model this effect with a narrower flat distribution function

$$\mathrm{P}(\psi) = \begin{cases} 1, & 0 \leq \psi \leq \psi_{\max} \\ 0, & \psi \geq \psi_{\max} \end{cases} \tag{6.9}$$

which ψ can have any value between zero and $\psi_{\max}$. For a perfect alignment of the easy axes with the texturing field, $\psi_{\max}$ would be zero. As a first approximation we consider that ψ is homogeneously distributed between zero and $\psi_{\max}$ (see Fig. 6.19).

6.4.1 Effect of texture on the equilibrium properties

First, we analyze the equilibrium magnetic properties to estimate the degree of magnetic texture acquired following protocol 2. The effect of the cooling protocol on the magnetic texture can be asserted by the remanence and coercivity of the hysteresis loops measured at $T << T_{\mathrm{B}}$ under magnetic fields up to 5 T. We estimated the demagnetizing effect on the shape of the hysteresis loop and it can safely be neglected.

Fig. 6.20 shows that the area of the hysteresis loop measured at $T = 2$ K in sample TXT is slightly larger than the one obtained following the protocol 1. This feature suggests that

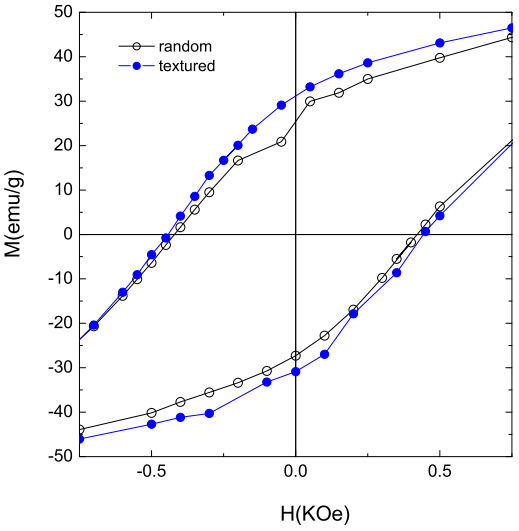

Figure 6.20: Hysteresis loop for the protocol 1 (∘) and protocol 2 (•) samples at $T = 2$ K. The area increases after the protocol 2.

protocol 2 introduces a partial alignment of the easy axes with respect to the direction of the freezing field. In agreement with this, the remanent magnetization M_{r} increases slightly, by about 15%, after protocol 2.

The degree of magnetic texture was obtained from the remanent magnetization which can be written as [190]

$$M_{\mathrm{r}} \simeq \langle \cos\psi \rangle \, M_{\mathrm{S}} \tag{6.10}$$

where M_S is the saturation magnetization and $\langle \cos\psi \rangle$ is given by

$$\langle \cos\psi \rangle = \int_0^{\pi/2} \cos\psi \; P(\psi) \sin\psi \; d\psi = \frac{1 - \cos 2\psi_{max}}{4(1 - \cos\psi_{max})} \tag{6.11}$$

Inserting in Eq. (6.10) M_r and M_S of sample RDM we obtain $\langle \cos\psi_{RDM} \rangle$=0.45. This value is slightly smaller than the expected at $T = 0$ for a sample with the easy axes randomly oriented, $\langle \cos\psi \rangle$=0.5, since the hysteresis loops were measured at $T = 2$ K. In order to avoid this experimental difficulty, $\langle \cos\psi_{TXT} \rangle$ is determined from the ratio between the remanent magnetization of sample TXT and that of sample RDM. Considering that saturation magnetization of sample TXT is the same as that of sample RDM one can write

$$\frac{M_{r\ RDM}}{M_{r\ TXT}} = \frac{\langle \cos\psi_{RDM} \rangle}{\langle \cos\psi_{TXT} \rangle} \tag{6.12}$$

Inserting in Eq. (6.12) the experimental values for remanent magnetizations, and using $\langle \cos\psi_{RDM} \rangle = 0.5$, gives $\langle \cos\psi_{TXT} \rangle = 0.575 \pm 0.005$, which corresponds to $\psi_{max} = 81 \pm 1$ °.

The texture effect on the magnetic behavior is also reflected in the equilibrium magnetization curves [191, 192]. It is interesting to note in Fig. 6.21 that the ferrofluid magnetizes

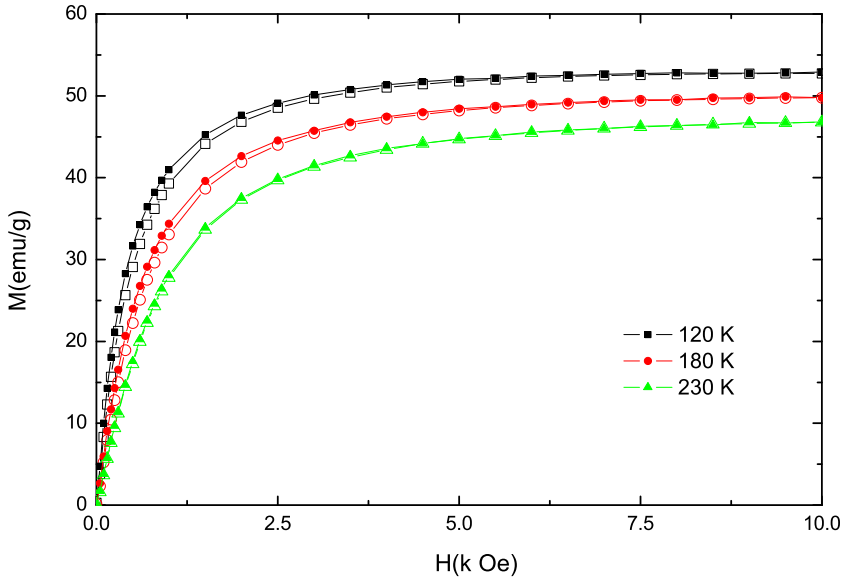

Figure 6.21: Equilibrium magnetization measured at different temperatures for the two cooling down protocols: solid symbols correspond to sample TXT; open symbols to RDM.

faster (i.e. at lower fields) after the texture process. This suggests that the process has induced a certain degree of orientational order on the easy axes. Above the solvent freezing temperature $T = 230$ K, the differences in equilibrium magnetization tend to vanish and magnetization curves measured following the two protocols superimpose. We notice that

magnetization M is not a function of H/T, which is in agreement with the temperature dependence we found for the magnetic moment determined by susceptibility measurements.

The effect of the magnetic cooling protocol on the magnetic texture is evidenced also by the equilibrium susceptibility [193]. The in-phase susceptibility above the blocking temperature and below the melting point is larger for the protocol 2 than for the protocol 1, as shown in Fig. 6.22, so that the effect of texture is to increase the equilibrium susceptibility [193]. Notice from Fig. 6.22 that equilibrium susceptibility data of sample TXT agrees with

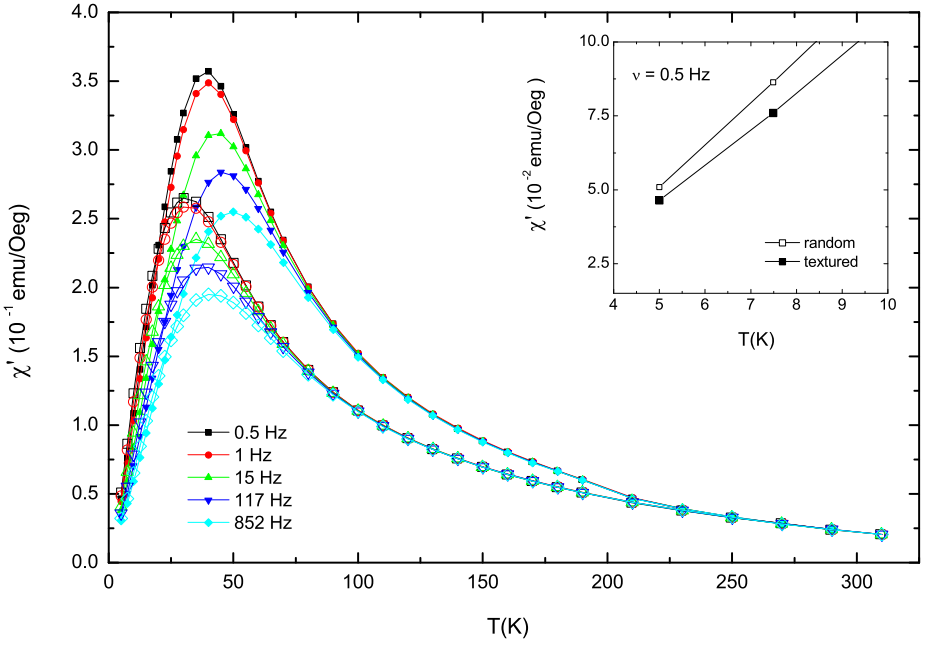

Figure 6.22: In-phase susceptibility at different frequencies: solid symbols correspond to sample TXT; open symbols to sample RDM. Notice that the equilibrium susceptibility is larger for the textured sample; at the melting point of the solvent ~ 250 K the curves obtained after the two protocols superimpose. Inset: low temperature magnification.

the data of sample RDM at the melting point of the solvent, indicating that the texture process is reversible.

The degree of magnetic texture was also estimated from the in-phase susceptibility at low temperatures. At $T \to 0$ the expression Eq. (1.22) reduces to

$$\chi' \simeq \langle \sin^2\psi \rangle \, \chi_\perp \tag{6.13}$$

where

$$\langle \sin^2\psi \rangle = \int_0^{\pi/2} \sin^3\psi \; \mathrm{P}(\psi) \; d\psi = \frac{2 + \cos^3\psi_{\max} - \cos\psi_{\max}}{3\,(1 - \cos\psi_{\max})} \tag{6.14}$$

and $\chi_\perp = \frac{M_S}{H_{AN}}$ (see Sec. 1.2.4) is the susceptibility perpendicular to the easy axis, being H_{AN} the anisotropy field. The value for $\chi_\perp \simeq 7.64 \times 10^{-2}$ emu/Oeg is estimated using the in-phase susceptibility data of sample RDM, assuming that the easy axes are randomly oriented, so $\langle \sin^2\psi \rangle_{RDM} = 2/3$. Inserting this value of $\chi_\perp$ in Eq. (6.13) we obtain $\langle \sin^2\psi \rangle_{TXT} = 0.608 \pm 0.001$, giving $\psi_{max} = 81.2 \pm 0.2$ °, in agreement with the value determined from remanence data.

Notice that the equilibrium susceptibility,

$$\chi_T \simeq \langle \cos^2\psi \rangle \chi_\parallel \tag{6.15}$$

where $\chi_\parallel$ is the susceptibility along the anisotropy axis,

$$\chi_\parallel \simeq \frac{C_\parallel}{k_B (T - \theta)} \tag{6.16}$$

also provides information about the degree of texture (through $\langle \cos^2\psi \rangle$) but is also influenced by the dipolar interactions (through θ).

The information about the texture determined through remanence and susceptibility has been compared with the values calculated with the expressions provided in Ref. [190]. The average value of $\cos\psi$ in a fluid dispersion of nanoparticles with magnetic moment μ and anisotropy energy KV, in the presence of a magnetic field H, is given by

$$\langle \cos^2\psi \rangle \simeq \mathcal{L}(\beta) \left(1 - \frac{1}{2\sigma}\right) \tag{6.17}$$

where $\sigma = KV/k_B T$, $\beta = \mu H/k_B T$, and $\mathcal{L}(\beta)$ is the Langevin function. On cooling the sample through its freezing point T_m it retains the texture characteristic of the fluid at T_m, characterized by $\beta = \mu H/k_B T_m$ and $\sigma = KV/k_B T_m$. The anisotropy energy $KV = 485$ K was determined from the out-of-phase susceptibility data of sample RDM following the method described in Ref. [47]. The average magnetic moment at T_m, $\mu = 7420.1\ \mu_B$, was obtained from the in-phase susceptibility data of sample RDM. Inserting these values in Eq. (6.17) gives $\langle \cos\psi \rangle \simeq 0.73$ which corresponds to $\psi_{max} = 63$ °. The degree of texture expected from these calculations is larger than that obtained from remanence and susceptibility data. The magnetic texture in a fluid dispersion of nanoparticles depends on the coupling between the magnetic moment and the easy axis of the particle. The discrepancy between the calculated and the experimental degree of texture can be explained considering a weaker anisotropy energy, probably due to the fact that the anisotropy constant K decreases as the temperature increases. Regardless this discrepancy we can conclude, from remanence and susceptibility data, that the sample becomes magnetically textured after procedure 2.

6.4.2 Magnetic interactions

We next discuss if the texture has any influence on the strength of magnetic interactions. In order to do that, we compare the equilibrium susceptibility χ_T of RDM and TXT samples, as χ_T is influenced by the dipolar interactions [56].

One of the approaches to model this effect is to assume that χ_T can be represented, above the blocking temperature, by the Curie-Weiss law Eq. (6.16), where the magnitude of θ is considered to reflect the strength of the interactions and the sign its type ($\theta > 0$, ferromagnetic; $\theta < 0$, antiferromagnetic) [56]. θ is usually obtained as the extrapolation of the reciprocal susceptibility. El-Hilo et al. [56] analyzed the use of Eq. [56] and concluded that magnetic relaxation influences θ. This effect is reflected in the reciprocal susceptibility in which a linear dependence of $1/\chi_T$ with the temperature is not clearly shown, being more

noticeable as T approaches T_B. For this reason the temperature range selected to apply the Curie-Weiss law was chosen well above T_B and below the melting point of the solvent.

Fig. 6.23 displays the reciprocal susceptibility data of RDM and TXT samples. From 5

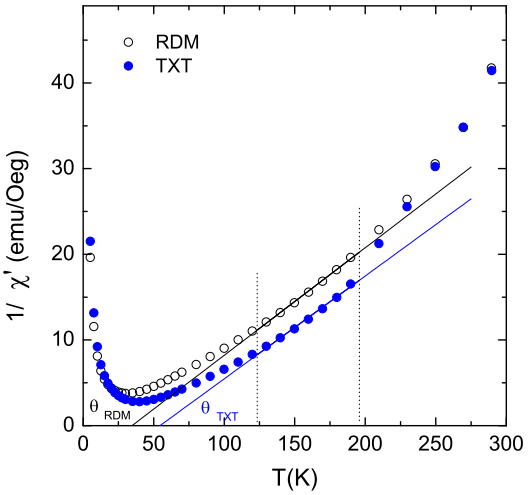

Figure 6.23: Reciprocal ac susceptibility: solid symbols, TXT; open symbols, RDM.

to 75 K the susceptibility shows the superparamagnetic blocking for both samples, as already shown in Fig. 6.22. Above 125 K and below the melting point of the solvent χ_T follows the Curie-Weiss law giving $\theta_{\mathrm{RDM}} = 34.6 \pm 2.6$ K and $\theta_{\mathrm{TXT}} = 54.4 \pm 3.6$ K for RDM and TXT samples, respectively. The reciprocal susceptibility data of sample TXT extrapolates to a larger value of θ which supports the interpretation that the interaction strength has increased after protocol 2. Notice that at the melting point of the solvent ~ 250 K the curves obtained after the two protocols agree with each other.

This result is in agreement with the success obtained in the texturing process, considering the anisotropic character of the dipolar interaction. Protocol 2 introduced a partial alignment of the easy axis towards the freezing field direction thereby narrowing the distribution of magnetic moment's direction. After protocol 2, the direction of the particle's magnetic moment becomes closer to its nearest neighbor one, increasing the strength of dipolar interaction. We can conclude that the texturing process is able to change the magnitude of the dipolar interactions by orienting the easy axes of the nanoparticles.

6.4.3 Magnetic relaxation

In previous sections we have shown that using the magnetic texture procedure, protocol 2, we are able to increase the strength of dipolar interactions in the sample. We can now attempt to explore how the texture, and the induced magnetic interactions, modify the magnetic relaxation process.

The out-of-phase susceptibility data (see Fig. 6.24) shows evidence for a superparamagnetic blocking at a temperature ~ 20 K. It is obvious from this figure that the magnetic

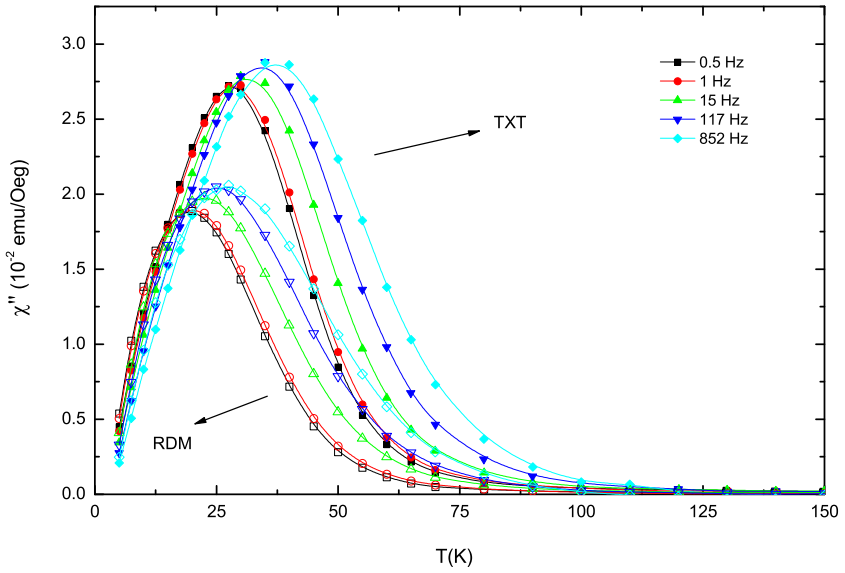

Figure 6.24: Out-of-phase susceptibility at different frequencies: solid symbols correspond to TXT sample and open symbols to RDM one.

relaxation is slower for the TXT sample. Also, we observe an increase in the out of phase susceptibility component. This indicates a larger susceptibility component along the anisotropy axis. The effect arises from the texture of the easy axes along the direction of the texturing field, that increases the fraction of particles that achieve thermal equilibrium over a determined energy barrier.

The dependence of the blocking temperature T_B with $\tau_m = 1/\omega$ is well described for both samples (RDM and TXT) by the Arrhenius law [35–37]

$$\ln(\tau_m) = \ln(\tau_0) + \frac{U_{\text{eff}}}{k_B T_B} \tag{6.18}$$

where U_{eff} corresponds to the total activation energy barrier that has contributions resulting from the magnetic anisotropy (U_0) and the dipole-dipole interactions with neighboring particles (U_{int}).

Fig. 6.25 shows that a plot of $\log_{10}\tau_m$ versus $1/T_B$ yields a straight line with an inital time much lower than τ_0, as predicted for interacting nanoparticles, even for sample RDM. In addition, this exponential prefactor is smaller for sample TXT. The slope is two times larger for sample TXT ($U_{\text{eff}} = 893$ K) than for sample RDM ($U_{\text{eff}} = 485$ K). Both effects support the interpretation that the interaction strength has increased after the magnetic texturation process.

Finally, we address the subject of the existence of a spin-glass transition. In a spin-glass, the average relaxation time must diverge at a finite temperature T_g [186],

$$\tau_c = \tau_m |1 - T/T_g|^{-z\nu} \tag{6.19}$$

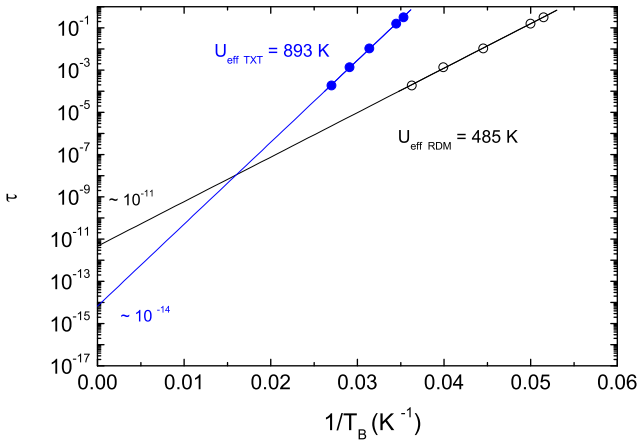

Figure 6.25: Arrhenius plot of the RDM (∘) and TXT samples (•) shows that the slope is larger for the former; the attempt time is three orders of magnitude smaller.

where $\tau_{\rm m}$ is the relaxation time of individual nanoparticles in the absence of interactions and $z\nu$ is a critical exponent. Considering that $\tau_{\rm m}$ is the relaxation time of sample RDM, in which the effect of magnetic interaction is negligible, we fit the τ of sample TXT with the expression Eq. (6.19). We show in Fig. 6.26 that the best fit where $T_{\rm g} = 23.9$ K and $z\nu = 4.8$, does not describe properly the dependence of τ with the temperature. In fact, it is not possible to find any $T_{\rm g}$ that fits the relaxation time with the expression Eq. (6.19).

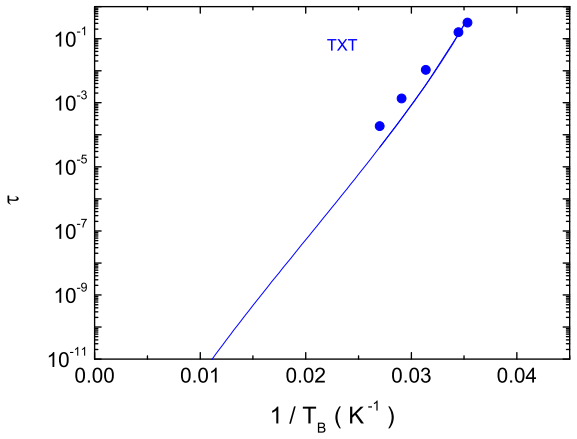

Figure 6.26: Arrhenius plot for sample TXT (•); the solid line is the fit to Eq. (6.19) where $T_{\rm g} = 23.9$ K and $z\nu = 4.8$.

6.5 Conclusions

Concerning the effect of dipolar interactions in weakly-interacting systems we can conclude, from susceptibility and SAR measurements, that magnetic relaxation becomes faster when the dipolar interaction becomes stronger. According to different theoretical models used in this work these results can be interpreted assuming that magnetic relaxation in our system is governed by single-particle anisotropy and is enhanced by dipolar interaction. Consequently, theoretical models based mainly on the contribution of dipolar interactions to the relaxation behavior are not applicable to our system.

Concerning the procedure of magnetically texturing the system in order to increase the dipolar interaction strength, we can conclude that this process induces a partial alignment of the easy axis with respect to the direction of the freezing field. This texture is reversible, which means that when the ferrofluid is heated to room temperature it recovers its initial properties. After this process, the strength of interparticle interaction increases and magnetic relaxation becomes slower. This procedure of increasing the magnitude of the interaction by magnetically texturing the ferrofluid enables the study of the effect of magnetic interactions on the relaxation times. In addition, the magnetic relaxation can not be described with the expressions developed for the spin-glass transitions.

Chapter 7

General conclusions

The particular features of nanoparticles turn into a rich magnetic behavior. Nanoparticles are rather attractive in magnetism, since they are unique systems to observe many physical phenomena. One of them, the appearance of a magnetic moment in antiferromagnetic nanoparticles, is a subject of study in this thesis. In this system, the decompensation of atomic spins produces a net magnetic moment. However, slight modifications in the particle structure may change its magnitude. In the case of akaganéite nanoparticles this change occurs just by washing the samples, because this is generating a deficient Cl^- sites occupancy. Therefore, there are two sources of magnetic moment in akaganéite nanoparticles: finite size effects and a deficient Cl^- occupancy. There is yet an additional contribution to the magnetic moment in akaganéite nanoparticles with a Cl^- occupancy that arises from the thermal population of uniform spin-precession modes. When this mode is populated, the two sublattices precesses with different amplitudes and the angle between them increases with the excitation energy. This leads to a magnetic moment with the unusual feature of increasing with temperature.

Some particular characteristics of ferrimagnetic nanoparticles also called our attention. In particular, the dependence of saturation magnetization with the nanoparticle size. Previous works showed that the saturation magnetization decreases as the size of the nanoparticles decreases. But, it is in fact hard to derive a function accounting for this decrease because when the available experimental data are plotted together, the values are widely scattered. This scattering is associated to different synthetic procedures and to different size determination methods. In order to avoid these experimental difficulties, the preparation of maghemite nanoparticles was carried out in a polymer template since the particles grow isolated and the particle size can be controlled by changing the iron to polymer ratio. A representative number of samples with a diameter size range of 1.5 to 15 nm and $\pm 10\%$ size dispersion were produced in this way. To obtain precise and representative values of the average size, this was estimated from SAXS measurements. It has been found that the dependence of the particle size with the saturation magnetization follows fairly well an analytical function based on the core-shell model. This function relates the saturation magnetization with the particle size, the saturation magnetization of the ferrimagnetic core and the thickness of a magnetically disordered shell. The fitting of the data to this function gives dead-layer thickness of 1 nm and a ferrimagnetic core with a saturation magnetization close to the bulk.

Ferrimagnetic nanoparticles can also be presented in the form of ferrofluids. This system allows a control of the magnitude of magnetic interactions between particles, so that it is a

useful model for the study of dipolar interactions. Making use of this advantage, a ferrofluid was diluted down to a concentration in which dipolar interactions are weak relative to the anisotropy energy. In this regime, some theoretical models propose that magnetic relaxation is no longer governed by interactions and it is, in fact, faster with growing interactions. These theoretical predictions are experimentally confirmed in these ferrofluids, in which the relaxation time from magnetization measurements decreases as the concentration increases. An interesting issue taking place in the medium to large dipolar interactions regime, is the experimental approach followed to modify the strength of the interactions. Here, we followed an experimental procedure that enabled us to increase the interaction strength. The process of magnetic field cooling induces a magnetic texture in the ferrofluid through the orientation of the easy axes. This texture is reversible, which means that when the ferrofluid is heated to room temperature it recovers its initial properties. After the texturing process the strength of dipolar interaction increases and magnetic relaxation becomes slower. This procedure therefore enables the quantitative study of the effect that magnetic interactions have on the relaxation times.

As it often happens in scientific studies, this thesis leaves open questions. We would like to comment on some of them and to propose possible lines of action. Concerning the influence of Cl^- occupancy on akaganéite nanocrystals magnetic behavior, the results presented here could be compared with predictions of Monte Carlo simulations. Screen-shots of the magnetic structure would be obtained that would render the ordering of the atomic spins, thus revealing the origin of the experimentally found magnetic moment. A threshold limit in the chlorine content should be found such that below this point, the structure collapses and the magnetic moment of the nanoparticle reaches a maximum. Furthermore, these simulations could be performed for different particle sizes in order to study the influence of the size in the temperature at which the thermoinduced contribution becomes noticeable. The screen shots of the magnetic structure will show the spins arrangement at different temperatures. One may expect that as the particle size increases, the difference between the ground state and excited levels would become smaller. Then, the sublattice magnetization would decreases at nearly the same temperature at which the uniform spin wave is populated. Concerning the dependence of saturation magnetization with size found here in maghemite nanocomposites it will be interesting to analyze the influence on M_S of other structural factors as the crystalline perfection, the degree of crystallization and the influence of a surface coating. With respect to the 'texturing' method for magnetic ferrofluids that is proposed here, it can be applied, not only to switch on and off the interactions, but also to 'tune' its strength. This method might allow the analysis in the whole range from weak to large dipolar interactions.

Bibliography

[1] R. J. Veitch, Soft-magnetic underlayer for MP data tape, IEEE T. Magn. 37 (2001) 1609.

[2] U. Meisen, H. Kathrein, The influence of particle size, shape and particle size distribution on properties of magnetites for the production of toners, J. Imaging Sci. Technol. 44 (2000) 508.

[3] Z. Bhimani, B. Wilson, New low cost ferrofluidic sealing challenges the mechanical seal, Ind. Lubr. Tribol. 49 (1997) 288.

[4] S. Kamiyama, K. Okamoto, T. Oyama, Study on regulating characteristics of magnetic fluid active damper, Energy Conv. Manag. 43 (3) (2002) 281.

[5] M. Takafuji, S. Ide, H. Ihara, Z. H. Xu, Preparation of poly(1-vinylimidazole)-grafted magnetic nanoparticles and their application for removal of metal ions, Chem. Mater. 16 (2004) 1977.

[6] M. S. Crainic, Z. Schlett, A flow transducer for cold water using ferrofluids, J. Magn. Magn. Mater. 268 (1-2) (2004) 8.

[7] F. X. Redl, K. S. Cho, C. B. Murray, S. O'Brien, Three-dimensional binary superlattices of magnetic nanocrystals and semiconductor quantum dots, Nature 423 (2003) 968.

[8] T. S. Chin, Permanent magnet films for applications in microelectromechanical systems, J. Magn. Magn. Mater. 209 (1-3) (2000) 75.

[9] R. Weissleder, M. Papisov, Pharmaceutical iron oxides for MR imaging, Rev. Magn. Reson. Med. 4 (1992) 1.

[10] A. Jordan, R. Scholz, K. Maier-Hauff, M. Johannsen, P. Wust, J. Nadobny, H. Schirra, H. Schmidt, S. Deger, S. Loening, W. Lanksch, R. Felix, Presentation of a new magnetic field therapy system for the treatment of human solid tumors with magnetic fluid hyperthermia, J. Magn. Magn. Mater. 225 (1-2) (2001) 118.

[11] I. Brigger, C. Dubernet, P. Couvreur, Nanoparticles in cancer therapy and diagnosis, Adv. Drug Delivery Rev. 54 (5) (2002) 631.

[12] M. A. Bogoyevitch, T. S. Kendrick, D. C. H. Ng, R. K. Barr, Taking the cell by stealth or storm? Protein Transduction Domains (PTDs) as versatile vectors for delivery, DNA Cell Biol. 21 (2002) 879.

[13] M. Uhlen, Magnetic separation of DNA, Nature 340 (1989) 733.

[14] O. Iglesias, A. Labarta, Finite-size and surface effects in maghemite nanoparticles: Monte Carlo simulations, Phys. Rev. B 63 (18).

[15] J. L. Dormann, L. Bessais, D. Fiorani, A dynamic study of small interacting particles - superparamagnetic model and spin-glass laws, J. Phys. C 21 (10) (1988) 2015.

[16] R. Gatteschi, D. Sessoli, V. J., Molecular Nanomagnets, Oxford University Press, 2006.

[17] M. N. Baibich, J. M. Broto, A. Fert, F. N. Vandau, F. Petroff, P. Eitenne, G. Creuzet, A. Friederich, J. Chazelas, Giant magnetoresistance of (001)Fe/(001) Cr magnetic superlattices, Phys. Rev. Lett. 61 (21) (1988) 2472.

[18] R. M. Cornell, U. Schwertmann, The Iron Oxides: Structure, Properties, Reactions, Occurences and Uses, Wiley, 2003.

[19] J. E. Post, V. F. Buchwald, Crystal structure refinement of akaganéite, Am. Miner. 76 (1991) 272.

[20] J. E. Post, P. J. Heaney, R. B. V. Dreele, J. C. Hanson, Neutron and temperature-resolved synchrotron X-ray powder diffraction study of akaganéite, Am. Miner. 88 (2003) 782.

[21] A. Szytula, M. Balanda, Dimitrijevic.Z, Neutron diffraction studies of β-FeOOH, Phys. Stat. Sol. (a) 3 (1) (1970) 1033.

[22] N. Yamamoto, T. Shinjo, M. Kiyama, Y. Bando, T. Takada, Mössbauer effect study of α-FeOOH and β-FeOOH - making use of oriented particles, J. Phys. Soc. Jpn. 25 (5) (1968) 1267.

[23] C. A. Barrero, K. E. García, A. L. Morales, S. Kodjikian, J. M. Greneche, New analysis of the Mössbauer spectra of akaganéite, J. Phys.: Condens. Matter 18 (2006) 6827.

[24] D. G. Chambaere, E. De Grave, On the Néel temperature of β-FeOOH: structural dependence and its implications, J. Magn. Magn. Mater. 42 (1984) 263.

[25] A. Millán, F. Palacio, E. Snoeck, V. Serin, P. Lecante, Magnetic polymer nanocomposites, in: t. t. E. Mai YW (Ed.), Polymer Nanocomposites, Cambridge: Woodhead Publishing Ltd., 2006, p. 441.

[26] C. Castro, A. Millán, F. Palacio, Nickel oxide magnetic nanocomposites in an imine polymer matrix, J. Mater. Chem. 10 (8) (2000) 1945.

[27] C. Castro, J. Ramos, A. Millán, J. González-Calbet, F. Palacio, Production of magnetic nanoparticles in imine polymer matrixes, Chem. Mater. 12 (12) (2000) 3681.

[28] J. Ramos, A. Millán, F. Palacio, Production of magnetic nanoparticles in a polyvinylpyridine matrix, Polymer 41 (24) (2000) 8461.

[29] A. Millán, F. Palacio, Magnetic nanocomposites from nitrogen base polymers, Appl. Organomet. Chem. 15 (5) (2001) 396.

[30] A. Millán, F. Palacio, A. Falqui, E. Snoeck, V. Serin, A. Bhattacharjee, V. Ksenofontov, P. Gütlich, I. Gilbert, Maghemite polymer nanocomposites with modulated magnetic properties, Acta Mater. 55 (6) (2007) 2201.

[31] A. Millán, A. Urtizberea, E. Natividad, F. Luis, N. J. O. Silva, F. Palacio, I. Mayoral, M. L. Ruiz-González, J. M. González-Calbet, P. Lecante, V. Serin, Akaganeite polymer nanocomposites, Polymer 50 (5) (2009) 1088.

[32] T. Hyeon, S. S. Lee, J. Park, Y. Chung, H. Bin Na, Synthesis of highly crystalline and monodisperse maghemite nanocrystallites without a size-selection process, J. Am. Chem. Soc. 123 (51) (2001) 12798.

[33] A. H. Morrish, The physical principles of magnetism, 1st Edition, John Wiley and Sons, New York, 1965.

[34] H. Pfeiffer, Determination of anisotropy-field distribution in particle assemblies taking into account thermal fluctuations, Phys. Stat. Sol. (a) 118 (1) (1990) 295.

[35] L. Néel, Influence des fluctuations thermiques sur l'aimantation de grains ferromagnétiques très fins, C. R. Hebd. Seances Acad. Sci. 228 (8) (1949) 664–666.

[36] W. F. Brown, Thermal fluctuations of a single-domain particle, Phys. Rev. 130 (5) (1963) 1677.

[37] W. T. Coffey, D. S. F. Crothers, Y. P. Kalmykov, E. S. Massawe, J. T. Waldron, Exact analytic formula for the correlation time of a single-domain ferromagnetic particle, Phys. Rev. E 49 (3) (1994) 1869.

[38] D. H. Martin, Magnetism in Solids, 1st Edition, Iliffe Books, London, 1967.

[39] N. J. O. Silva, V. S. Amaral, L. D. Carlos, Relevance of magnetic moment distribuiton and scaling law methods to study the magnetic behavior of antiferromagnetic nanoparticles: Application to ferritin, Phys. Rev. B 71 (18) (2005) 184408.

[40] M. Hanson, C. Johansson, S. Mørup, The influence of magnetic-anisotropy on the magnetization of small ferromagnetic particles, J. Phys. Condens. Matter 5 (6) (1993) 725.

[41] D. E. Madsen, S. Mørup, M. F. Hansen, On the interpretation of magnetization data for antiferromagnetic nanoparticles, J. Magn. Magn. Mater. 305 (1) (2006) 95–99.

[42] M. Respaud, Magnetization process of noninteracting ferromagnetic cobalt nanoparticles in the superparamagnetic regime: Deviation from langevin law, Journal of Applied Physics 86 (1) (1999) 556.

[43] J. L. García-Palacios, On the statics and dynamics of magnetoanisotropic nanoparticles, Adv. Chem. Phys. 112 (2000) 1–210.

[44] H. Kachkachi, M. Azeggagh, Magnetization of nanomagnet assemblies: Effects of anisotropy and dipolar interactions, Eur. Phys. J. B 44 (3) (2005) 299.

[45] P. Svedlindh, T. Jonsson, J. L. García-Palacios, Intra-potential-well contribution to the AC susceptibility of a noninteracting nano-sized magnetic particle system, J. Magn. Magn. Mater. 169 (3) (1997) 323.

[46] M. I. Shliomis, V. I. Stepanov, Frequency-dependence and long-time relaxation of the susceptibility of the magnetic fluids, J. Magn. Magn. Mater. 122 (1-3) (1993) 176.

[47] F. Luis, J. M. Torres, L. M. García, J. Bartolomé, J. Stankiewicz, F. Petroff, F. Fettar, J. L. Maurice, A. Vaures, Enhancement of the magnetic anisotropy of nanometer-sized Co clusters: Influence of the surface and of interparticle interactions, Phys. Rev. B 65 (9) (2002) 094409.

[48] T. Jonsson, J. Mattsson, P. Nordblad, P. Svedlindh, Energy barrier distribution of a noninteracting nano-sized magnetic particle system, J. Magn. Magn. Mater. 168 (3) (1997) 269.

[49] S. Mørup, E. Tronc, Superparamagnetic relaxation of weakly interacting particles, Phys. Rev. Lett. 72 (20) (1994) 3278.

[50] J. L. Dormann, F. D'Orazio, F. Lucari, E. Tronc, P. Prené, J. P. Jolivet, D. Fiorani, R. Cherkaoui, M. Noguès, Thermal variation of the relaxation time of the magnetic moment of γ-Fe_2O_3 nanoparticles with interparticle interactions of various strengths, Phys. Rev. B 53 (21) (1996) 14291.

[51] J. L. Dormann, D. Fiorani, E. Tronc, On the models for interparticle interactions in nanoparticle assemblies: comparison with experimental results, J. Magn. Magn. Mater. 202 (1) (1999) 251.

[52] P. E. Jönsson, J. L. García-Palacios, M. F. Hansen, P. Nordblad, Relaxation in interacting nanoparticle systems, J. Mol. Liq. 114 (1-3) (2004) 131.

[53] D. V. Berkov, N. L. Gorn, Susceptibility of the disordered system of fine magnetic particles: a Langevin-dynamics study, J. Phys.: Condens. Matter 13 (41) (2001) 9369.

[54] O. Iglesias, A. Labarta, Magnetic relaxation in terms of microscopic energy barriers in a model of dipolar interacting nanoparticles, Phys. Rev. B 70 (2004) 144401.

[55] P. Allia, M. Coisson, P. Tiberto, F. Vinai, M. Knobel, M. A. Novak, W. C. Nunes, Granular Cu-Co alloys as interacting superparamagnets, Phys. Rev. B 6414 (14) (2001) 14420.

[56] M. El-Hilo, K. O'Grady, R. W. Chantrell, The ordering temperature in fine particle-systems, J. Magn. Magn. Mater. 117 (1-2) (1992) 21.

[57] L. Néel, Superantiferromagnétisme dans les grains fins, C. R. Hebd. Seances Acad. Sci. 253 (2) (1961) 203–208.

[58] L. Néel, Superposition de l'antiferromagnétisme et du superparamagnétisme dans un grain très fin, C. R. Hebd. Seances Acad. Sci. 253 (1) (1961) 9–12.

[59] L. Néel, Superparamagnétisme des grains très fins antiferromagnétiques, C. R. Hebd. Seances Acad. Sci. 252 (26) (1961) 4075–4080.

[60] L. Néel, Sur le calcul de la susceptibilité additionnelle superantiferromagnétique des grains fins et sa variation thermique, C. R. Hebd. Seances Acad. Sci. 253 (13) (1961) 1286–1291.

[61] S. Mørup, C. Frandsen, Thermoinduced magnetization in nanoparticles of antiferromagnetic materials, Phys. Rev. Lett. 92 (2004) 217201.

[62] S. Mørup, B. R. Hansen, Uniform magnetic excitations in nanoparticles, Phys. Rev. B 72 (2005) 024418.

[63] F. Keffer, C. Kittel, Theory of antiferromagnetic resonance, Phys. Rev. 85 (1952) 329.

[64] D. E. Madsen, S. Mørup, Thermoinduced magnetization and uncompensated spins in antiferromagnetic nanoparticles, Phys. Rev. B 74 (2006) 014405.

[65] B. D. Cullity, S. R. Stock, Elements of X-Ray diffraction, Pearson education, Prentice Hall, Upper Saddle River New Jersey, 2001.

[66] http://www.malvern.com/LabEng/products/zetasizer/zetasizer.htm.

[67] A. Guinier, G. Fournet, Small Angle Scattering of X-Rays, John Wiley and Sons, 1955.

[68] A. Feigin, D. I. Svergun, Structure Analysis by Small-Angle X-Ray and Neutron Scattering, Plenum, 1987.

[69] Small - Angle X - ray Scattering, O. Glatter and O. Kratky Edition, New York: Academic Press., 1982.

[70] A. V. Semenyuk, D. I. Svergun, GNOM - a program package for small-angle scattering data-processing, J. Appl. Crystallogr. 24 (1991) 537.

[71] D. Svergun, A. Semenyuk, Biological small angle scattering group (BioSAXS), http://www.embl-hamburg.de/biosaxs/gnom.html.

[72] G. Beaucage, Approximations leading to a unified exponential power-law approach to small-angle scattering, J. Appl. Crystallogr. 28 (1995) 717.

[73] G. Beaucage, Small-angle scattering from polymeric mass fractals of arbitrary mass-fractal dimension, J. Appl. Crystallogr. 29 (1996) 134.

[74] G. Beaucage, H. K. Kammler, S. E. Pratsinis, Particle size distributions from small-angle scattering using global scattering functions, J. Appl. Crystallogr. 37 (2004) 523.

[75] P. V. Konarev, V. V. Volkov, A. V. Sokolova, M. H. J. Koch, D. I. Svergun, PRIMUS: a Windows PC-based system for small-angle scattering data analysis, J. Appl. Crystallogr. 36 (2003) 1277.

[76] D. Orthaber, A. Bergmann, O. Glatter, SAXS experiments on absolute scale with Kratky systems using water as a secondary standard, J. Appl. Crystallogr. 33 (2000) 218.

[77] E. Natividad, M. Castro, A. Mediano, Accurate measurement of the specific absorption rate using a suitable adiabatic magnetothermal setup, Appl. Phys. Lett. 92 (9) (2008) 093116.

[78] E. Natividad, M. Castro, A. Mediano, Adiabatic vs. non-adiabatic determination of specific absorption rate of ferrofluids, J. Magn. Magn. Mater. 321 (10) (2009) 1497.

[79] R. E. Rosensweig, Heating magnetic fluid with alternating magnetic field, J. Magn. Magn. Mater. 252 (2002) 370.

[80] M. Mc Elfresh, Fundamentals of Magnetism and Magnetic Measurements, Purdue University, Quantum Design Inc., 1994, (http://www.qdusa.com/resources/pdf/FundPrimer.pdf).

[81] A. D. Hibbs, R. E. Sager, S. Kumar, J. E. McArthur, A. L. Singsaas, K. G. Jensen, M. A. Steindorf, T. A. Aukerman, H. M. Schneider, A squid-based ac susceptometer, Rev. Sci. Instrum. 65 (8) (1994) 2644.

[82] http://www.qdusa.com/products/brochures/vsmappnote3-07.pdf.

[83] http://www.ru.nl/hfml/facility/experimental/magnets/#c5.

[84] E. M. Coe, L. H. Bowen, J. A. Speer, Z. H. Wang, D. E. Sayers, R. D. Bereman, The recharacterization of a polysaccharide iron complex (Niferex), J. Inorg. Biochem. 58 (4) (1995) 269.

[85] F. Cadena, M. Johnson, US Patent 2004262225.

[86] N. S. Clarke, P. G. Hall, Adsorption of water-vapor by iron-oxides .1. preparation and characterization of the adsorbents, Langmuir 7 (4) (1991) 672.

[87] Z. Y. Yuan, T. Z. Ren, B. L. Su, Surfactant mediated nanoparticle assembly of catalytic mesoporous crystalline iron oxide materials, Catal. Today 93-5 (2004) 743.

[88] N. G. Holm, M. J. Dowler, T. Wadsten, G. Arrhenius, β-FeOOH·Cl_n (akaganeite) and $Fe_{1-x}O$ (wustite) in hot brine from the atlantis-II deep (red-sea) and the uptake of amino-acids by synthetic β-FeOOH·Cl_n, Geochim. Cosmochim. Acta 47 (8) (1983) 1465.

[89] P. Keller, Eigenschaften von $(Cl,F,OH)_{<2}Fe_8(O,OH)_{16}$ und akaganéit, Neues Jahrb. Miner. Abh. 113 (1970) 29.

[90] R. V. Morris, D. C. Golden, J. F. Bell, T. D. Shelfer, A. C. Scheinost, N. W. Hinman, G. Furniss, S. A. Mertzman, J. L. Bishop, D. W. Ming, C. C. Allen, D. T. Britt, Mineralogy, composition, and alteration of mars pathfinder rocks and soils: Evidence from multispectral, elemental, and magnetic data on terrestrial analogue, snc meteorite, and pathfinder samples, J. Geophys. Res. Planets 105 (E1) (2000) 1757.

[91] V. F. Buchwald, R. S. Clarke, Corrosion of Fe-Ni alloys by Cl-containing akaganeite (β-FeOOH) - the antarctic meteorite case, Am. Mineral. 74 (5-6) (1989) 656.

[92] S. Goñi-Elizalde, M. E. García-Clavel, M. I. Tejedor-Tejedor, Mechanism of akaganeite-hematite transformation via solution, React. Solid. 3 (1-2) (1987) 139.

[93] R. M. Cornell, R. Giovanoli, Transformation of akaganeite into goethite and hematite in alkaline media, Clays Clay Miner. 38 (5) (1990) 469.

[94] M. A. Blesa, M. Mijalchik, M. Villegas, G. Rigotti, Transformation of akaganeite into magnetite in aqueous hydrazine suspensions, React. Solids 2 (1-2) (1986) 85.

[95] H. B. Weiser, W. O. Milligan, X-ray studies on the hydrous oxides. V. Beta ferric oxide monohydrate, J. Am. Chem. Soc. 57 (1) (1935) 238.

[96] K. Stahl, K. Nielsen, J. Z. Jiang, B. Lebech, J. C. Hanson, P. Norby, J. van Lanschot, On the akaganeite crystal structure, phase transformations and possible role in post-excavational corrosion of iron artifacts, Corros. Sci. 45 (11) (2003) 2563.

[97] H. M. Bao, P. L. Koch, Oxygen isotope fractionation in ferric oxide-water systems: Low temperature synthesis, Geochim. Cosmochim. Ac. 63 (5) (1999) 599.

[98] R. J. Atkinson, A. M. Posner, J. P. Quirk, Crystal nucleation and growth in hydrolyzing iron(III) chloride solutions, Clay. Clay Miner. 25 (1) (1977) 49.

[99] P. A. Riveros, J. E. Dutrizac, The precipitation of hematite from ferric chloride media, Hydrometallurgy 46 (1-2) (1997) 85.

[100] P. Refait, J. M. R. Genin, The mechanisms of oxidation of ferrous hydroxychloride β-$Fe_2(OH)_3Cl$ in aqueous solution: The formation of akaganeite vs goethite, Corros. Sci. 39 (3) (1997) 539.

[101] J. K. Bailey, C. J. Brinker, M. L. Mecartney, Growth mechanisms of iron-oxide particles of differing morphologies from the forced hydrolysis of ferric-chloride solutions, J. Colloid Interface Sci. 157 (1) (1993) 1.

[102] H. Fan, B. Song, Z. Yang, Q. Li, Fast inducing synthesis of spherical superparamagnetic β-FeOOH nanoparticles without aggregation, Chem. Lett. 33 (5) (2004) 576.

[103] Z. Y. Yuan, B. L. Su, Surfactant-assisted nanoparticle assembly of mesoporous β-FeOOH (akaganeite), Chem. Phys. Lett. 381 (5-6) (2003) 710.

[104] A. Saric, K. Nomura, S. Popovic, N. Ljubesic, S. Music, Effects of urotropin on the chemical and microstructural properties of Fe-oxide powders prepared by the hydrolysis of aqueous $FeCl_3$ solutions, Mater. Chem. Phys. 52 (3) (1998) 214.

[105] D. N. Bakoyannakis, E. A. Deliyanni, A. I. Zouboulis, K. A. Matis, L. Nalbandian, T. Kehagias, Akaganeite and goethite-type nanocrystals: synthesis and characterization, Microporous and Mesoporous Mater. 59 (1) (2003) 35.

[106] M. Nesterova, J. Moreau, J. F. Banfield, Model biomimetic studies of templated growth and assembly of nanocrystalline FeOOH, Geochim. Cosmochim. Acta 67 (6) (2003) 1177.

[107] Z. Y. Sun, J. B. Huang, Effect of dextran on the crystallization of ferric hydroxide, Acta Phys. Chim. Sin. 22 (2) (2006) 172.

[108] F. Funk, G. J. Long, D. Hautot, R. Buchi, I. Christl, P. G. Weidler, Physical and chemical characterization of therapeutic iron containing materials: A study of several superparamagnetic drug formulations with the β-FeOOH or ferrihydrite structure, Hyperfine Interact. 136 (1-2) (2001) 73.

[109] B. Knight, L. H. Bowen, R. D. Bereman, S. Y. Huang, E. De Grave, Comparison of the core size distribution in iron dextran complexes using Mössbauer spectroscopy and X-ray diffraction, J. Inorg. Biochem. 73 (4) (1999) 227.

[110] F. J. Lázaro, A. Larrea, A. R. Abadía, Magnetostructural study of iron-dextran, J. Magn. Magn. Mater. 257 (2-3) (2003) 346.

[111] S. Dante, Z. Z. Hou, S. Risbud, P. Stroeve, Nucleation of iron oxy-hydroxide nanoparticles by layer-by-layer polyionic assemblies, Langmuir 15 (6) (1999) 2176.

[112] L. Y. Zhang, D. S. Xue, J. Fen, Magnetic properties of amorphous β-FeOOH nanowire arrays, J. Magn. Magn. Mater. 305 (1) (2006) 228.

[113] J. Y. Bottero, A. Manceau, F. Villieras, D. Tchoubar, Structure and mechanisms of formation of FeOOH(Cl) polymers, Langmuir 10 (1) (1994) 316.

[114] J. Rose, A. Manceau, J. Y. Bottero, A. Masion, F. García, Nucleation and growth mechanisms of Fe oxyhydroxide in the presence of PO_4 ions .1. Fe K-edge EXAFS study, Langmuir 12 (26) (1996) 6701.

[115] E. Wolska, Relations between the existence of hydroxyl ions in the anionic sublattice of hematite and its infrared and X-ray-characteristics, Solid State Ionics 28 (1988) 1349.

[116] E. Murad, J. L. Bishop, The infrared spectrum of synthetic akaganeite, β-FeOOH, Am. Miner. 85 (5-6) (2000) 716.

[117] J. M. González-Calbet, M. A. Alario-Franco, M. Gayoso-Andrade, The porous structure of synthetic akaganeite, J. Inorg. Nucl. Chem. 43 (2) (1981) 257.

[118] B. Weckler, H. D. Lutz, Lattice vibration spectra. part XCV. infrared spectroscopic studies on the iron oxide hydroxides goethite (α), akaganeite (β), lepidocrocite (γ), and feroxyhite (δ), Solid State Inorg. Chem. 35 (8-9) (1998) 531.

[119] A. Saric, S. Music, K. Nomura, S. Popovic, Microstructural properties of Fe-oxide powders obtained by precipitation from $FeCl_3$ solutions, Mater. Sci. Eng. B 56 (1) (1998) 43.

[120] E. A. Deliyanni, D. N. Bakoyannakis, A. I. Zouboulis, K. A. Matis, L. Nalbandian, Akaganeite-type β-FeO(OH) nanocrystals: preparation and characterization, Microporous Mesoporous Mat. 42 (1) (2001) 49.

[121] A. Millán, A. Urtizberea, N. J. O. Silva, P. Boesecke, E. Natividad, F. Palacio, E. Snoeck, L. Soriano, A. Gutierrez, C. Quiros, Multiple-length-scale small-angle X-ray scattering analysis on maghemite nanocomposites, J. Appl. Crystallogr. 40 (2007) S696.

[122] G. Porod, Kolloid Z. 124 (1951) 83.

[123] D. G. Chambaere, E. De Grave, The β-FeOOH to α-Fe_2O_3 phase-transformation - structural and magnetic phenomena, Phys. Chem. Miner. 12 (3) (1985) 176.

[124] J. van Lierop, D. H. Ryan, M. E. Pumarol, M. Roseman, Muon spin relaxation study of spin dynamics in a polysaccharide iron complex, J. Appl. Phys. 89 (11) (2001) 7645.

[125] L. Néel, Propriétés magnétiques des grains fins antiferromagnétiques - superparamagnétisme et superantiferromagnétisme, J. Phys. Soc. Jpn. 17, Supplement B-I (1962) 676.

[126] S. Kilcoyne, R. Cywinski, Ferritin: a model superparamagnet, J. Magn. Magn. Mater. 140 (1995) 1466.

[127] S. A. Makhlouf, F. T. Parker, A. E. Berkowitz, Magnetic hysteresis anomalies in ferritin, Phys. Rev. B 55 (1997) R14717.

[128] J. G. E. Harris, J. E. Grimaldi, D. D. Awschalom, A. Chiolero, D. Loss, Excess spin and the dynamics of antiferromagnetic ferritin, Phys. Rev. B 60 (5) (1999) 3453.

[129] M. S. Seehra, V. S. Babu, A. Manivannan, J. W. Lynn, Neutron scattering and magnetic studies of ferrihydrite nanoparticles, Phys. Rev. B 61 (2000) 3513.

[130] D. G. Chambaere, E. De Grave, A study of the non-stoichiometrical Halogen and Water-content of β-FeOOH, Phys. status solidi. A, Appl. and Mater. Sci. 83 (1) (1984) 93.

[131] D. S. Kulgawczuk, Z. Obuszko, A. Szytula, Susceptibility and magnetization of β- and δ-FeOOH, Phys. Stat. Sol. 26 (1) (1968) K83.

[132] A. Abragam, B. Bleaney, Electron Paramagnetic Resonance of Transition Ions, Dover publications, 1970.

[133] B. E. Lang, Specific heat and thermodynamic properties of metallic systems: Instrumentation and analysis, Ph.D. thesis, Department of Chemistry and Biochemistry, Brigham Young University, (2005) (http://contentdm.lib.byu.edu/ETD/image/etd1031.pdf).

[134] H. Rohrer, H. Thomas, Phase transitions in uniaxial antiferromagnet, J. Applied Phys. 40 (3) (1969) 1025.

[135] J. M. D. Coey, A. Barry, J. M. Brotto, H. Rakoto, S. Brennan, W. N. Mussel, A. Collomb, D. Fruchart, Spin-flop in goethite, J. Phys.: Condens. Matter 7 (4) (1995) 759–768.

[136] J. Takagi, S. Takakura, T. Okada, T. Kobayashi, M. Ozaki, H. Kihira, T. Mizoguchi, Estimation of magneto-crystalline uniaxial anisotropy constant of β-FeOOH by Mössbauer spectroscopy, Corros. Sci. 50 (7) (2008) 1971.

[137] C. Zener, Classical theory of the temperature dependence of magnetic anisotropy energy, Phys. Rev. 96 (5) (1954) 1335.

[138] F. Keffer, Temperature dependence of ferromagnetic anisotropy in cubic crystals, Phys. Rev. 100 (6) (1955) 1692.

[139] F. Keffer, T. Oguchi, Ferromagnetic anisotropy in cubic crystals, Phys. Rev. 117 (3) (1960) 718.

[140] A. Aharoni, Introduction to the theory of Ferromagnetism, Oxford Science publications, 2000.

[141] N. J. O. Silva, V. S. Amaral, L. D. Carlos, B. Rodríguez-González, L. M. Liz-Marzán, T. S. Berquó, S. K. Banerjee, V. de Zea Bermúdez, A. Millán, F. Palacio, Evidence of random magnetic anisotropy in ferrihydrite nanoparticles based on analysis of statistical distributions, Phys. Rev. B 77 (13) (2008) 134426.

[142] C. R. H. Bahl, J. Garde, K. Lefmann, T. B. S. Jensen, P. A. Lindgard, D. E. Madsen, S. Mørup, Uniform spin wave modes in antiferromagnetic nanoparticles with uncompensated moments, Eur. Phys. J. B 62 (1) (2008) 53.

[143] Q. A. Pankhurst, R. J. Pollard, Origin of the spin-canting anomaly in small ferrimagnetic particles, Phys. Rev. Lett. 67 (2) (1991) 248.

[144] M. P. Morales, C. J. Serna, F. Bodker, S. Mørup, Spin canting due to structural disorder in maghemite, J. Phys.: Condens. Matter 9 (25) (1997) 5461.

[145] C. J. Serna, F. Bodker, S. Mørup, M. P. Morales, F. Sandiumenge, S. Veintemillas-Verdaguer, Spin frustration in maghemite nanoparticles, Solid State Commun. 118 (9) (2001) 437.

[146] F. T. Parker, M. W. Foster, D. T. Margulies, A. E. Berkowitz, Spin canting, surface magnetization, and finite-size effects in γ-Fe_2O_3 particles, Phys. Rev. B 47 (13) (1993) 7885.

[147] P. V. Hendriksen, F. Bodker, S. Linderoth, S. Wells, S. Mørup, Ultrafine maghemite particles .1. Studies of induced magnetic texture, J. Phys.: Condens. Matter 6 (16) (1994) 3081.

[148] P. V. Hendriksen, S. Linderoth, C. A. Oxborrow, S. Mørup, Ultrafine maghemite particles .2. The spin-canting effect revisited, J. Phys.: Condens. Matter 6 (16) (1994) 3091.

[149] A. Berkowitz, J. A. Lahut, I. S. Jacobs, L. M. Levinson, D. W. Forester, Spin pinning at ferrite-organic interfaces, Phys. Rev. Lett. 34 (10) (1975) 594.

[150] A. H. Morrish, K. Haneda, Magnetic-structure of small $NiFe_2O_4$ particles, J. Appl. Phys. 52 (3) (1981) 2496.

[151] F. Gazeau, E. Dubois, M. Hennion, R. Perzynski, Y. Raikher, Quasi-elastic neutron scattering on γ-Fe_2O_3 nanoparticles, Europhys. Lett. 40 (5) (1997) 575.

[152] D. Lin, A. C. Nunes, C. F. Majkrzak, A. E. Berkowitz, Polarized neutron study of the magnetization density distribution within a $CoFe_2O_4$ colloidal particle, J. Magn. Magn. Mater. 145 (3) (1995) 343.

[153] T. Okada, H. Sekizawa, F. Ambe, S. Ambe, T. Yamadaya, Magnetic and Mössbauer studies of Co adsorbed γ-Fe_2O_3, J. Magn. Magn. Mater. 31-4 (1983) 903.

[154] R. H. Kodama, A. E. Berkowitz, Atomic-scale magnetic modeling of oxide nanoparticles, Phys. Rev. B 59 (9) (1999) 6321.

[155] H. Kachkachi, M. Dimian, Hysteretic properties of a magnetic particle with strong surface anisotropy, Phys. Rev. B 66 (17) (2002) 174419.

[156] A. Berkowitz, W. J. Schuele, P. J. Flanders, Influence of crystallite size on magnetic properties of acicular γ-Fe_2O_3 particles, J. Appl. Phys. 39 (1968) 1261.

[157] R. H. Kodama, A. E. Berkowitz, E. J. McNiff, S. Foner, Surface spin disorder in $NiFe_2O_4$ nanoparticles, Phys. Rev. Lett. 77 (2) (1996) 394.

[158] B. Martínez, X. Obradors, L. Balcells, A. Rouanet, C. Monty, Low temperature surface spin-glass transition in γ-Fe_2O_3 nanoparticles, Phys. Rev. Lett. 80 (1) (1998) 181.

[159] J. M. D. Coey, Noncollinear spin arrangement in ultrafine ferrimagnetic crystallites, Phys. Rev. Lett. 27 (17) (1971) 1140.

[160] E. Tronc, P. Prene, J. P. Jolivet, J. L. Dormann, J. M. Greneche, Spin canting in γ-Fe_2O_3 nanoparticles, Hyperfine Interact. 112 (1-4) (1998) 97.

[161] S. Mørup, Spin-canting and transverse relaxation at surfaces and in the interior of ferrimagnetic particles, J. Magn. Magn. Mater. 266 (1-2) (2003) 110.

[162] S. Linderoth, P. V. Hendriksen, F. Bodker, S. Wells, K. Davies, S. W. Charles, S. Mørup, On spin-canting in maghemite particles, J. Appl. Phys. 75 (10) (1994) 6583.

[163] M. P. Morales, M. Andres-Verges, S. Veintemillas-Verdaguer, M. I. Montero, C. J. Serna, Structural effects on the magnetic properties of γ-Fe_2O_3 nanoparticles, J. Magn. Magn. Mater. 203 (1999) 146.

[164] M. P. Morales, S. Veintemillas-Verdaguer, M. I. Montero, C. J. Serna, A. Roig, L. Casas, B. Martínez, F. Sandiumenge, Surface and internal spin canting in γ-Fe_2O_3 nanoparticles, Chem. Mater. 11 (11) (1999) 3058.

[165] N. Feltin, M. P. Pileni, New technique for synthesizing iron ferrite magnetic nanosized particles, Langmuir 13 (15) (1997) 3927.

[166] E. M. Moreno, M. Zayat, M. P. Morales, C. J. Serna, A. Roig, D. Levy, Preparation of narrow size distribution superparamagnetic γ-Fe_2O_3 nanoparticles in a sol-gel transparent SiO_2 matrix, Langmuir 18 (12) (2002) 4972.

[167] C. Brosseau, J. Ben Youssef, P. Talbot, A. M. Konn, Electromagnetic and magnetic properties of multicomponent metal oxides heterostructures: Nanometer versus micrometer-sized particles, J. Appl. Phys. 93 (11) (2003) 9243.

[168] X. N. Xu, Y. Wolfus, A. Shaulov, Y. Yeshurun, I. Felner, I. Nowik, Y. Koltypin, A. Gedanken, Annealing study of Fe_2O_3 nanoparticles: Magnetic size effects and phase transformations, J. Appl. Phys. 91 (7) (2002) 4611.

[169] E. Tronc, M. Nogues, C. Chaneac, F. Lucari, F. D'Orazio, J. M. Greneche, J. P. Jolivet, D. Fiorani, A. M. Testa, Magnetic properties of γ-Fe_2O_3 dispersed particles: size and matrix effects, J. Magn. Magn. Mater. 272 (2004) 1474.

[170] S. Koutani, G. Gavoille, R. Gerardin, Magnetic-behavior of aggregates of small γ-Fe_2O_3 particles, J. Magn. Magn. Mater. 123 (1-2) (1993) 175.

[171] C. Pecharroman, T. González-Carreño, J. E. Iglesias, The infrared dielectric-properties of maghemite, γ-Fe_2O_3, from reflectance measurement on pressed powders, Phys. Chem. Miner. 22 (1) (1995) 21.

[172] O. Spalla, S. Lyonnard, F. Testard, Analysis of the small-angle intensity scattered by a porous and granular medium, J. Appl. Crystallogr. 36 (2003) 338.

[173] P. Riello, A. Benedetti, Small angle scattering of a polydisperse system of interacting hard spheres: An analytical solution, J. Chem. Phys. 106 (1997) 8660.

[174] P. R. Laity, J. E. Taylor, S. S. Wong, P. Khunkamchoo, K. Norris, M. Cable, G. T. Andrews, A. F. Johnson, R. E. Cameron, A review of small-angle scattering models for random segmented poly(ether-urethane) copolymers, Polymer 45 (2004) 7273.

[175] B. Martínez, A. Roig, X. Obradors, E. Molins, A. Rouanet, C. Monty, Magnetic properties of γ-Fe_2O_3 nanoparticles obtained by vaporization condensation in a solar furnace, J. Appl. Phys. 79 (5) (1996) 2580.

[176] P. Weiss, R. Forrer, Absolute saturation of ferromagnetic substances and the law of approach as a function of the field and of the temperature, Ann. Phys. 10 (12) (1929) 279.

[177] K. Woo, J. Hong, S. Choi, H. W. Lee, J. P. Ahn, C. S. Kim, S. W. Lee, Easy synthesis and magnetic properties of iron oxide nanoparticles, Chem. Mater. 16 (14) (2004) 2814.

[178] D. Makovec, A. Kosak, A. Znidarsic, M. Drofenik, The synthesis of spinel-ferrite nanoparticles using precipitation in microemulsions for ferrofluid applications, J. Magn. Magn. Mater. 289 (2005) 32.

[179] E. Tronc, A. Ezzir, R. Cherkaoui, C. Chaneac, M. Nogues, H. Kachkachi, D. Fiorani, A. M. Testa, J. M. Greneche, J. P. Jolivet, Surface-related properties of γ-Fe_2O_3 nanoparticles, J. Magn. Magn. Mater. 221 (1-2) (2000) 63.

[180] G. Fonnum, C. Johansson, A. Molteberg, S. Mørup, E. Aksnes, Characterisation of Dynabeads® by magnetization measurements and Mössbauer spectroscopy, J. Magn. Magn. Mater. 293 (1) (2005) 41.

[181] P. Dutta, A. Manivannan, M. S. Seehra, N. Shah, G. P. Huffman, Magnetic properties of nearly defect-free maghemite nanocrystals, Phys. Rev. B 70 (17).

[182] J. Park, E. Lee, N. M. Hwang, M. S. Kang, S. C. Kim, Y. Hwang, J. G. Park, H. J. Noh, J. Y. Kini, J. H. Park, T. Hyeon, One-nanometer-scale size-controlled synthesis of monodisperse magnetic iron oxide nanoparticles, Angew. Chem.-Int. Edit. 44 (19) (2005) 2872.

[183] Y. Komorida, M. Mito, H. Deguchi, S. Takagi, A. Millán, N. J. O. Silva, F. Palacio, Surface and core magnetic anisotropy in maghemite nanoparticles determined by pressure experiments, Appl. Phys. Lett. 94 (20).

[184] O. Iglesias, A. Labarta, From finite-size and surface effects to glassy behaviour in ferrimagnetic particles, in: D. Fiorani (Ed.), Surface effects in magnetic nanoparticles, Nanostructure Science and Technology, Springer, 2005, p. 105.

[185] M. F. Hansen, S. Mørup, Models for the dynamics of interacting magnetic nanoparticles, J. Magn. Magn. Mater. 184 (3) (1998) 262.

[186] P. E. Jönsson, Superparamagnetism and spin-glass dynamics of interacting magnetic nanoparticle systems, Adv. Chem. Phys. 128 (2004) 191.

[187] J. Wagner, B. Fischer, T. Autenrieth, Field induced anisotropy of charged magnetic colloids: A rescaled mean spherical approximation study, J. Chem. Phys. 124 (11) (2006) 114901.

[188] G. Meriguet, F. Cousin, E. Dubois, F. Boue, A. Cebers, B. Farago, W. Perzynski, What tunes the structural anisotropy of magnetic fluids under a magnetic field?, J. Phys. Chem. B 110 (9) (2006) 4378.

[189] P. V. Hendriksen, S. Linderoth, P. A. Lindgard, Finite-size modifications of the magnetic-properties of clusters, Phys. Rev. B 48 (10) (1993) 7259.

[190] K. O'Grady, A. Bradbury, J. Popplewell, S. W. Charles, R. W. Chantrell, The effect of field-induced texture on the properties of a fine particle system, J. Magn. Magn. Mater. 49 (1-2) (1985) 106.

[191] Y. L. Raikher, The magnetization curve of a textured ferrofluid, J. Magn. Magn. Mater. 39 (1-2) (1983) 11.

[192] F. Bentivegna, J. Ferre, M. Nyvlt, J. P. Jamet, D. Imhoff, M. Canva, A. Brun, P. Veillet, S. Visnovsky, F. Chaput, J. P. Boilot, Magnetically textured γ-Fe_2O_3 nanoparticles in a silica gel matrix: Structural and magnetic properties, J. Applied. Phys. 83 (12) (1998) 7776.

[193] R. W. Chantrell, N. Y. Ayoub, J. Popplewell, The low field susceptibility of a textured superparamagnetic system, J. Magn. Magn. Mater. 53 (1-2) (1985) 199.

List of Figures

List of Articles

Much of the work developed in this thesis has been submitted to publication. Here, we list the articles that has been published,

- **Specific Absorption Rates and Magnetic Properties of Ferrofluids with Interaction Effects at Low Concentrations**; A. Urtizberea; E. Natividad; A. Arizaga; M. Castro; A. Mediano; **J. Phys. Chem. C 114** (11), p 4916 (2010)
- **Akaganeite polymer nanocomposites**; A. Millan, A. Urtizberea, E. Natividad, F. Luis, N. J. O. Silva, F. Palacio, I. Mayoral, M. L. Ruiz-González, J. M. González-Calbet, P. Lecante, V. Serin; **Polymer 50** (5), p 1088 (2009)
- **Surface effects in maghemite nanoparticles**; A. Millan, A. Urtizberea, N. J. O. Silva, F. Palacio, V. S. Amaral, E. Snoeck, V. Serin; **J. Magn. Magn. Mater. 312** (1), L5 (2007)
- **Multiple-length-scale small-angle X-ray scattering analysis on maghemite nanocomposites**; A. Millan, A. Urtizberea, N. J. O. Silva, P. Boesecke, E. Natividad, F. Palacio, E. Snoeck, L. Soriano, A. Gutierrez, C. Quiros; **J. Appl. Crystallogr. 40** (1), p S696 (2007)